Seventh DELTA
User- meeting

Dortmund
30. November 2011

Dear reader, dear colleague,

again a year of successful work at DELTA can be registered. To prove this statement you only need to have a look into the presented User-Reports for 2011. A respectable number of high quality reports are presented. These papers as well as the number of students educated at DELTA in the recent past let me be an optimist: DELTA has a future!

Additionally, several changes and of course improvements of DELTA were carried out. If you would like to read some details about it please consult the extended abstract presented by M. Bakr et al. in this Annual Report.

DELTA is a small Synchrotron Facility supported by a small number of professionals covering very different fields of work. They have at least one common characteristic: They are idealists. And this makes the work at DELTA attractive and pleasant, too. Thanks to the staff, to the government, to the responsible, and to all contributors.

Alex von Bohlen
November 2011


7th DELTA User-Meeting
Dortmund, 30 November 2011

Generation of ultrashort VUV and THz pulses at the DELTA storage ring using coherent harmonic generation (CHG)

M. Bakr, M. Höner, H. Huck, S. Khan, R. Molo, A. Nowaczyk, A. Schick, P. Ungelenk, M. Zeinalzadeh

Beamline BL-1: Deep X-Ray Lithography

T. Brenner, D. Lietz, M. Paulus, U. Berges, C. Sternemann, M. Tolan

Spin- and angle-resolved PES on Bi_2Te_3 / Si(111) thin films at BL5

A. Herdt, L. Plucinski, S. Döring, G. Bihlmayer, C.M. Schneider

XAFS at the liquid air interface

S. Bieder, D.C. F. Wieland, J. Möller, R. Wagner, M. Paulus, C. Sternemann, P. Degen, M. Tolan

Hydration properties of micelles

M. A. Schroer, C. J. Sahle, J. Smiatek, P. Degen, C. Sternemann, M. Tolan

In depth profiling by GIXRF of ion-implanted Si-wafers

A. von Bohlen, M. Brücher, R. Hergenröder

Local atomic and electronic structure of Ag clusters deposited in a polydimethylsiloxane (PDMS) matrix

S. Homann, S. Due, K.Latussek, D. Engemann, S. Balk, R. Wagner, C.Sternemann, M. Paulus, C. J. Sahle, M. A. Schroer, H. Hövel

Size controlled and Ge-oxide free Ge NC formation in multilayered GeSiO/SiO2

C. J. Sahle, M. Zschintzsch, C. Sternemann, A. Nyrow, A. Schwamberger, M. Tolan

Influence of the chemical reaction path on the crystalline structure of sol-gel derived TiO_2 and TiO_2-ZrO_2 nanoparticles

S. J. Pfleiderer, D. Lützenkirchen-Hecht, R. Frahm

Characterization of the microstructure in diffusion brazed Al-Al- and Al-steel- joints

L. Wojarski, A. Steffen, C. Sternemann, M. Paulus, S. Alkas-Yonan, M. Tolan, W. Tillmann

X-ray diffraction studies on low alloyed and high-Mn steels with TRansformation and TWinning Induced Plasticity (TRIP, TWIP)

H. Quade, R. Twardowski, S. Buttmann, A. Steffen, M. Paulus, C. Sternemann, M. Tolan, U. Prahl, W. Bleck

Optimization of the mechanical properties of HVOF sprayed nanostructured WC-Co coatings manufactured by fine powders (-10+2 µm) with ultra-fine carbides (400 nm)

W. Tillmann, M. Tolan, P. Hollingsworth, I. Baumann, M. Paulus

The effect of high pressure on peanuts

M. A. Schroer, M. Paulus, M. Tolan

Investigation the effect of iron incorporation during Kr^+ ion beam sputtering on Si (001) by using X-ray absorption near edge spectroscopy (XANES)

B. Khanbabaee, B. Arezki, A. Biermanns1, M. Cornejo, D. Hirsch, F. Frost, U. Pietsch, D. Lützenkirchen-Hecht, R. Wagner

Electronic structure study of the ferrospinel $NiFe_2O_4$

M. Müller, C. Caspers, S. Kramer-Sinzinger, S. Döring, U. Berges, C. M. Schneider, C. Westphal

The X-ray investigation of doping influence on InAs wire by selective area MOVPE growth

A. Davydok, A. Biermanns, K.Sladek , S.Abbasi, U. Pietsch

Current Induced Structural Changes of Thin Film OFET Devices

L. Grodd, A. Davydok, S. Grigorian, U. Pietsch

Influence of Alkyl Side Chains on the Formation of RT and -30°C Cast P3AT crystallites

T. S. Shabi, S. Grigorian, M. Brinkmann, U. Pietsch, N. Kayunkid, N. Koenen, U. Scherf

XANES and EXAFS studies on diamond metal composites

A. Steffen, M. Paulus, M. Ferreira, W. Tillmann, M. Tolan

Temperature induced phase separation and nanocrystal formation in bulk amorphous $Si_xGe_yO_z$ with high Ge amount

A. Nyrow, C. J. Sahle, C. Sternemann, A. Schwamberger, R. Wagner, A. Hohl, M. Tolan

Investigation of TRIP assisted Q&P steels

N. Große-Heilmann, C. Kronholz, A. Peters, A. Steffen, K. Rüster, M. Tolan

Temperature-induced denaturation of protein layers at solid-liquid interfaces - an x-ray reflectivity study

I. Kiesel, M. Paulus, J. Nase, S. Tiemeyer, C. Sternemann, M. Tolan

Determination of melting temperatures of strained natural rubber vulcanizates

B. Heuwers, R. Hoeher, D. Quitmann, F. Katzenberg, J. C.Tiller

The new setup for grazing incidence diraction measurements at BL9

F. J. Wirkert, M. Paulus, C. Sternemann, S. Holz, I. Kiesel, M. Tolan

CO_2 adsorption experiments on $[Zn_2(BME\text{-}bdc)_2(dabco)]_n$ thin films

D. C. F. Wieland, D. Zacher, S. Henke, C. Sternemann, M. Paulus, M. Tolan, R. A. Fischer

Protein Adsorbates on Hydrophobic Surfaces

H. Hähl, P. Loskill, A. Hoffmann, M. Klos, I. Kiesel, M. Paulus, C. Sternemann, M. Tolan, K. Jacobs

Exciton-mediated lattice distortions in InAs/GaAs quantum dots

S. Tiemeyer, M. Bombeck, M. Paulus, C. Sternemann, F. Wirkert, M. Bayer, M. Tolan

The interface between a solid and a supercritical gas

S. Holz, M. Paulus, J. Nase, T. Brenner, C. Sternemann, M.Tolan

Laser-induced lattice distortions in CdSe/CdS core/shell quantum rods

S. Tiemeyer, M. Bombeck, M. Paulus, C. Sternemann, J. Nase, M. Bayer, M. Tolan

Pressure dependent structure of silkworm silk fibroin nanocrystals

C. Krywka, F. Kunze, C. Sternemann, M. Müller

Correlation of the particle behavior, microstructure and phase evolution during the optimization of HVOF sprayed WC-12Co coatings by means of DoE

W. Tillmann, L. Hagen, I. Baumann, M. Tolan, M. Paulus, F. Wieland

Probing the interaction potential of proteins in solution

J. Möller, M. A. Schroer, M. Erlkamp, S. Grobelny, M. Paulus, M. Tolan, R. Winter

Verification of carbide-nitride transformation in a cold work tool steel powder by means of synchrotron radiation

K. Zumsande, N. Krasokha, S. Huth, S. Weber, W. Theisen

New beamline BL10

K. Istomin, A. Hüsecken, S. Balk, R. Wagner, D. Lützenkirchen-Hecht

Commissioning and first experiments at the PEEM at the TGM Beamline 12

C. Keutner, U. Berges, C. M. Schneider, C. Westphal

Investigation of the three layer system MgO/Fe/GaAs(001)

D. Handschak, F. Schönbohm, T. Lühr, S. Döring, D. Weier, C. Keutner, U. Berges, C. Westphal

Magneto-Optical Polarization Spectroscopy at the Co 3p edge

M. F. Tesch, M. C. Gilbert, H.-Ch. Mertins, D. Bürgler, C. M. Schneider

Thermal stability of ultra -thin HfO_2 films and structure determination of $HfSi_2$ islands on Si(110)

F. Schönbohm, C. D. Weier, T. Lühr, K. Skaja, S. Döring, U. Berges, C. Westphal

Generation of ultrashort VUV and THz pulses at the DELTA storage ring using coherent harmonic generation (CHG)

M. Bakr, M. Höner, H. Huck, S. Khan, R. Molo, A. Nowaczyk,
A. Schick, P. Ungelenk, and M. Zeinalzadeh

Introduction

Over the past decades, intense research has been focused on the evolution of the electronic excitations of atoms, molecules, and solid systems in the energy-momentum space, whereas much less work on the time scale of such excitations has been performed due to the rareness of time-resolved experimental techniques. Access to such electron dynamics, which take place on the pico- to femtosecond time scale, is solely provided using a time-resolved pump-probe scheme (Fig. 1).

Synchrotron radiation has a typical pulse duration of about 100 ps (FWHM), given by the electron bunch length, whereas commercial ultrafast lasers have pulse durations of about 30 fs, but their wavelengths are in the near-visible regime. For high-resolution time-resolved pump-probe experiments, the synchrotron pulse duration has to be compatible with the laser pulse duration, i.e. on the femtosecond scale. This can be achieved through several ways, among which the most prominent are linac-based free electron lasers (FELs). In conventional synchrotron light sources, short pulses can be generated by combining long bunches with femtosecond laser pulses using the so-called coherent harmonic generation (CHG) scheme which will be presented here [1-6].

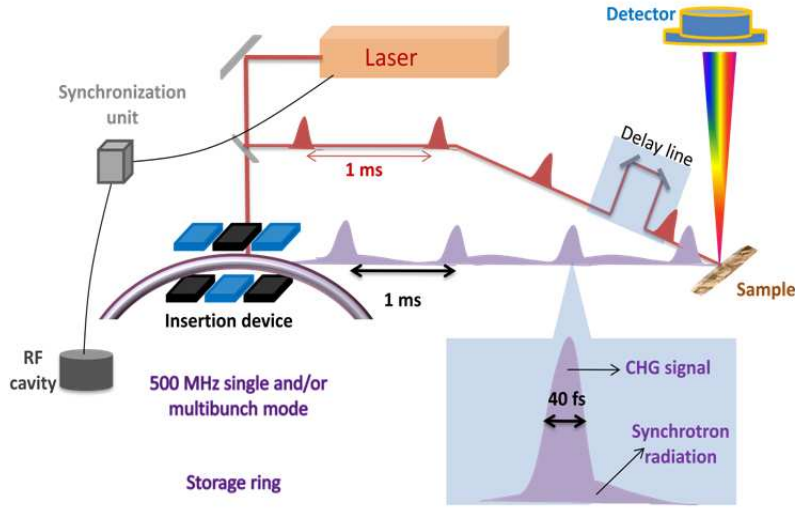

Fig. 1: Pump-probe scheme. Laser and synchrotron radiation pulses are focused on the same spot on the sample at a time delay Δ*t* determined by a delay line that is adjusted by the path of the pump beam. Afterwards, signals containing information on the intrinsic dynamics of the system are recorded by the detector.

CHG at DELTA

The DELTA facility at the TU Dortmund University is a synchrotron light source with a ring circumference of 115.2 m (Fig. 2) and a nominal beam energy of 1.5 GeV. The electromagnetic undulator U250, previously used as storage-ring FEL, can be used in an optical-klystron configuration (i.e., two undulators separated by a dispersive chicane) and is ideally suited for the CHG scheme (Fig. 3).

As the laser pulse is sent into the first undulator (modulator) and co-propagates with an electron bunch, a sinusoidal energy modulation of the electrons with a periodicity of the laser wavelength will occur if the resonance condition $\lambda_L = \lambda_U/2\gamma^2\,(1+K^2/2)$ is fulfilled. Here, λ_L is the laser wavelength, λ_U is the undulator period length, K is the deflection parameter of the modulator, and γ is the Lorentz factor of the electrons. This process requires temporal overlap enabled by synchronizing the laser to a subharmonic of the accelerating radio frequency. Since the laser pulse is typically one thousand times shorter than the electron bunch, only a small fraction (slice) of the bunch is modulated. After the modulator, electrons pass through the chicane where the electrons with different energies travel along different paths, resulting in a density modulation (microbunching). Finally, the microbunched electrons travel through the second undulator (radiator) emitting coherent, femtosecond radiation which is more intense than that radiated from the whole bunch (Fig. 4).

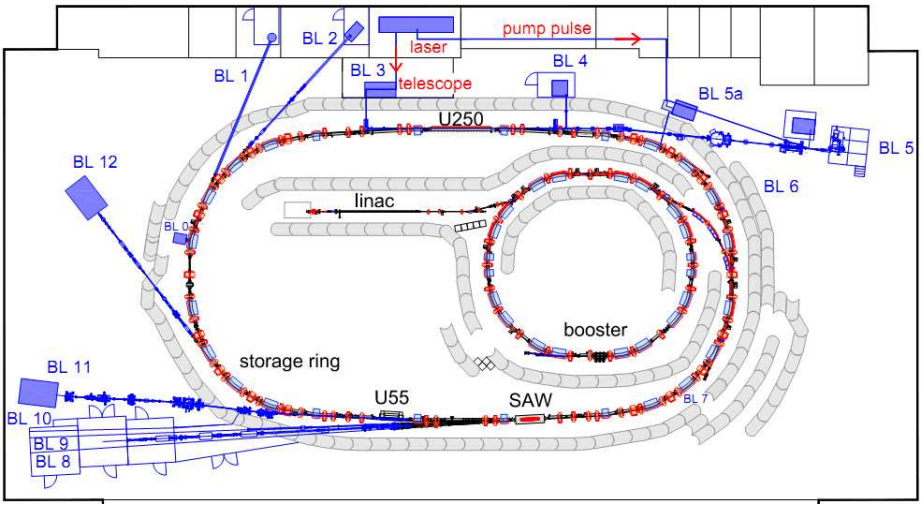

Fig. 2: Schematic diagram of the DELTA synchrotron radiation facility.

The radiated power from the electron slices at the *n*th harmonic of the laser wavelength scales with the squared number of bunched electrons as $P(\omega) \sim N^2 b_n^2(\omega)$, where N is the number of electrons in the slice. The bunching factor b_n describes the degree of microbunching with $0 \le b_n \le 1$ and decreases exponentially with increasing the harmonic order [7].

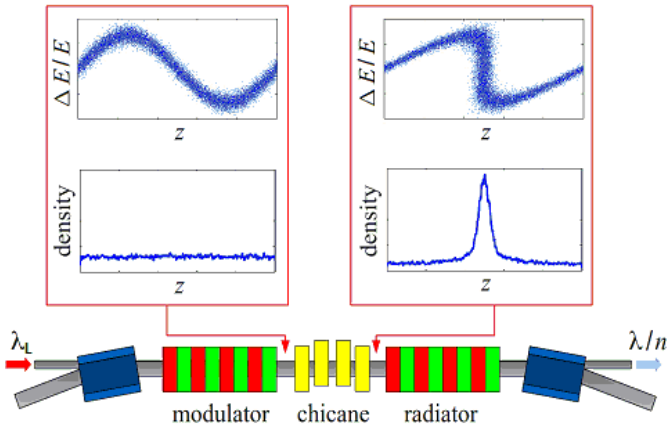

Fig. 3: Schematic diagram of the CHG scheme with two undulators and one chicane. The longitudinal phase space diagrams show the electron distribution before and after the chicane.

Several meters after the modulator, a narrow gap in the longitudinal charge distribution develops since off-energy electrons have moved ahead or lagged behind. In a dipole magnet, such a gap gives rise to coherent radiation in the THz regime with a broad spectrum and sub-ps pulse duration [8, 9].

Experimental Setup

A Ti:Sapphire laser system is used to deliver pulses of wavelength λ_L = 795 nm with a pulse energy up to 8 mJ and duration of about 40 fs at a repetition rate of 1 kHz. The laser pulse is sent into the undulator U250 via a telescope located at the beamline BL3 (Fig. 2). Before the undulator, two remotely controlled mirrors allow the adjustment of laser position and angle. Two screens can be moved into the laser path for transverse diagnostics. Due to the installation of new power supplies, the electromagnetic undulator U250 allows to tune the modulator, the chicane, and the radiator independently. Using a water-cooled copper mirror approximately 5 meters after the U250, laser and synchrotron radiation is guided into beamline BL4, where the transverse and longitudinal overlap between laser and electrons is established using CCD cameras, photodiodes and a streak camera. A dedicated THz beamline (BL6) was built for detecting the THz pulses generated downstream of the undulator (Fig. 2). These pulses are detected and recorded using a liquid-He-cooled bolometer together with a 1 GHz oscilloscope. The strength of the THz pulses gives an indication of the quality of the overlap. This beamline will be shortly equipped with a new high-resolution Fourier-transform spectrometer for studying the THz pulse characteristics as well as for far-IR spectroscopic studies with high time resolution.

The CHG radiation is guided to the experimental station at beamline BL5 operated by the Forschungszentrum Jülich. For pump-probe experiments, a fraction of each laser pulse will be sent to an optical station located before BL5 and focused onto the sample at BL5 with a well-defined time delay (Fig. 2).

Results

Two months after the installation of the laser and THz beamlines (March 2011), the first coherent THz and CHG pulses were observed in single-bunch mode (Fig. 4). A few shifts later, an electron orbit that complies with both user and CHG operation was established, and CHG was successfully observed at about 400 nm (i.e. at the second harmonic of the seeding laser) during user shifts with a multi-bunch filling pattern (Fig. 4a). The spectral bandwidth (FWHM) is found to be about 5 nm, indicating a time-bandwidth product close to the Fourier limit. The coherent nature of this radiation is seen by the quadratic dependence of the radiation power on the electron beam current (Fig. 4b).

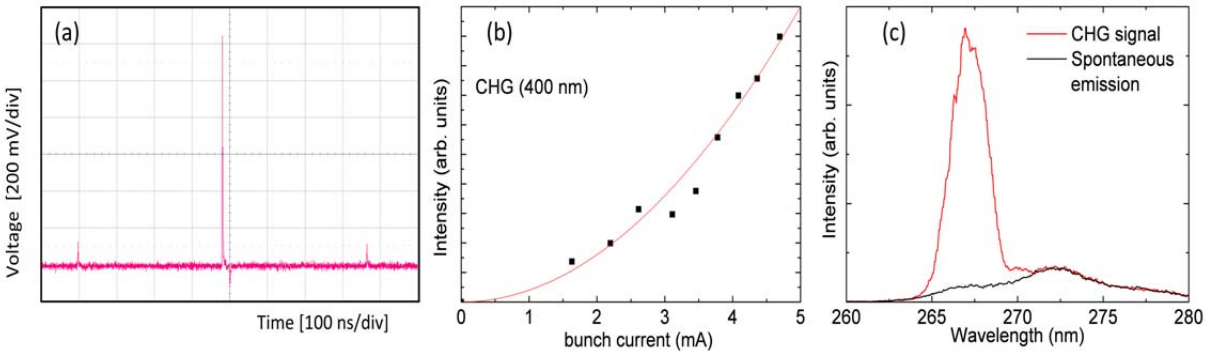

Fig. 4: (a) Oscilloscope image of the undulator radiation showing three revolutions in single-bunch mode. The central peak contains the CHG signal at the second harmonic of the seeding laser. (b) Quadratic dependence of the CHG signal on the beam current. (c) Spontanuous emission spectrum with CHG signal at the third harmonic of the seeding laser (red) and without CHG signal (black).

Other improvements of DELTA

Improvements to the injection efficiency of electrons into the storage ring have been recently made by installing a new electron gun and kicker pulsers. The new gun allows fast switching between single- and multiple bunch injection as well as a hybrid fill pattern. The beam lifetime has recovered from replacing vacuum chambers in the winter shutdown and is improved by better alignment of magnets and vacuum chambers. Much effort has been put to establish longitudinal and transverse bunch-by-bunch feedback systems that suppress undesired collective multi-bunch instabilities. Along with that, progress is being made now in installing a fast orbit correction scheme.

Outlook

Apart from general improvements of the machine, the commissioning of the new short-pulse facility is in good progress. CHG radiation at the third harmonic of the seeding laser has been recently observed (Fig. 4c). Much effort is now being put to generate shorter wavelengths. Firstly, the modulator will be seeded with the second and third harmonics of 800 nm using a nonlinear frequency conversion unit. Secondly, the radiator parameters will be tuned to generate CHG pulses at higher harmonics of that seeding wavelength (e.g. λ = 53 nm being the fifth harmonic of a seed pulse at 265 nm).

Other short-pulse methods are planned to be implemented at DELTA, particularly the echo-enabled harmonic generation (EEHG) [7] scheme which allows reaching higher harmonics of the seeding laser, thus shorter wavelengths compared to CHG. The currently-used straight section at the northern part of DELTA can be extended to implement the EEHG scheme by installing additional short undulators and magnetic chicanes upstream of the U250. Simulations for this configuration are in progress [10].

References:

[1] B. Girard *et al*., Phys. Rev. Lett. **53**, 2405 (1984).

[2] E. Allaria *et al*., Phys. Rev. Lett. **100**, 174801 (2008).

[3] M. Labat *et al*., Eur. Phys. J. D **44**, 187 (2007).

[4] S. Khan *et al.,* Synch. Rad. News **24**, 18 (2011).

[5] H. Huck *et al*. Proceedings of FEL2011, Shanghai, China (2011).

[6] A. Schick *et al*. Proceedings of IPAC2011, San Sebastián, Spain (2011), and references therein.

[7] G. Stupakov, Phys. Rev. Lett. **102**, 074801 (2009).

[8] K. Holldack *et al*., Phys. Rev. Lett. **96**, 054801 (2006).

[9] M. Höner *et al*. Proceedings of IPAC2011, San Sebastián, Spain (2011).

[10] R. Molo *et al*. Proceedings of FEL2011, Shanghai, China (2011).

Beamline BL-1: Deep X-Ray Lithography

Thorsten Brenner*, Daniela Lietz, Michael Paulus, Ulf Berges, Christian Sternemann, and Metin Tolan.
Fakultät Physik/DELTA, TU Dortmund, D-44221 Dortmund, Germany.
*email: thorsten.brenner@tu-dortmund.de

Beamline BL-1 is dedicated to deep x-ray lithography (DXRL). DXRL is a method to produce various microstructures with a height up to several millimeters. Microstructures are applied in optics, micro mechanics, fluidic, or medical devices. It is possible to reach a high aspect ratio of about 100 and a lateral resolution up to 2 µm for microstructures using DXRL [1].

A well-established process for production of microstructures using lithography is the LIGA process [2]. It includes the process steps (x-ray) lithography, electroplating, and molding. A wafer covered with a photo sensitive material (positive or negative resist) is exposed through a mask. This mask consists of an x-ray transparent material, e. g. carbon or titanium, and an absorber material, e. g. gold. The lateral shape of the absorber layer is transferred into the photoresist by shadow projection. Solely the exposed resist areas experience a chemical change regarding the molecular weight. After chemical development the exposed (positive resist) or unexposed (negative resist) material is removed. Afterwards, the micromechanical components can be produced by electroplating and molding.

Figure 1: 4-inch Wafer with microgear structure after exposure, post exposure bake and development.

At beamline BL-1 we exposed wafers with negative resist SU-8 with thickness of 550 µm. Systematic tests to find optimal parameters (e. g. mask material, dose, absorbing materials as filters to tune the x-ray spectrum, post exposure bake) for exposure have been started. Therefore, we have exposed wafer under different conditions. First, we exposed wafers with different radiation dose. Two different masks containing graphite or titanium as membrane material were used (see last user report). Currently, we continued with a new graphite mask. A photograph of a wafer exposed with this new mask is shown in figure 1 after its chemical development. Furthermore, we changed the ratio of top to bottom dose by adding kapton with maximum thickness of 400 µm as a filter material.

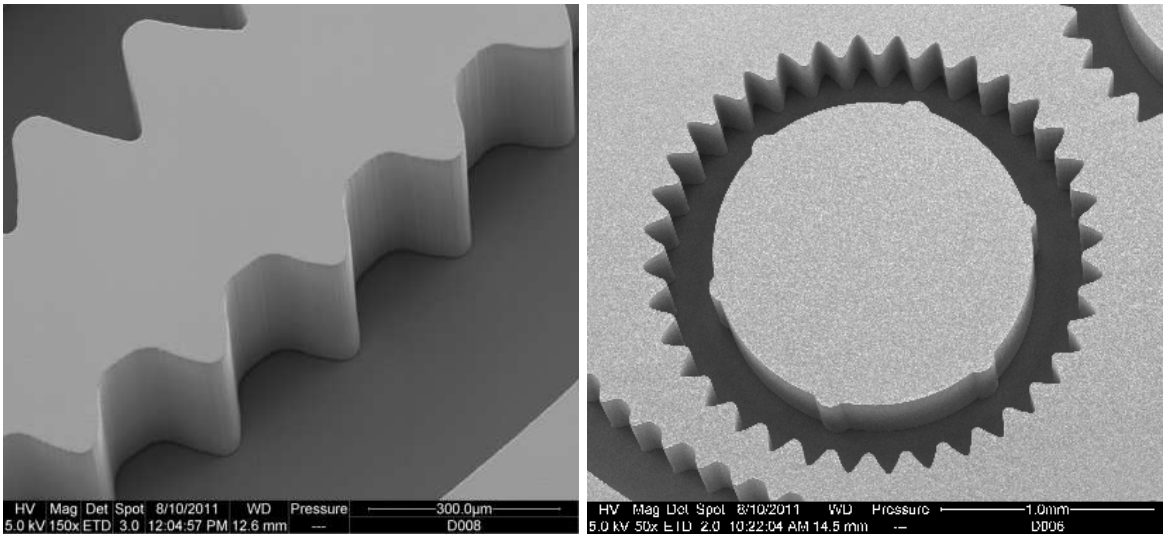

Figure 2: SEM images of the developed wafers exposed at BL-1.

Some results are shown in figure 2. The SEM images show developed wafers with microstructures. The structures exhibit high steepness of walls and sharp edges, but high sidewall roughness resulting from the graphite material of the mask. The adhesion between substrate and photoresist is good, because no gaps between them are visible. The aspect ratio can be determined to a maximum value of 10 in this case.
An update of hardware components is in progress. A roots pump will replace the turbomolecular pump. The new pump evacuates the endstation within five minutes (instead of 30 minutes before) reaching a minimum pressure of 10^{-2} mbar, which is adequate for DXRL applications. It will be installed in the end of 2011. Moreover a new endstation is under construction to improve the manageability and efficiency of the exposure. This will be realized by a goniometer turning the wafer stepper by 90° laterally, so that wafers can be placed easily onto the stepper through a new inlet opening in the side of the endstation. The installation of the new endstation is planed for spring 2012.

Acknowledgement
We would like to thank Dr. Alex von Bohlen (Leibniz-Institut für Analytische Wissenschaften - ISAS - e.V.) for taking the SEM images. We also would like to thank the DELTA machine group for providing synchrotron radiation and for technical support. T. Brenner thanks the NRW Forschungsschule 'Forschung mit Synchrotronstrahlung in den Nano- und Biowissenschaften' for financial support.

References

[1] V. Saile, U. Wallrabe, O. Tabata, J.G. Korvink, O. Brand, G.K. Fedder, C. Hierold (Eds.), *LIGA and its applications*, Wiley-VCH (2009).

[2] *http://www.imt.kit.edu/liga.php*

Spin- and angle-resolved PES on Bi_2Te_3 / Si(111) thin films at BL5

A. Herdt[1], L. Plucinski[1], S. Döring[2] , G. Bihlmayer[1], and C.M. Schneider[1,2,3]

[1]*Peter Grünberg Institut (PGI-6), Forschungszentrum Jülich*
[2]*Universität Duisburg-Essen, AG Prof. Dr. C.M. Schneider*
[3]*Jülich Aachen Research Alliance-Fundamentals of Future Information Technologies (JARA-FIT)*

Topological insulators (TIs) have been proposed as a new state of quantum matter providing spin-filtered Dirac fermions on the surface present within an energy gap [1,2]. Characterized by an odd number of massless Dirac cones, the surface states show linear energy dispersions related to relativistic Dirac fermions with an intrinsic spin locked to its translational momentum [2,3]. Contrary to ordinary Dirac fermions in graphene, the Dirac fermions in TIs show a net spin-polarization and thus are guaranteed to be conducting due to the time-reversal symmetry [2]. TIs with strong spin-orbit interaction, e.g. $Bi_{1-x}Sb_{-x}$, Bi_2Se_3, and Bi_2Te_3, are supposed to be potential candidates for new spintronic devices or quantum computing applications [1].

Photoelectron spectroscopy represents a surface sensitive method for studying the electronic states located within a few nm off the surface [4]. The combination of angle- and spin-polarized photoemission spectroscopies SP-ARPES has become one of the important methods to observe the physical properties of the TIs. Recently, we have confirmed the robustness of the topological Bi_2Te_3 thin film surface after air-exposure and subsequent *in-situ* sputter-anneal cleaning procedure under ultra-high vacuum (UHV) conditions [5]. As a result, clear Dirac-cone features observed in high-resolution ARPES spectra were found to be insensitive against cleaning-induced surface roughness.

In this report we present angle- and spin-resolved measurements on epitaxial MBE-grown Bi_2Te_3/Si(111) thin films [6] carried out at BL5 using linear polarized light (*hv* = 24 eV). Bi_2Te_3 crystallizes in a layered rhombohedral structure with the space group $D_3^5(R\bar{3}m)$, see Fig. 1 (a). The basic unit cell is five atomic layers thick, a so-called quintuple layer (1QL ≈ 1nm). The crystal is characterized by a strong covalent bonding within the QL. The QLs are stacked in the sequence Te1-Bi1-Te2-Bi1'-Te1' along the z-direction with weak van der Waals bonding between the stacks, see Fig. 1 (b). The irreducible Brillouin zone and its projection onto the surface are shown in Fig. 1 (c).

Prior to the measurements, a 10x10 mm² sample was cut from the wafer *ex-situ* and transferred to the UHV preparation chamber (base pressure ≈ 1E-10 mbar). Next, the thin film was cleaned by means of several Ar-ion (500eV) sputtering and annealing cycles with details of the procedure explained in Ref. [5]. Crystalline order and surface cleanliness were checked using Auger-electron spectroscopy and low-energy electron diffraction methods. Finally, the sample was transferred to the SP-ARPES - machine and mounted on a commercial six axis liquid nitrogen cooled manipulator. The experimental end-station includes a commercial VG

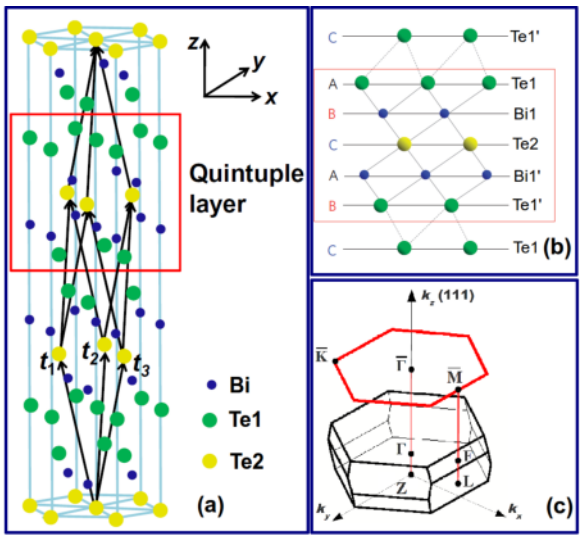

Figure 1: (a) Layered crystal structure of Bi_2Te_3. 1QL represents five atomic layers. (b) Schematic representation of 1QL sequence along the z-axis, taken from [2]. (c) Projection of the bulk zone onto the surface.

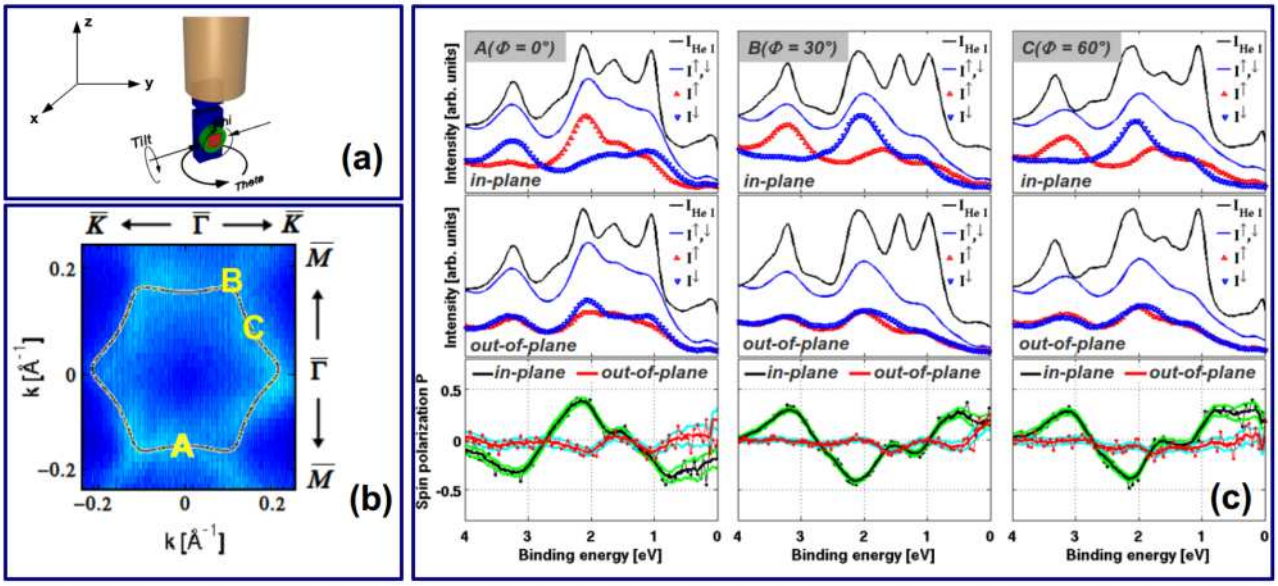

Figure 2: (a) Experimental geometry of the installed six axis liquid nitrogen cooled manipulator. (b) Measured Fermi surface using linear polarized light (hν=24eV). A to C represent the azimuthal angle positions A(Φ=0°), B(Φ=30°) and C(Φ=60°). (c) Spin-resolved photoemission on a Bi_2Te_3/Si(111) thin film. The top row indicates the in-plane spin-vector components, while the out-of-plane components are plotted in the middle row. In the bottom row the deduced spin-asymmetries P_x and P_z are indicated by black and red solid lines. Standard deviations are represented by envelopes (blue and red) obtained from the corresponding spin asymmetry error values.

Scienta SES 2002 hemispherical spectrometer equipped with a combination of an optimized high transmission spin-polarized low-energy electron diffraction (SPLEED) [7,8] detector and a two-dimensional delay-line-detector (DLD) system [9]. This custom configuration permits the semi-simultaneous detection of a 1D spin-resolved energy-distribution curve (EDC) and a 2D angular map. In spin-resolved mode the spin-polarization vector components P_x and P_z for in- and out-of-plane directions of the spin vector can be obtained simultaneously. Fig. 2 (b) shows a measured hexagonal Fermi surface of the Bi_2Te_3 thin film. In order to proof the intrinsic helical spin texture of the Dirac fermions, the sample was rotated to three different azimuthal ***k***-point positions denoted by A(Φ=0°), B(Φ=30°) and C(Φ=60°). As can be seen from Fig. 2 (c) there is a clear reversal of the spin-polarization for the in-plane components between the positions A and B which has its maximum values around ± 45%. In addition, the out-of-plane component also shows spin reversals with magnitudes of ± 9%. The spin-asymmetry values were calculated from the partial channeltron intensities of the SPLEED detector. These observations are well confirmed by our *ab initio* Full Potential Linearized Augmented Plane Wave Method (FLAPW) calculations as well as complementary studies on similar samples. We have shown that in Bi_2Te_3 thin films high spin-polarized states reside not only at low binding energies as shown on Bi_2Te_3 single crystal samples [10], but also can be found in the extended binding energy regime up to 4 eV. From the practical point of view, the incorporation of high quality MBE-grown TI thin films into spintronic devices is more favorable than the implementation of single crystals. Thus, thin films exhibiting the topological properties are potential candidates for future spintronic or quantum computation applications. Our spin-resolved data are supported by additional high-resolution photoemission measurements of the energy band dispersions using ARPES at BL5.

References

[1] E. Moore, Nature (London), **464**, 194 (2010)

[2] H. Zhang *et al*.: Nat. Phys. **5**, 438 (2009)

[3] Y. L. Chen *et al*.: Science **325,** 178 (2009)

[4] C.M. Schneider *et al*.: J. Electron Spectrosc. Relat. Phenom., **51**, 263 (1990)

[5] L. Plucinski *et al*.: Appl. Phys. Lett. **98**, 222503 (2011)

[6] J. Krumrain *et al*.: J. Cryst. Growth **324**, 115 (2011)

[7] J. Kirschner *et al*.: Phys. Rev. Lett. **42**, 1008 (1979)

[8] D. Yu *et al*.: Surf. Sci. **601**, 5803 (2007)

[9] L. Plucinski *et al*.: J. Electron Spectrosc. Relat. Phenom., **181**, 215 (2010)

[10] S. Souma *et al*.: PRL **106**, 216803 (2011)

XAFS at the liquid air interface

Steffen Bieder*,[a], D.C. Florian Wieland[a], Johannes Möller[a], Ralf Wagner[c], Michael Paulus[a], Christian Sternemann[a], Patrick Degen[b], and Metin Tolan[a]
[a] *Fakultät Physik/DELTA, TU Dortmund, D-44221 Dortmund,*
[b] *Physikalische Chemie II, TU Dortmund, Otto-Hahn-Str. 6, D-44221 Dortmund*
[c] *Fakultät Physik, Bergische Universität Wuppertal, Gaustr. 20, 42097 Wuppertal*

*email: Steffen.Bieder@uni-dortmund.de

Composite materials formed by nature show a hierarchical organized and complex structure. The biomineralization process for instance is controlled by proteins and the chemical environment [1, 2, 3]. Studies on different systems show that the formation process is influenced by electrostatic interactions, geometric matching and stereochemical correspondence [4, 5, 6].
In this study the crystallization of iron oxide at the aqueous solution-air interface is investigated by X-ray absorption fine structure (XAFS) experiments. The interface properties were manipulated by employing varying amphiphilic Langmuir layers. Two kinds of subphases were used in order to investigate the influence of different salts on the mineralization process. Subphases containing 100 mmol of iron(II)- and iron(III)-chloride were utilised. Amphiphilic molecules of steric acid and stearyl alcohol were used to model negativly charged and almost neutral interfaces, respectivily. In the case of iron-salt solutions the biomineralization process is triggered by a change of the pH value. Due to this ammonia is added to the gas phase above the sample in order to start the mineralization process. The diffusion of ammonium to the liquid interface causes a pH change in the following.

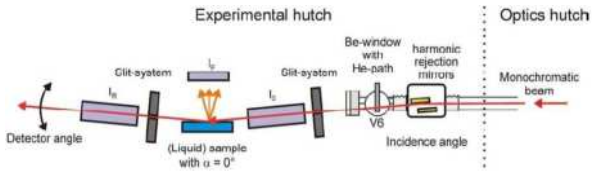

Fig. 1: Scetch of the experimental setup at Beamline BL8. The photon beam is bend down on the sample surface by the harmonic rejection mirror. The incident angle was adjusted to 0.1°. [7]

The experiment took place at beamline BL8 at DELTA investigating the iron K-edge. For the measurement the beam had to be bent down on the liquid surface by using a deflection mirror, resulting in an incident angle of 0.1° (see figure 1). At the sample stage a Langmuir trough with a helium flushed housing was installed. After preparing the sample system several EXAFS measurements were taken from the system in order to study the initial state of the sample system. After this ammonia was added to the athmosphere to start the mineralisation process. The ongoing process was measured by several XANES scans until the system reached a steady state. This procedure was necessary because EXAFS measurements least 6-8h. In order to prevent artifacts due to a ongoing mineralization the system had to reach a stable state. After the XANES measurements showed no changes anymore the end state was characterized by EXAFS scans.

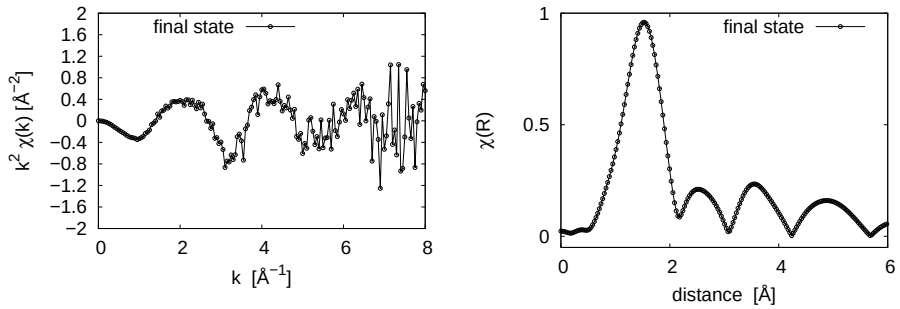

(a) (b)

Fig. 2: a) Extracted EXAFS signal of an 100 mM iron(II)chloride solution with a stearyl alcohol monolayer present at the interface and a surface pressure of $\Pi = 20\ \frac{\mathrm{mN}}{\mathrm{m}}$. b) Fourier transformed EXAFS signal χ(R). The data was measured in the final state of the sample system.

Figure 2a shows the final state of an 100 mM iron(II)-chloride solution with a stearyl alcohol monolayer present at the interface. The surface pressure was adjusted to $\Pi = 20\ \frac{\mathrm{mN}}{\mathrm{m}}$. The signal is very noisy because of the small amount of crystalline material. Figure 2b shows the χ(R) of the probe, which was calculated by a fourier transformation of the EXAFS signal. It can be seen that the iron atoms are surrounded by a single coordination shell with a radius of 1.7 Å. From this data it can be deduced that no iron oxide mineralization takes place.

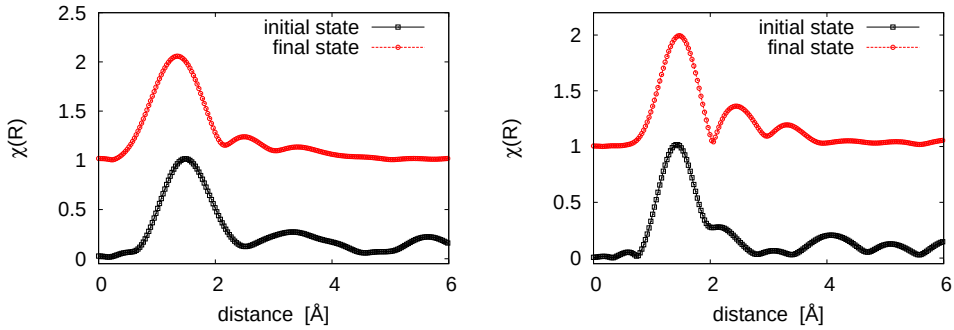

(a) (b)

Fig. 3: a) χ(R) of an 100 mM iron(III)chloride solution with a stearic acid monolayer present at the interface and a surface pressure of 10 $\frac{\mathrm{mN}}{\mathrm{m}}$. b) χ(R) of the same system with an surface pressure of 20 $\frac{\mathrm{mN}}{\mathrm{m}}$. In both system the develop of a second peak at a radius of 2.3 Å could be observed.

Further a 100 mM iron(III)chloride solution was investigated were a steric acid monolayer was deposit at the interface. The measurements were made at two different surface pressures of $\Pi = 10\ \frac{\mathrm{mN}}{\mathrm{m}}$ and $20\ \frac{\mathrm{mN}}{\mathrm{m}}$. In figure 3a the initial and final states of the system with an surface pressure of $10\ \frac{\mathrm{mN}}{\mathrm{m}}$ are shown. Slightly differences between the two states can be seen. The oszillation above 2 Å in the data from the initial state can be attributed to noise. The few iron molecules present at the interface result in a low signal to noise ratio. In the final state the appearence of a second coordination shell is hinted at 2.3 Å.The observed changes were more pronounced by increasing the surface pressure to $\Pi = 20\ \frac{\mathrm{mN}}{\mathrm{m}}$, see figure 3b. Again in the initial state the iron atom is surrounded by a single coodination shell. This changes after ammonia is added and a second shell develops at 2.3 Å.

References

[1] H.A. Lowenstamm, S. Weiner, *On Biomineralization*; Oxford: New York, 1989.

[2] L. Addadi, S. Weiner, *Angew. Chem., Int. Ed. Engl.* **1992**, 31, 153.

[3] L. Addadi, S. Weiner, *Proc. Natl. Acad. Sci. U.S.A* **1985**, 82, 4110.

[4] E.M. Landau, M. Levanon, L. Leiserowitz, M. Lahav, J. Sagiv *Nature* **1985**, 318, 353.

[5] S. Mann, D. Archibald, J.M. Didymus, T.Douglas. B.R. Heywood, F.C. Meldrum, N.J. Reeves *Science* **1993**, 261, 1286.

[6] J.H. Fendler *Chem. Mater.* **1996**, 8, 1616.

[7] D. Lützenkirchen-Hecht, T. Heim, S. Rutkowski, R. Wagner, R. Frahm *Fifth DELTA User-meeting Reports*, **2009**

Hydration properties of micelles

Martin A. Schroer*,[a], Christoph J. Sahle**,[a], Jens Smiatek[b], Patrick Degen[c], Christian Sternemann[a], and Metin Tolan[a]

[a] *Fakultät Physik/DELTA, TU Dortmund, Maria-Goeppert-Mayer-Str. 2, D-44227 Dortmund, Germany;*

[b] *Institut für physikalische Chemie, Westfälische Wilhelms Universität Münster, Corrensstr. 28/30 D-48149 Münster, Germany;*

[c] *Fakultät Chemie/ Physikalische Chemie II, TU Dortmund, Otto-Hahn-Str.6 ,D-44227 Dortmund, Germany*

*email: martin.schroer@tu-dortmund.de ; **email: christoph.sahle@tu-dortmund.de

The structure of water in close vicinity to hydrophilic and hydrophobic interfaces has been shown to exhibit a fairly different structure compared to the bulk phase. Due to the differing structure of the water network in these relevant geometries different physical properties have been proposed and were found both in experimental and via simulation studies [1, 2, 3]. In this context the local structure of water near to mesoscopic surfaces which have a high relevance for many chemical and biological processes is largely missing.

Particle systems that are on these length scales and which are in doubt to affect the water structure due to their effective charge are micelles [4]. This type of aggregates formed beyond a critical temperature from surfactant molecules exhibited a complex phase diagram that depends on the solutions temperature and micelle concentration. Moreover, increasing the micelle concentration allows to enhance the population of hydration water to bulk water.

The micelle studied are made of CTAB (cetyl trimethylammonium bromide) which contains a bromide atom. To reveal the effect on the water structure, X-ray Raman scattering (XRS) measurements were conducted at ID16, ESRF, on the oxygen K-edge. As the scattering cross-section of this technique is relatively low, additional X-ray absorption fine structure (XAFS) measurement were performed at BL8, DELTA, at the Br K-edge. This approach allows is to study both the effect of the charged micelle as well as of the dissociated bromide ion on the water structure.

Fig. 1 shows the Br K-edge for CTAB micelles at different temperatures as well as of the dry CTAB powder. In order to reveal if the bromide ion is located close to the charged micellar surface, additional measurements on equimolar potassium bromide solutions were performed. As for the latter a fully dissociation is present, comparison of both XAFS signals will allow to access the local hydration structure of the bromide. The data analysis is still in progress.

In addition, all-atom Molecular Dynamics (MD) simulations of CTAB layers in contact with explicit water molecules were done. The so-obtained microscopic structure coordinates can be used to calculate the corresponding XRS and XAFS signals and thus allow a detailed comparison with the experimental data. This approach therefore will give a deeper insight into the local hydration structure close to the micelles' surface.

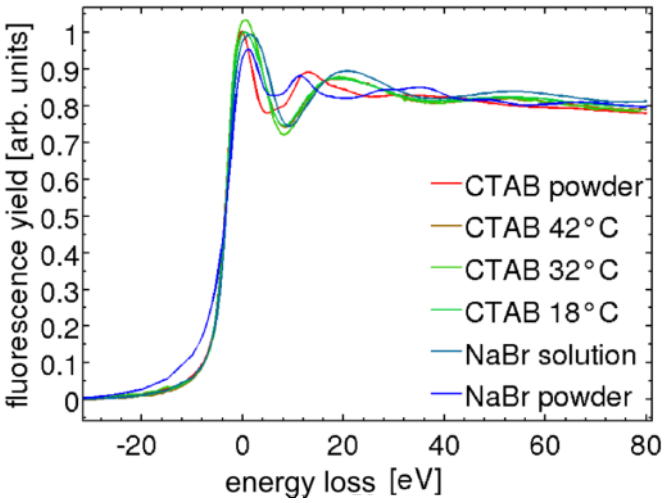

Figure 1: Fluorescence yield of different CTAB and KBr samples at the Br K-edge in terms of relative energy loss.

The authors like to acknowledge the BL8 crew and the DELTA machine group for providing synchrotron radiation and technical support.

References

[1] S.H. Lee, P.J. Rossky, *J. Chem. Phys.* **100**, 3334 (1994).

[2] L. Cheng, P. Fenter, K.L. Nagy, M.L. Schlegel, N.C. Sturchio *Phys. Rev. Lett.* **87**, 156103 (2001).

[3] J. Israelachvili, H. Wennerstrom, *Nature* **379**, 219 (1996).

[4] R. Hargreaves, D.T. Bowron, K. Edler, *J. Am. Chem. Soc.* **133**, 16524 (2011).

In depth profiling by GIXRF of ion-implanted Si-wafers

Alex von Bohlen, Martin Brücher, Roland Hergenröder
Leibniz-Institut für Analytische Wissenschaften – ISAS – e.V.
Bunsen-Kirchhoff-Str. 11
44139 Dortmund

Ion-implanted materials have some tradition in microelectronics when shallow junctions are necessary after the chip production. Several methods - preferably destruction free options - have been used in the resent past for the characterization of the implanted material [1, 2]. One promising way was the grazing incidence X-ray fluorescence (GIXRF). However, some open questions of the proposed method and its capabilities have to be worked out before starting with routine analyses.

Therefore, a set of ion-implanted Si-wafers ⟨100⟩ was characterized using GIXRF at DELTA BL 8. The implanted ions of Co and Zn have nominal area densities of i) Co^+ 1E17/cm² ii) Co 1E16/cm² and Zn 1E16/cm², and iii) Zn^+ 0.49E17/cm² and Co^+ 1E17/cm². In order to produce buried material profiles of some hundreds of nm depth implantation energy of 100keV was chosen. GIXRF spectra and X-ray reflectivity scans were recorded at 10 keV, 12 keV and 15.5 keV primary energies at BL8. The fluorescence radiation was collected directly above the sample using an AMPTEK XR 100 SDD detector.

The expected advantage of GIXRF is on the one hand the consumption free characterization of the material and on the other hand the fast analytical procedure when comparing with other methods of surface analyses. However, some work has to be invested to determine the limitations of GIXRF for the proposed application.

In this report we show our first result despite the final decision is still open if the method will be helpful for the characterization of non-discrete layers of ion-implanted material. Our first observation was the different slope of the GIXRF signals in relation to the implantation dose (Fig. 1).

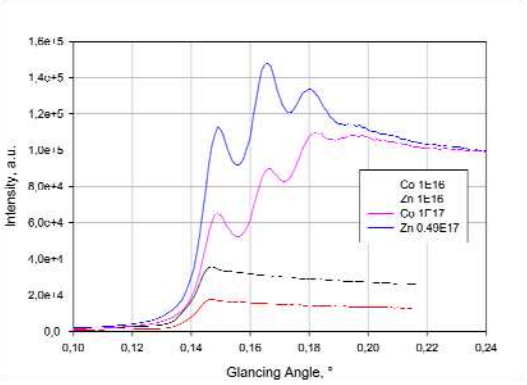

Figure 1. Co- and Zn-ions implanted in Si-wafer. Different slops of the GIXRF can be observed in dependence of the dose.

In the case of higher implantation doses the excitation radiation undergoes interference and affects the complete energy range of the fluorescence radiation. Simulations are in preparation (cf. Fig.2).

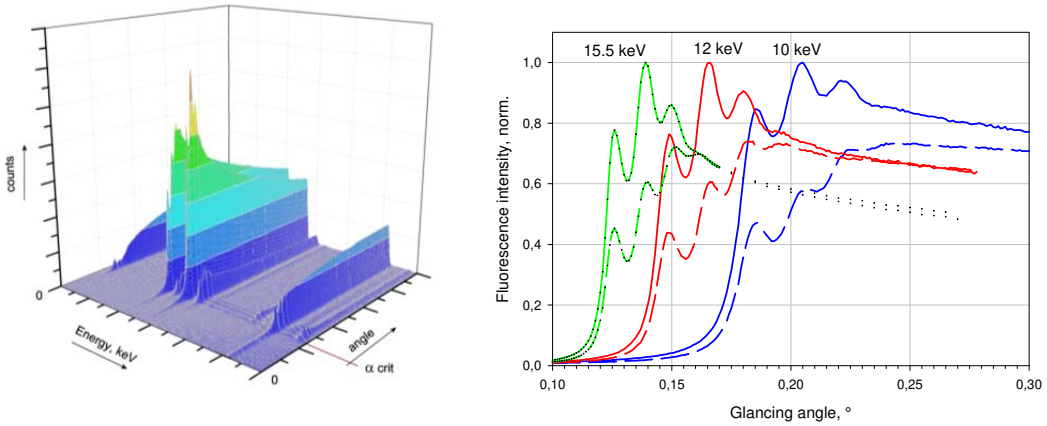

Figure 2. GIXRF fluorescence spectra of high dose ion-implanted materials.

An independent determination of the in-depth distribution of the implanted material was achieved by X-ray Photoelectron Spectroscopy with Ar^+ ion-sputtering (XPS-AES). The implantation profiles of the implanted materials show clear differences. Co was implanted first and in a second run, Zn was implanted. In comparison to single element ion implantation profiles of Co implanted in Si-wafers, the Co-ions were pressed into deeper regions while implanting Zn after Co. A quantitative evaluation of the in-depth distribution was possible after determining the deepness of the sputter craters. For this purpose a white-light interferometer was used (cf. Fig 3).

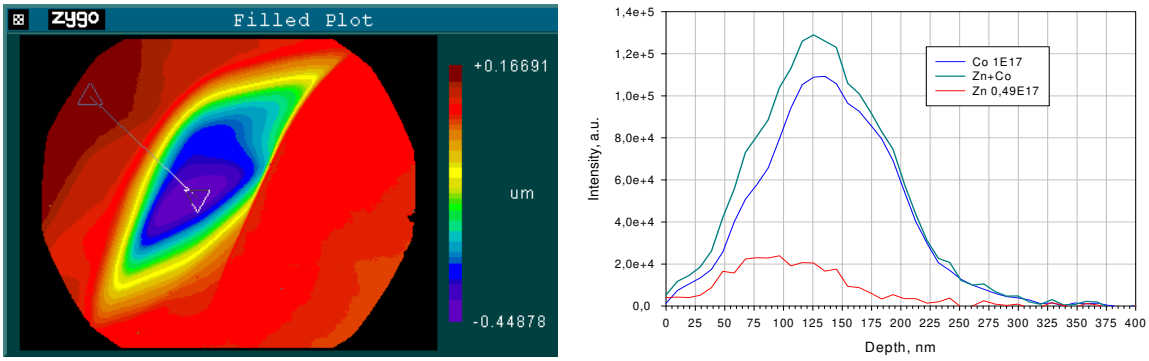

Figure 3. Left: White-light interferogram of a XPS-AES crater, right: Depth-profiles of implanted Cobalt and Zinc ions in a Si-wafer.

Literature

1. R. Klockenkämper, H. W. Becker, H. Bubert, H. Jenett, A. von Bohlen. Depth Profiles of a shallow implanted layer in a Si-wafer determined by different methods of thin-layer analysis. Spectrochim Acta B 57 (2002) 1593-1599.
2. Lara Lobo, Beatriz Fernandez, Rosario Pereiro, Nerea Bordel, Evgeny Demenev, Damiano Giubertoni, Massimo Bersani, Philipp Hönicke, Burkhard Beckhoff, Alfredo Sanz-Medel. Quantitative depth profiling of boron and arsenic ultra low energy implants by pulsed rf-GD-ToFMS. J. Anal. At. Spectrom., 26 (2011) 542- 549.

Local atomic and electronic structure of Ag clusters deposited in a polydimethylsiloxane (PDMS) matrix

Sabrina Hoffmann*,[a], Stefanie Duffe[a], Kamil Latussek[a], David Engemann[a], Stefan Balk[b], Ralph Wagner[b], Christian Sternemann[c], Michael Paulus[c], Christoph J. Sahle[c], Martin A. Schroer[c], and Heinz Hövel[a]

[a] *Fakultät Physik/Experimentelle Physik I, TU Dortmund, Otto-Hahn-Str. 4, 44221 Dortmund, Germany;*
[b] *Bergische Universität Wuppertal, Fachbereich C, Fachgruppe Physik, Gaußstr. 20, 42119 Wuppertal, Germany;*
[c] *Fakultät Physik/DELTA, TU Dortmund, Maria-Goeppert-Mayer-Str. 2, 44227 Dortmund, Germany;*

*email: sabrina.hoffmann@physik.uni-dortmund.de

In this report we describe first results of our x-ray absorption near edge structure (XANES) spectroscopy measurements at the Ag L_3 absorption edge of Ag clusters in a polydimethylsiloxane (PDMS) matrix compared to Ag and Ag_2O reference samples as well as to Ag clusters on SiO_2 substrates performed at beamline BL8 of the synchrotron radiation facility DELTA, TU Dortmund.
Clusters assembled materials are of great impact for future applications in science and nanotechnology [1, 2, 3]. In particular, advances in metal cluster-beam technology allow experiments on free and supported or embedded clusters resembling nanostructures in realistic, technical relevant environments. Optical properties of noble metal clusters and nanostructures such as their UV-VIS absorption band alter significantly with size, shape, and interparticle spacing as well as with the properties of the local environment. This yields a wide range of further applications such as optical biosensors [4] or metal nanoantennas as promising systems for field-enhanced spectroscopy or nanoscopic light emitters [5]. XANES yields unique structural and chemical information on supported and embedded clusters. It is well suited to investigate the chemical environment of noble metal clusters and allows the study of changes of the unoccupied density of states (uDOS). The focus of our study is set on the following two topics:

(i) The uDOS of clusters is different from that of bulk Ag which manifests depending on their size in quantized or bulk-like properties. Thus, the uDOS is strongly influenced by the size which is under investigation. Starting with Ag clusters of 2 nm size produced with THECLA (Thermal CLuster Apparatus) [6] we investigate sample positions with different cluster coverage. For increasing coverage particles larger than 2nm are formed by coalescence.
(ii) It is well known that exposure to air after sample preparation leads to a partial oxidation / sulfidization of Ag clusters which affects their properties significantly. Particularly, the formation of Ag_2O is of relevance due to its similarities with its isoelectronic analogue Cu_2O, with obvious links to high temperature superconductors [7]. The oxidation as well as the partial sulfidization of supported and embedded clusters was examined using optical spectroscopy, where one can see a shift in the plasmon energy after exposing the clean Ag clusters to air.

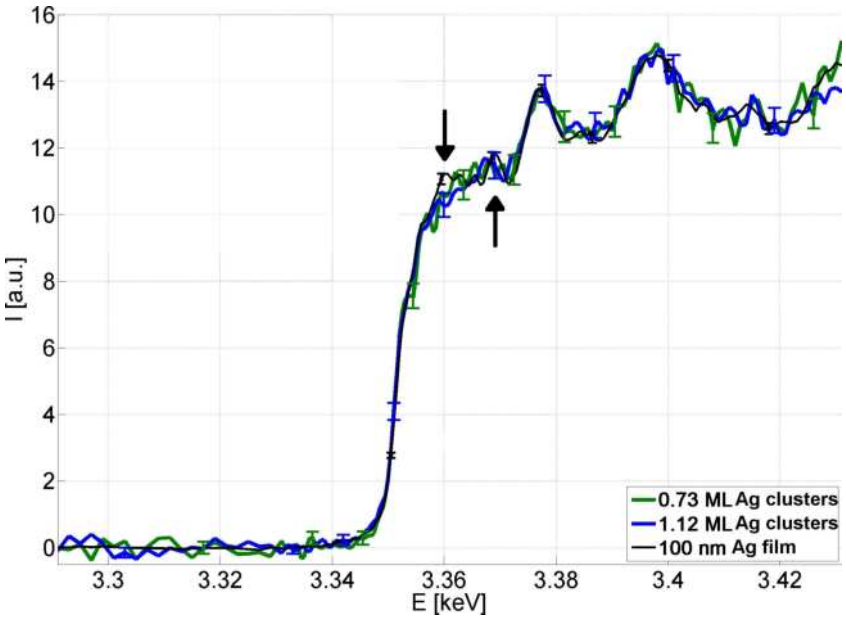

Figure 1: XANES spectra of the Ag L_3 edge of a Ag film and two different packing densities of Ag clusters in PDMS. Differences in the near edge structure indicated with arrows.

For the same cluster samples we performed XANES measurements at BL8, DELTA, using the Si(111) monochromator to investigate the L_3 absorption edge of Ag clusters in PDMS, an Ag reference film and on Ag_2O reference powder [8] . Using PDMS it is possible to deposit more clusters than on a SiO_2 substrate without risking co-

alescence of the clusters [9]. All samples were measured utilizing the vacuum sample environment available at BL8, DELTA.

Although the small amount of cluster material in the samples provided only a low signal to noise ratio there are visible changes of the XANES features at the Ag L_3 absorption edge compared to bulk silver (Figure 1, indicated with arrows). These findings encouraged us to perform further experiments on this subject. Measurements of the Ag L_2 edge of Ag clusters deposited into a PDMS matrix performed at ID26, ESRF, Grenoble, show significant differences compared to an Ag reference film (Figure 2) [10]. There is a continuous change to bulk properties for increasing cluster coverage. For higher coverage the features of the absorption edge (marked A, B, C) become more similar to the reference film signal, because clusters start to form bigger particles due to coalescence. These data verified the trend already seen for the Ag L_3 edge measured at BL8, DELTA.

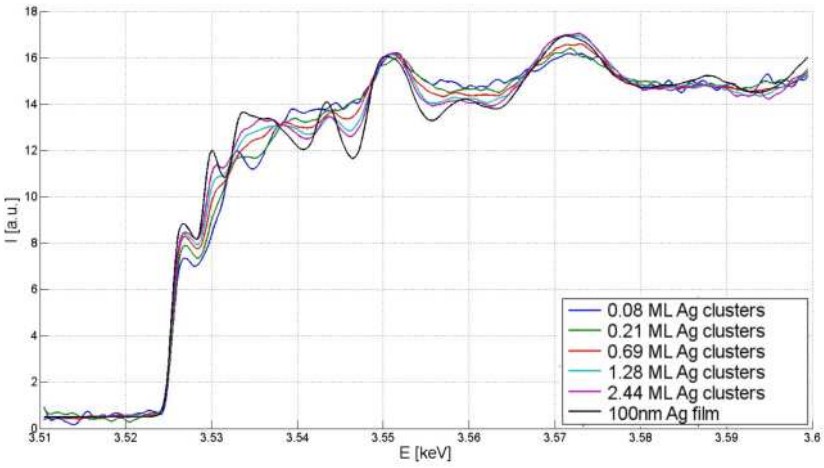

Figure 2: XANES spectra of the Ag L_2 edge of a Ag film and two different packing densities of Ag clusters in PDMS (ID26, ESRF).

In very recent measurements at BL8 (last week of October), we now investigated partly sulfidized clusters in a PDMS matrix to probe the feasibility of detecting such chemical changes in these samples. Data analysis is still in progress.

In future experiments at beamline BL8, DELTA, we would like to continue our investigations of clusters in different matrix materials. Using SiO_2 aerogel it is possible to prepare samples with a large amount of separated Ag clusters in this matrix due to its extremely low density and large network. This provides an even better signal to noise ratio.

The authors would like to acknowledge the DELTA machine group for providing synchrotron radiation and technical support.

References

[1] R.E. Palmer, S. Pratontep, and H.-G. Boyen, Nature Materials **2**, 443 (2003).

[2] Z.Y. Li, N.P. Young, M. Di Vece, S. Palomba, R.E. Palmer, A.L. Bleloch, B.C. Curley, R.L. Johnston, J. Jiang, and J. Yuan, Nature **451**, 46 (2008).

[3] S. Duffe, N. Grönhagen, L. Patryarcha, B. Sieben, C. Yin, B. von Issendorff, M. Moseler, H. Hövel, Nature Nanotechnol. **5**, 335 (2010).

[4] A.J. Haes and R.P. van Duyne, J. Am. Chem. Soc. **124**, 10596 (2002).

[5] J. Merlein, M. Kahl, A. Zuschlag, A. Sell, A. Halm, J. Boneberg, P. Leiderer, A. Leitenstorfer, and R. Bratschitsch, Nature Photonics **2**, 230, (2008).

[6] U. Kreibig, M. Gartz, A. Hilger, H. Hövel, Optical Investigations of Surfaces and Interfaces of Metal Clusters, In: Advances in Metal and Semiconductor Clusters Vol. 4, (ed. M.A. Duncan), JAI press Inc., 345 (1998).

[7] O. Sipr, F. Rocca, and G. Dalba, J. Synchrotron Rad. **6**, 770 (1999).

[8] P. Behrens, S. Aßmann, U. Bilow, C. Linke, and M. Jansen, Z. anorg. allg. Chem. **625**, 111 (1999).

[9] L. Ravagnan, G. Divitini, S. Rebasti, M. Marelli, P. Piseri and P. Milani, J. Phys. D **42**, 082002 (2009).

[10] H. Hövel, S. Hoffmann, S. Duffe, K. Latussek, D. Engemann, Ch. J. Sahle, Ch. Sternemann, ESRF user report, MA-1298, (2011).

Size controlled and Ge-oxide free Ge NC formation in multilayered $GeSiO/SiO_2$

Christoph J. Sahle*,[a], Manuel Zschintzsch*,[b], Christian Sternemann[a], Alexander Nyrow[a], Alexander Schwamberger[a], Metin Tolan[a]

[a] *Fakultät Physik/DELTA, TU Dortmund, Maria-Goeppert-Mayer-Str. 2, 44221 Dortmund, Germany.*

[b] *Institute of Ion Beam Physics and Materials Research, Helmholtz-Zentrum Dresden-Rossendorf e.V., Bautzner Landstrae 400, D-01328 Dresden, Germany.*

*email: christoph.sahle@tu-dortmund.de

The formation of size controlled Ge-oxide free Ge NCs in a silica matrix was investigated by measurements of the x–ray absorption near–edge structure (XANES) at the Ge K–edge. All measurements were performed at the materials science beamline BL8 [1] of the DELTA synchrotron radiation facility.

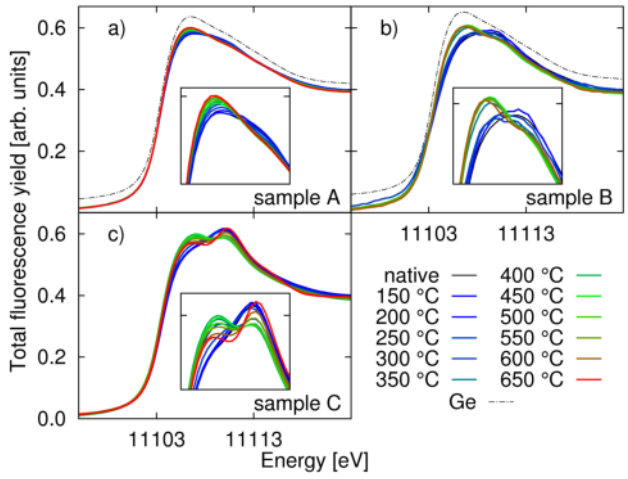

Figure 1: (a) Ge K–edge of the native and differently annealed $GeSiO/SiO_2$ multilayer samples A, B, and C.

An important aspect for the usablility of oxide matrix embedded NCs for light emitting devices or photo-voltaics are the NC's surface and/or NC-matrix interface properties. In this respect Ge NCs embedded in a Ge-oxide matrix have been proven to show an increased density of electronically active interface states which lead to a fast non-radiative exciton recombination. This phenomenon results in a considerably smaller photoluminescence yield of Ge NCs expecially when embedded in a non-stoichiometric, i.e. $x = 2$, GeO_x ($x \approx 1$) matrix. For the use in photo-voltaics a maximum exciton lifetime is desirable to allow an effcient charge separation. Following the approach reported earlier [2, 3] but instead of using dc magnetron sputtering from Ge and Si targets separately to deposit layers of GeO and SiO_2 , co-sputtering from both sputter targets was used to deposit $GeSiO_x$ layers separated by thin layers of SiO_2. Three samples of slightly different oxygen content in the GeSiO layer were deposited: sample A has a slight oxygen deficit ($x_A = 1.5$), sample B has an almost stochiometric oxygen content ($x_B = 1.9$), and sample C has a slight oxygen excess ($x_A = 2.2$). The Ge K–edges are depicted in Fig. 1. Deteils of the analysis are given in [4].

It is found that in the temperature regime where the disproportionation reaction of GeO_x takes place in the binary system [1,3] a redistribution of oxygen from Ge-oxides to the Si matrix material takes place. Depending on the stoichiometry of the SiO_x matrix different degrees of oxidization of the resulting Ge NCs can be achieved. Here, a slightly under-stoichiometric SiO_x matrix with $x < 2$ is capable of compensating oxygen contaminants in the annealing atmosphere and the possible loss of volatile GeO. Besides the study of the Ge K-edge also the Si absorption edge such as the Si K or $L_{2,3}$-edge should be investigated for a complete understanding of the processes in these ternary systems.

The authors would like to acknowledge the DELTA machine group and Ralph Wager for the beamline setup and assistence. This work was supported by, DFG (TO 169/14-1) and BMBF (05K10PEC).

References

[1] D. Lützenkirchen-Hecht, R. Wagner, U. Haake, A. Watenphul, R. Frahm, *J. Synchrotron Rad.* **16**, 264 (2009).

[2] Ch.J. Sahle, C. Sternemann, H. Conrad, A. Herdt, O.M. Feroughi, M. Tolan, A. Hohl, R. Wagner, D. Lützenkirchen–Hecht, R. Frahm, A. Sakko, and K. Hämäläinen, *Appl. Phys. Lett.* **95**, 021910 (2009).

[3] Ch.J. Sahle, M. Zschintzsch, C. Sternemann, J. von Borany, A. Mücklich, A. Nyrow, N.M. Jeutter, R. Wagner, R. Frahm, and M. Tolan, *Nanotechnology* **22**, 125709 (2011).

[4] M. Zschintzsch, Ch.J. Sahle, C. Sternemann, J. von Borany, A. Mücklich, A. Nyrow, and M. Tolan, *Nanotechnology*, in press (2011).

Influence of the chemical reaction path on the crystalline structure of sol-gel derived TiO_2 and TiO_2-ZrO_2 nanoparticles

S. J. Pfleiderer, D. Lützenkirchen-Hecht, R. Frahm

Fachbereich C-Physik, Bergische Universität Wuppertal, Gaußstr. 20, 42097 Wuppertal, Germany

In our report, we describe investigations of TiO_2 and TiO_2-ZrO_2 nanoparticles derived from sol-gel processes with XANES and XRD measurements. To influence the reaction products of the chemical reaction and following annealing process, many possibilities are known and described in literature [1-3]. The addition of small concentrations of ZrO_2 to the titania is known to stabilize the crystalline anatase phase and to prevent the particles from uncontrolled growing [3]. Next to a high degree of crystallinity and a large specific surface area, these are two desirable characteristics in photocatalysis [4,5] as well as in Li ion batteries [6]. To characterise the degree of crystallinity and the phase composition, linear combination XANES fits (LC-XANES) is used in this work. The particle size is determined from XRD measurements. As parameters to influence the reaction chemistry, the dilution of the precursor alkoxide in different amount of alcohol, the use of different electrolytes as reaction media and changes in the water to alkoxide ratio are investigated. In the case of the 1.0 M hydrochloric acid reaction solution, the effect of the amount of added acid is checked.
In our last report, we showed the XANES and XRD data from six prepared powder samples which consisted of pure TiO_2 and ZrO_2, TiO_2:ZrO_2=10:1, TiO_2:ZrO_2=2:1, TiO_2:ZrO_2=1:1 and TiO_2:ZrO_2=1:2. Only the pure oxide powders and the composite powder with TiO_2:ZrO_2=10:1 showed crystallization due to XANES and XRD data. In the next step, we studied powder samples with TiO_2:ZrO_2=4:1, 6:1 and 8:1 to see at which ratio crystallization is possible in the regarded temperature range between 350°C and 500°C. Samples with TiO_2:ZrO_2=15:1, 20:1 and 25:1 are prepared in order to search for the lowest possible concentration of zirconia which is still able to stabilize phase and size. This is necessary because it was shown in our last study that the addition of zirconia lowers the degree of crystallinity compared to pure titania powder prepared with the same reaction path [7].
We could observe that in the sample with TiO_2:ZrO_2=4:1, crystallization started at 500°C, no crystallization is observed before. With decreasing zirconia concentration, the temperature at which the crystallization start become lower and a higher degree of crystallinity can be achieved. With the investigation of the samples with lower zirconia concentrations, we found that the sample with TiO_2:ZrO_2=20:1 is a promising candidate for further investigations.
In these investigations, we can see that there is an influence of the preparation conditions on the decrease of the undesired amorphous phase, but in the most cases, no trend with the amount of added water, alcohol or the type of added electrolyte is observable.
In the investigation of the effect of the amount of added hydrochloric acid on the nanopowder, it can be seen that the pure titania powders consist of pure anatase and remaining amorphous phase in the case of an added HCl amount of 80 and 160 mmol. In the case of an added HCl amount of 320 mmol, a significant amount of rutile shows up in the XANES and XRD data which increases with increasing annealing temperature. In the TiO_2-ZrO_2 composite powders, the observed phases are only the anatase phase and remaining amorphous phase. This showed that it is possible to suppress the occurrence of other crystalline phases than anatase by the addition of zirconia. The effect that the growth of the particle size with increasing annealing temperature is suppressed by the addition of ZrO_2 has been shown in our last report [7] and can be observed in many cases in the current study.

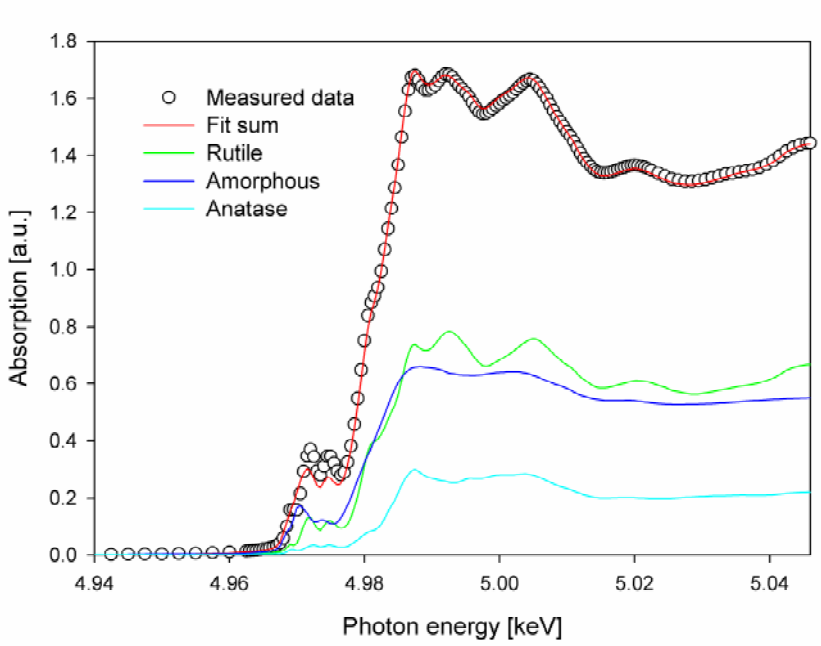

Fig. 1: The XANES spectrum of a pure TiO_2 powder synthesized with 40 mmol titanium isopropoxide and 320 mmol 1.0 M hydrochloric acid. Significant rutile concentration can be observed by comparison with the shown reference spectra. The powder was annealed at 500°C for four hours.

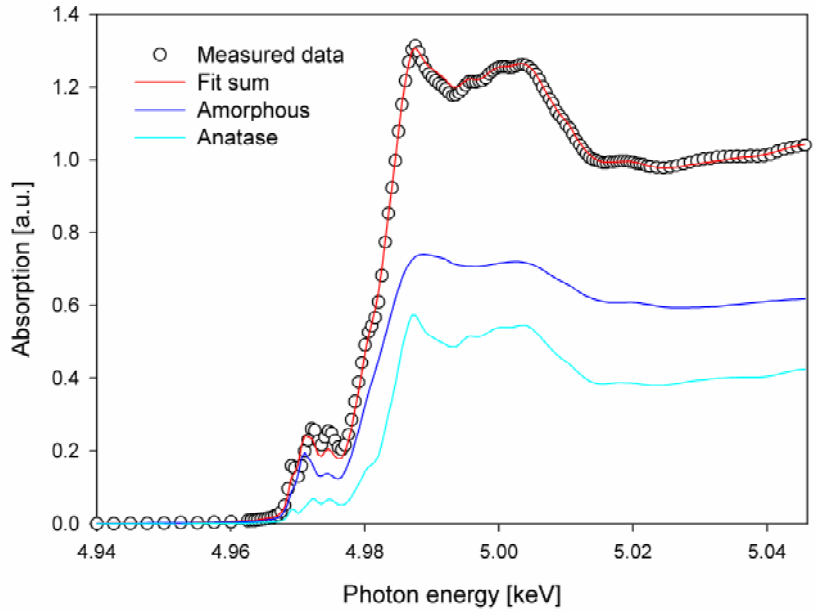

Fig. 2: The near edge spectrum of a composite sample synthesized with an overall alkoxide amount of 40 mmol and 320 mmol hydrochloric acid. The alkoxide ratio was choosen in a way that Ti:Zr=20:1. By comparison with the reference specra, it can be seen that the powder consists of anatase in a matrix of remaining amorphous phase after annealing at 500°C for four hours.

References

[1] R. Rossmanith, C. K. Weiss, J. Geserick, N. Hüsing, U. Hörmann, U. Kaiser, K. Landfester, Chem. Mater. **2008**, 20, 5768-5780.
[2] Y. Li, T. J. White, S. H. Lim, Journal of Solid State Chemistry **2004**, 177, 1372-1381.
[3] S. H. Elder, Y. Gao, X. Li, J. Liu, D. E. Mc Cready, C. F. Windisch, Jr., Chem. Mater. **1998**, 10, 3140-3145.
[4] Z. Zhang, C.-C. Wang, R. Zakaria, J. Y. Ying, J. Phys. Chem. B **1998**, 102, 10871-10878.
[5] B. Ohtani, Y. Ogawa, S. Nishimoto, J. Phys. Chem. B **1997**, 101, 3746-3752.
[6] F. Bonino, L. Busani, M. Lazzari, M. Manstretta, B. Rivotta, B. Scrosati, J. Power Sources **1981**, 6, 261-270.
[7] S. Pfleiderer, D. Lützenkirchen-Hecht, R. Frahm, submitted to Journal of Sol-Gel Science and Technology.

Characterization of the microstructure in diffusion brazed Al-Al- and Al-steel- joints

Lukas Wojarski[1], Andre Steffen[2], Christian Sternemann[2], Michael Paulus[2], Salar Alkas-Yonan[1], Metin Tolan[2], Wolfgang Tillmann[1]

[1] Lehrstuhl für Werkstofftechnologie, TU Dortmund, D-44227 Dortmund
[2] Fakultät Physik/DELTA, TU Dortmund, D-44227 Dortmund

Introduction

Despite the vast distribution of aluminium for many industrial applications due to its specific properties such as low density accompanied by excellent specific stiffness in addition with outstanding formability, joining aluminiumis are still challenging. The main obstacle for thermal joining processes is the superficial oxide film on aluminium alloys, which hinders molten material to flow in case of welding and at the same time prevents wetting processes. The reason is the comparatively high melting point of alumina as well as its tightness regarding any diffusion mechanisms. Therefore it is inevitable to remove or destroy the oxide film prior or during the brazing process. Commonly, fluxes are applied for the reduction of the surface, which lead to impurities in the brazing seam. Furthermore, fluxes can be corrosive and have to be removed from the surface, which leads to high expenses for the costly cleaning process as well as for the disposal of the chemicals [1].

A possible approach to produce aluminium joints without the utilization of fluxes is to make use of diffusion brazing processes. Diffusion brazing processes are known for producing high strength joints, which can be manufactured at moderate temperatures. Furthermore, they are commonly used to braze barely wettable materials. In contrast to diffusion welding, the TLP bonding process is based on the formation of a liquid. Thus, it features brazing specific advantages like tolerance towards manufacturing inaccuracies as well as the absence of high clamping forces, which limit the complexity of the joining partners. Furthermore, the joints provide a higher re-melting temperature compared to the actual process temperature, and feature a joint microstructure close to that of the parent material, resulting in similar mechanical properties when applying a sufficient homogenization after isothermal solidification [2].

Despite the technological advantages of TLP joints, the industrial application of the process is usually limited due to the long process times, which range up to several hours and therefore lead to high expenses. Consequently, there is the need for a deep understanding of the process kinetics during TLP brazing and their influence on the microstructure, in order to shorten costly process optimization [2].

Within these investigations copper was used as intermediate layer to join aluminium to aluminium and aluminium to steel due to the existence of an eutectic in the binary system Al-Cu with a melting point of 548°C, which is significantly lower than the melting temperature of conventional brazes like AlSi-12. The deposition of copper was carried out using an Arc-PVD coating due to the possibility to apply homogenous coatings with defined amounts [3].

Preliminary Results

Within the foregoing investigations the dependence of the predominant process parameter, the dwell time on the resulting microstructure was analyzed. The samples were brazed at 580°C for varying dwell times. After the heating cycle the microstructure of the samples were examined by means of optical microscopy. Furthermore, chemical examinations of the samples using a scanning electron microscope (SEM) that is equipped with an energy dispersive x-ray spectrometer were carried out.

These experiments revealed that at dwell times below 3 minutes no liquid phase had formed and therefore no bond could be obtained (see Fig. 1). All samples with dwell times below 3 minutes feature to continuous layer and the chemical analysis of the samples revealed the same chemical

composition independent of the applied process duration. Whereas the upper layer contains 30 at-% aluminium, the lower layer is comprised of 50 at-% aluminium.

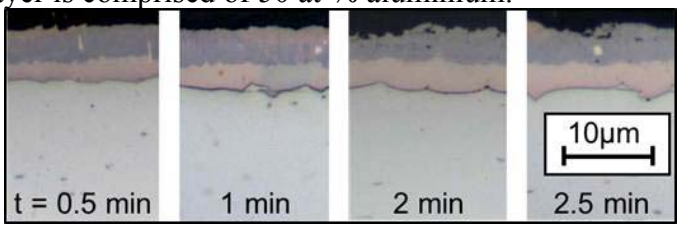

Figure 1: Microstructure of samples with dwell times shorter than 3 minutes

When the dwell time exceeds 3 minuntes, instantly a liquid phase was formed and the samples stuck together after cooling (see Fig. 2). Furthermore, the samples do not feature homogenous layers anymore, but show a eutectic structure indicating the width of the liquid phase that solidifies isothermally due to diffusion with increasing dwell time.

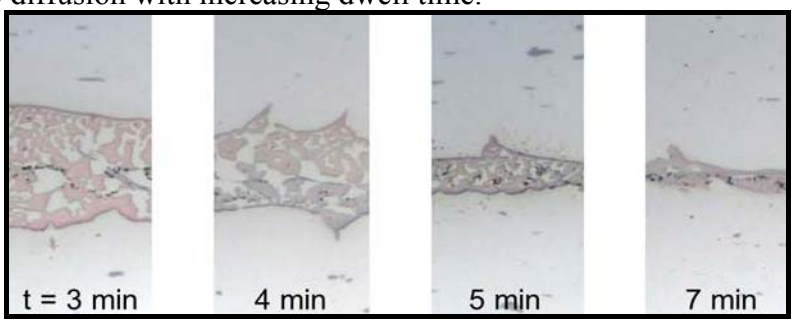

Figure 2: Microstructure of samples after formation of a liquid

These results lead to the conclusions that only two stable phases form prior to the formation of the liquid phase which do not change their composition over time, but only vary in their thickness. Due to the stoichiometric composition these phases could be AlCu and Al_4Cu_9 or $AlCu_2$, which had to be proven by means of x-ray diffraction (XRD). Furthermore, the microstructure of the bonded samples probably consists of α-aluminium and Al_2Cu, which had to be approved as well.

XRD-Results

In order to determine the actual phases formed in the interface of the brazements, XRD measurements of the fractured surfaces of shear tension samples were conducted, as it is assumed that the samples fracture at locations with local stress maxima which commonly appear in the fusion area. Due to the small thickness of the phase bands to be examined, a surface sensitiv XRD set-up was applied. The photonenergy was E = 15 keV. In figures 3 & 4 the scattering angle 2θ was rescaled to correspond to a photonenergy of Cu Kα radiation.

The conducted XRD-measurements confirmed the assumption that the layers at the unbonded samples consists of AlCu and Al_4Cu_9 for all dwell times shorter than 3 minutes as shown in Fig. 3. Furthermore, it could be shown that the other possible phase $AlCu_2$ does not form due to the advantageous conditions for the formation of Al_4Cu_9 at the elevated temperature during the brazing process. Some samples, like the one shown in Fig. 3, additionally contain some remaining pure copper. Due to diffusion mechanisms the AlCu and Al_4Cu_9 phases grow whereas the amount of pure copper decreases with increasing dwell time until the former copper layer solely consists of the two phase bands.

The micrographs obtained by light microscopy in addition with the XRD measurements of the bonded samples revealed the presence of a liquid phase during the actual brazing process due to the existence of α-aluminium and Al_2Cu (see Fig. 4), which are the phases present close to the eutectic according to the binary phase diagram in the Al-Cu-system. These phases were present in all bonded samples up to a dwell times of 100 minutes, where the seam disappeared due to completion of the homogenization stage and hence only α-aluminium was detectable.

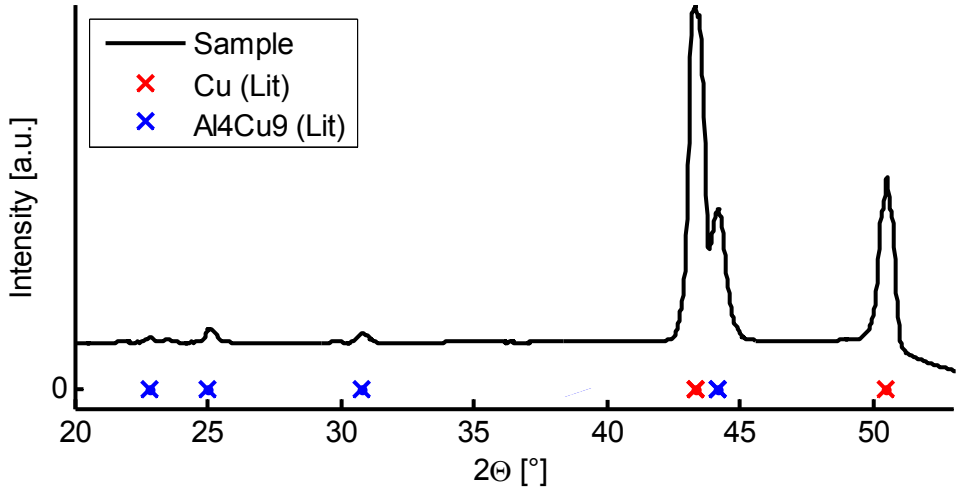

Figure 3: Exemplary XRD-pattern of an unbonded sample.

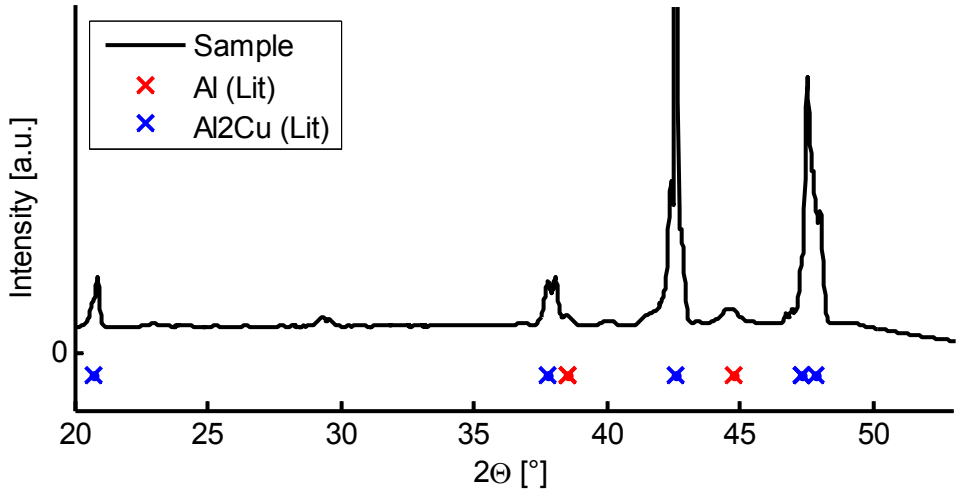

Figure 4: Exemplary XRD-pattern of a successfully bonded sample.

Conclusion

XRD measurements were used to determine the phases that occur during the brazing process. The expected phases could be proven and therefore a better understanding of the kinetics during diffusion brazing of aluminium materials using copper interlayers was reached. Based on these results further process optimization will be possible due to the correlation of the resulting shear strength in dependence of the present phases and its distribution in the joint area.

References

[1] Türpe, M.: Betrachtungen zum Löten in Gegenwart und Zukunft. Materialwissenschaft und Werkstofftechnik, 36 (2007) 2, pp. 187 – 191.

[2] Gale, W. F., Butts, D. A.: Transient liquid phasebonding. Science and Technology of Welding and Joining, 9 (2004) 4, pp. 283 – 300.

[3] Tillmann, W.; Osmanda, A.M.; Wojarski, L.: Diffusion brazing of Al-alloys for hybride structures, Quarterly Journal of the Japan Welding society, 27 (2009) 2, pp. 179-182.

X-ray diffraction studies on low alloyed and high-Mn steels with TRansformation and TWinning Induced Plasticity (TRIP, TWIP)

Hendrik Quade[1], Raphael Twardowski[1], Sascha Buttmann[1], Andre Steffen[2], Michael Paulus[2], Christian Sternemann[2], Metin Tolan[2], Ulrich Prahl[1], Wolfgang Bleck[1]

[1] Institut für Eisenhüttenkunde der RWTH-Aachen Intzestrasse 1, D-52072 Aachen
[2] Fakultät Physik/DELTA, TU Dortmund, Maria-Goeppert-Mayer-Str. 2, D-44227 Dortmund

Introduction

High manganese austenitic steels and low alloyed TRIP steels combine high strength and formability, therefore they get high attention regarding the application in automotive parts. The excellent mechanical properties of these steels result from different deformation mechanisms, such as the martensitic transformation and twinning. In addition to the knowledge of the individual hardening mechanisms the prediction of damage and failure is of major importance for processing and use in safety-sensitive areas. The precise quantification of the martensitic transformed and twinned regions is indispensable [1-3]. The TRansformation-Induced-Plasticity (TRIP) and Twinning Induced Plasticity-effect (TWIP) cause an extra work hardening during straining, by phase transformation from austenite to martensite and grain refinement due to formation of mechanical twins. The TRIP and TWIP effect does not only result in an increase in hardening but also postpones necking or damage to later deformation degrees, which leads to a better formability.

Experiments

For the investigation of the Transformation Induced Plasticity effect during straining 3 commercial low-alloyed TRIP steels were anylysed. The investigations were carried out using a tensile testing machine of the institute of forming technology and light weight construction of the TU Dortmund in order to be able to perform in-situ tests. Further we carried out investigations on high-Mn steel tensile samples with varying microstructure. The microstructure was set by annealing at temperatures in the range of 800°C to 1030°C for 30 min and quenching in water. Afterwards the samples were pre-strained to 5 %, 10 %, 20 %, 30% and 40% of true strain, in order to reveal the evolution of the phase transformation mechanisms. The tensile tests were carried out for a temperature range of 123 K to 423 K and a strain rate of 0,004 1/s.
The X-ray diffraction experiments were carried out at beamline BL9. The low-alloyed samples were measured in transmission geometry, the high-Mn steel tensile samples in reflection geometry. For the measurements, monochromatic X-rays with a wavelength of λ=0.45919 Å (27 keV) were used. For the detection of the 2D diffraction pattern (exemplify shown in Figure 1) an image plate detector (MAR345) was applied. The corresponding diffractogram can be estimated by integrating over the whole angle of the rings (Figure 1). For further quantitative analysis also the volume fractions of austenite and martensite phase were calculated.

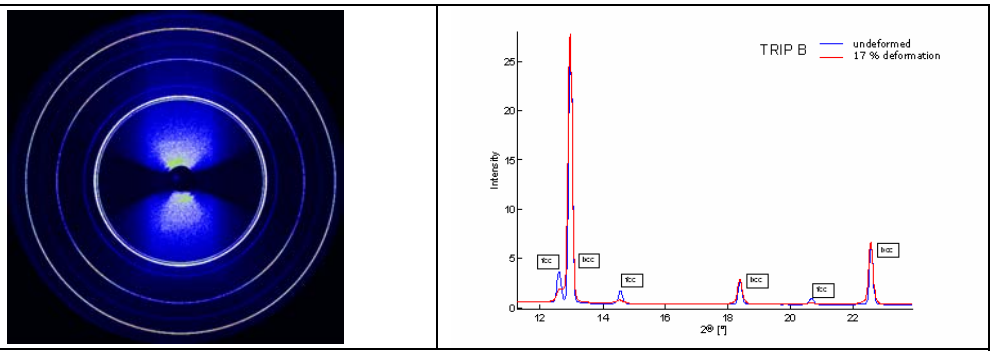

Figure 1: Generated Debye-Scherrer rings after irradiation of the sample (left), corresponding diffractogram (right).

Results and Discussion

Figure 2 shows the volume fractions of retained austenite as a function of tensile force and strain as averaged curve for 4 parallel samples in the investigated low-alloyed TRIP samples. The retained austenite stability for all steels is nearly equal. The highest volume fraction was observed in TRIP B with a lower resistance against phase transformation at higher strains.

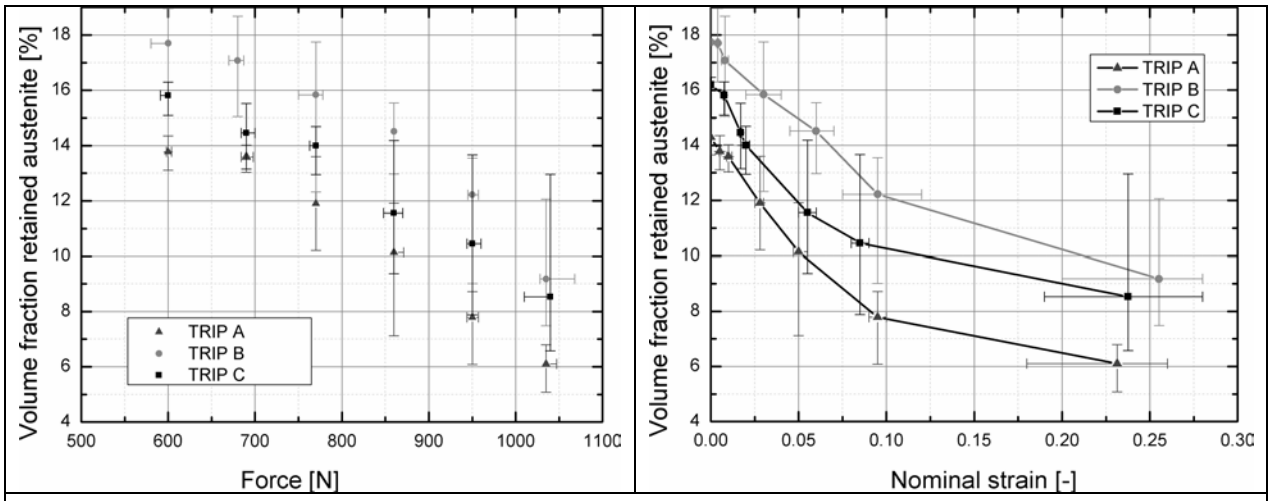

Figure 2: Volume fraction retained austenite as a function of tensile force (left) and strain (right).

For all investigated steels it can be seen a rapid martensite formation at early states of deformation. Secondary, there exists no significant sigmoidal shape in the evolution of volume fraction over strain. At higher strain values the retained austenite content converges to a saturation value.
3 regimes of transformation were observed. The elastic regime were no martensite formation was detected, a regime at lower strains were a fast phase transformation takes place and a regime at higher states of deformation were the martensite volume fraction reaches a saturation.
In figure 3 the results for the high-Mn steel tensile samples are summarized. The volume fraction of the hcp-phase is plotted as a function of true strain for each microstructure and all testing temperatures of 123 K, 293 K, 373 K and 423 K. The lowest values for the hcp-phase are found for all microstructures at the highest testing temperature of 373 K and 423 K. With decreasing temperature the volume fraction of the hcp-phase is increasing significantly only for microstructures with a grain size of 15 µm and 100 µm. The overall growth can be fitted by an exponential function.
In initial condition the tensile samples are fully austenitic. Plastic deformation takes place by mechanical twinning or ε-martensite formation, depending on the stacking fault energy. Both, the TWIP and the TRIP effect show an increase in the volume fraction of the hcp-phase. In order to distinguish between both mechanisms, additional EBSD measurements were carried out. Hence, mechanical twinning is dominant for the microstructures with a grain size of 2 µm and 5 µm and all testing temperatures and additionally for the microstructures with a grain size of 15 µm and 100 µm at 373 K and 423 K. With decreasing temperature and increasing grain size the stacking fault energy is significantly lowered and ε-martensite formation prevails. Obviously the stacking fault energy mainly controlling the active deformation mechanism and is highly dependent on the temperature and microstructure. Synchrotron investigations are suited for the detection of thin twin boundaries and therefor allow a quantitative measurement of their volume fraction.

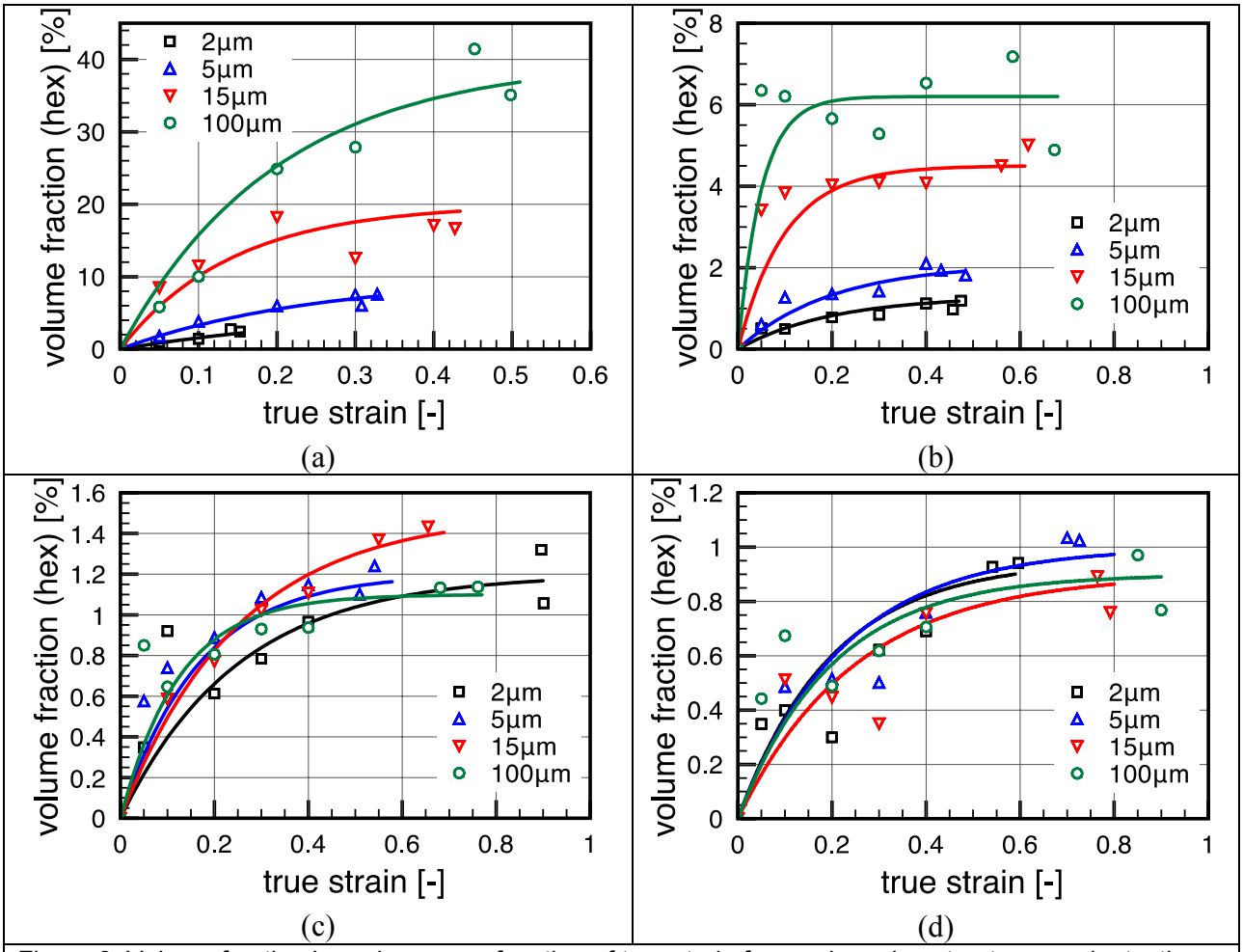

Figure 3: Volume fraction hcp-phase as a function of true strain for varying microstructures and a testing temperature of 123 K (a), 293 K (b), 373 K (c) and 423 K (d).

Acknowledgements

The authors like to acknowledge the DELTA machine group for providing synchrotron radiation and technical support.
A. Steffen thanks the NRW Forschungsschule 'Forschung mit Synchrotron-strahlung in den Nano- und Biowissenschaften' for financial support.
Hendrik Quade acknowledges the Materials innovation institute M2i (http://www.m2i.nl) for the financial support. The corresponding research was carried out under the project No. MC2.07293.
Raphael Twardowski would like to thank the Deutsche Forschungsgemeinschaft for the financial support. The current research was carried out within the SFB 761 under the project C6.

References

[1] L. Zhao, N.H. van Dijk, E. Brück, J. Sietsma, S. Van der Zwaag. Magnetic and X-ray diffraction measurements for the determination of retained austenite in TRIP steels. Materials Science and Engineering, A313, 2001, pp. 145-152.

[2] N.H. van Dijk, A.M. Butt, L. Zhao, J. Sietsma, S.E. Offerman, J.P. Wright, S. van der Zwaag. Thermal stability of retained austenite in TRIP steels studied by synchrotron X-ray diffraction during cooling. Acta Materialia 53, 2005, pp. 5439-5447.

[3] K. Yan, D. G. Carr, M. D. Callaghan, K.-D. Liss, H. Li. Deformation mechanisms of twinninginduced plasticity steels: In situ synchrotron characterization and modeling. Scripta Materialia 62, 2010, pp. 246-249

Optimization of the mechanical properties of HVOF sprayed nanostructured WC-Co coatings manufactured by fine powders (-10+2 µm) with ultra-fine carbides (400 nm)

Wolfgang Tillmann[a], Metin Tolan[b], Peter Hollingsworth[a]*, Ingor Baumann[a], Michael Paulus[b],
[a]*Institute of Materials Engineering, Technische Universität Dortmund, Leonhard-Euler-Str. 2, 44227 Dortmund, Germany*
[b]*Fakultät Physik/DELTA, Technische Universität Dortmund, Maria-Goeppert-Mayer-Str. 2, 44227 Dortmund, Germany*
*e-mail: peter.hollingsworth@udo.edu

Thermal sprayed Tungsten-Carbide-Cobalt (WC-Co) coatings are widely used to protect surfaces of tools and machine components against sliding, abrasive and erosive wear [1]. A novel application is the coating of forming tools. In addition to high wear resistance, it is particularly important to maintain the high shape and dimensional accuracy of the surface after the coating application [2]. Conventional structured WC-Co coatings, which have been widely developed by means of the High Velocity Oxy-Fuel flame spraying technique (HVOF) and also have extensively been investigated by many researchers, are not suitable, as they often feature an inadequate surface roughness as-sprayed. Another problem represents the inappropriate porosity in the microstructure > 1 % which often requires a minimum layer thickness > 100 µm to provide a sufficient wear protection. To adapt the surface properties to the demands of the forming process an expensive surface finishing (for instance by grinding) is necessary [3]. An innovative approach is the processing of fine WC-Co (< 15 µm) powders by means of HVOF in order to obtain fine structured coatings with very low porosities and smooth surfaces as-sprayed. However, the processing of fine powders is associated with difficulties [4]. Due to their high surface-to-volume ratio fine powders tend to agglomerate rapidly resulting in an uncontinuous powder flow. Another problem is represented by the high thermal susceptibility of fine powders, which can lead to undesirable phase reactions when passing through the hot HVOF jet. In order to prevent these undesirable effects and to process fine powders reliably, suitable spray equipment and optimized spray parameters are fundamentally required [5-6]. In this study, the feeding and processing of a fine WC-12Co powder (Fig. 1) with agglomerate size of 2-10 µm and 400 nm WC-phases by means of the HVOF process was investigated to manufacture fine structured wear protective coatings.

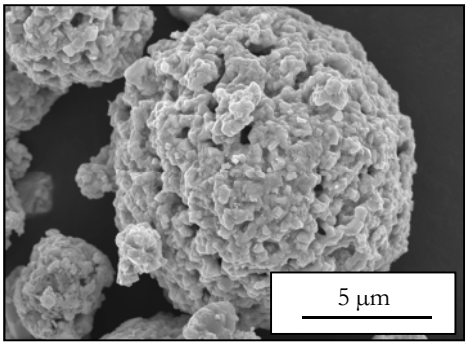

Figure 1: SEM picture oft the used WC-12 powder

Within this spray experiments the focus was placed on the mechanical and morphological properties like microhardness (h), fracture toughness (ft), porosity (p) and roughness (r). Additionally, the phase compositions of feedstock powder and coatings were determined by using x-ray diffraction experiments and correlated to the mechanical properties.

To find suitable spray parameters statistical design of experiments (DoE) was used. The DoE was devided in three parts. The goal of the first part, the pilot tests, was to identify appropriate factor levels for the spray parameters. For this purpose the kerosene flow (kf), the stand-off distance (sod) and the oxygen-fuel ratio λ were varied [7]. Afterwards, the intention of the second part, the screening, was to identify the spray parameters, which mainly influence the coating and process properties microhardness, fracture toughness, porosity, roughness and deposition efficiency. The following parameters were diversified: kerosene flow, lambda value λ, backside cooling pressure (bcp), frontside cooling pressure (fcp), carrier-gas flow (cf), powder rate (pr), gun velocity (gv) and stand-off distance. It has been shown, that the kf, lambda value λ and the sod are the most significant process parameter [7]. In the subsequent multi-criteria optimization, these three parameter were varied in order to find best possible coating characteristics even at a high deposition efficiency or at least to realize the best possible compromise. A section of the optimization results is shown in Fig. 2. For reasons of clarity (and readability) only the 2-dimensional contour plot is shown. Here one can find the optimum at a stand-off distance of 170 mm and a λ value of 1.2. Additionally a kerosene flow of 15.3 l/h could be identified. The multi-criteria optimization model predicts optimized coating properties for this parameter settings. In verification experiments the predicted coating properties were compared to the experimental results. An example of the comparison is shown in Fig.3. The red bar indicates the predicted and the green bar the experimental microhardness of the optimized coating. The predicted coating hardness agrees very well with the experimental result, what shows that the optimization was successful. In addition to the process and coating optimization the influence of the phase transformation was investigated. The phase determination is

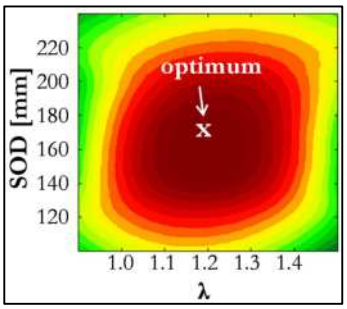

Figure 2: Result of the multicriteria optimization

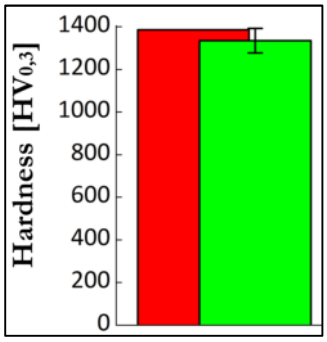

Figure 3: Comparison of the predicted and the experimental microhardness

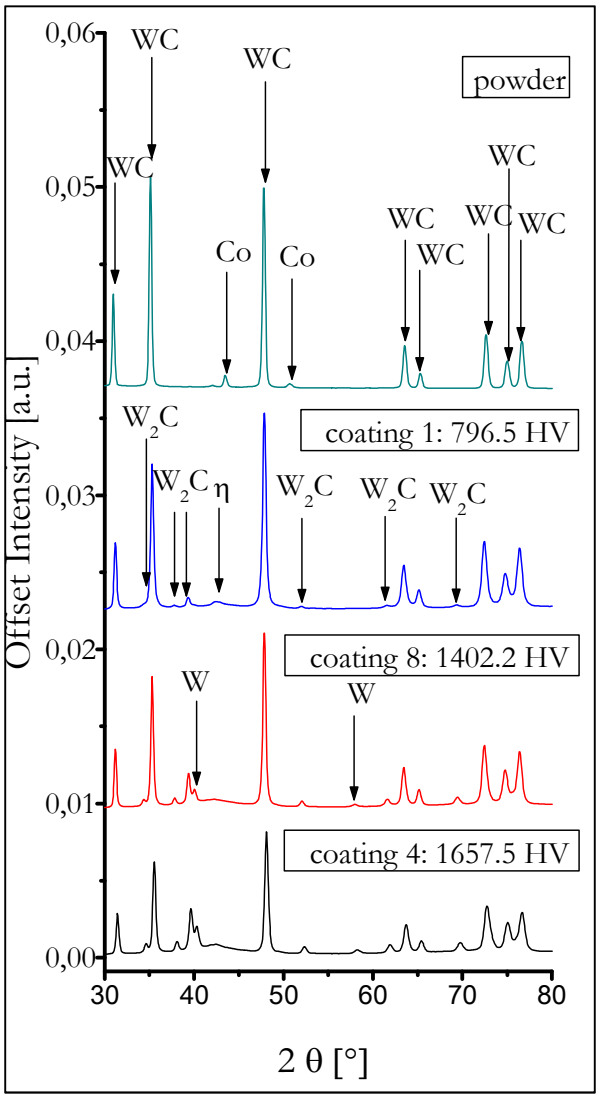

Figure 4: X-ray diffraction patterns

of particular interest, because of the small agglomerate size and consequently the thermal sensibility of the powder. The phase analyses were performed by XRD using synchrotron radiation with a photon energy of 27 keV. The spectra of the feedstock powder and three demonstrative coatings are shown in Fig. 4. As expected, the powder contains cobalt and tungsten-carbide. The three spectra of the coatings are sorted by microhardness in descending order. First of all the absence of pure crystalline Co in the HVOF sprayed coatings attracts attention. That implies that the powder agglomerates melt completely in flight. The enormous cooling rate limits the crystallisation of the Co. Furthermore the coatings include the originated phases W, W_2C and η-phases. The cause of the phase transformation is the overheating of the particle surface and consequently a dissolution of WC. Especially the small WC grain size of 400 nm intensifies the heating of the WC particles and consequently the phase transformation (particular information in [8]). The amount of W_2C, W and η-phases influences the coating properties, particularly the microhardness and the fracture toughness. The higher the amount of W_2C, W and η-phases the higher the microhardness (Fig. 4). On the one hand the surface of the WC particles is hardened by the formation of the harder W_2C, and on the other hand the formation of η-phases results in a hardening of the binder matrix. Simultaneously decreasing fracture toughness is expected, but beside the hardness the fracture toughness increases with increasing temperature (and large particle in flight velocities). Thereby the partial molten powder agglomerates conjoin more closely to the other agglomerates, which results in an highercohesive strength of the individual splats. A further increase of the temperature of the particles in-flight and accompanied by increased phase transformations causes a decreasing fracture toughness.. This leads to the conclusion that a process parameter optimization is important to adjust desired coating properties.

References

[1] Kerspe, H.: Aufgaben und Verfahren in der Oberflächentechnik, Renningen-Malmsheim, Expert Verlag (2008)

[2] Tillmann, W.; Vogli, E.; Baumann, I.; Krebs, B.; Nebel, J.: Wear-protective cermet coatings for forming tools in *Materials Science and Engineering Technology* (2010) Volume 41, Issue 7, pp. 597-607

[3] Lindemann, U.; Reichwald, R.; Zäh, M.: Individualisierte Produkte – Komplexität beherrschen in Entwicklung und Produktion, Berlin, Springer Verlag (2006)

[4] Tillmann, W.; Vogli, E.; Baumann, I.: Manufacturing of HVOF sprayed, finest structured cermet coatings using fine WC-12Co powders (– 8 + 1 µm) in *Materials Science and Engineering Technology* (2008),Volume 39, Issue 12, pp. 859-866

[5] Tillmann, W.; Vogli, E.; Baumann, I.; Matthaeus, G.; Ostrowski, T.: Influence of the HVOF Gas Composition on the Thermal Spraying of WC-Co Submicron Powders (−8 + 1 µm) to Produce Superfine Structured Cermet Coatings in *Journal of Thermal Spray Technology* (2008), Volume **17**, Issue 5-6, pp 924-932

[6] Tillmann, W.; Vogli, E.; Baumann, I.; Kopp, G.; Weihs, C.: Desirability-Based Multi-Criteria Optimization of HVOF Spray Experiments to Manufacture Fine Structured Wear-Resistant 75Cr3C2-25(NiCr20) Coatings in *Journal of Thermal Spray Technology* (2009), Volume 19, Issue 1-2, pp. 392-408

[7] Tillmann, W.; Hollingsworth, P.; Baumann, I.; Tolan M.; Paulus, M Nanostructured WC-Co coatings manufactured by fine powders (-10+2 µm) with ultra-fine carbides (400 nm) by means of HVOF in *DVS-Berichte* 276, ISBN 978-3-87155-268 (2011)

[8] Hollingsworth, P.:Einsatz statistischer Versuchsplanungsmethoden zur Entwicklung und Optimierung von thermisch gespritzten Wolframkarbid basierten Schichten und deren Analyse mittels röntgenographischer Methoden, Diploma thesis (2011), TU Dortmund

The effect of high pressure on peanuts

Martin A. Schroer*,[a], Michael Paulus[a], Metin Tolan[a]
[a] *Fakultät Physik/DELTA, TU Dortmund, Maria-Goeppert-Mayer-Str. 2, D-44227 Dortmund, Germany*
*email: martin.schroer@tu-dortmund.de

The application of high hydrostatic pressure has become a versatile method to induce different types of structural transitions of various large biological macromolecules. For instance in combination with scattering techniques, the unfolding of proteins and its dependence on molecular details can be studied [1, 2] as well as the influence of pressure on the protein-protein interaction in concentrated solutions [3, 4]. Similarly, the phase diagram of model membran systems as present in organisms especially in the deep sea can be explored using high pressures [5]. Moreover, besides its physicochemical and physiological relevance, high pressure is also of biotechnological interest as for instance in high pressure food processing [6].

In this spirit a study of the effect of high pressure on the nanostructure of a peanut has been performed. Employing small angle X-ray scattering (SAXS) allowed to reveal structural changes on the mesoscopic length scale that is characteristic for membranes and proteins. SAXS measurements under pressures of up to 4 kbar were conducted at beamline BL9 using a custom-built high pressure sample cell [7, 8].

The peanut sample was taken from a commercially available candy bar (Snickers, Mars Inc.) and rinsed with water to remove parasitic caramel deposits. From the so cleaned peanut, a slice was taken and placed into the sample cell.

The so-obtained SAXS curves are shown in Fig. 1 for different pressures. Pressurizing the slice of peanut to 4 kbar results in the presence of the two peaks at $q \approx 1.0$ nm^{-1} and $q \approx 2.1$ nm^{-1}. Decreasing the pressure to 2 kbar leads to both a shift of these peaks to smaller q values as well as a reduction of their scattering intensity. After the pressure was released, a scattering curve similar to that before pressurizing the peanut is obtained. In addition, the slice did not show any sigificant change of its macroscopic structure monitored by the bare eye.

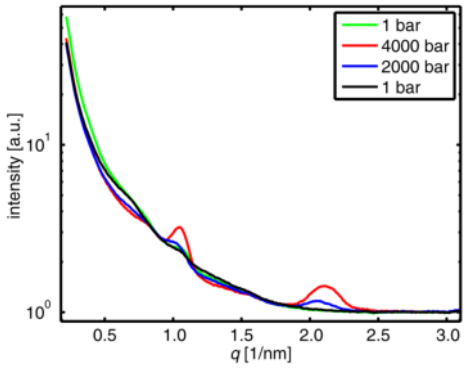

Figure 1: SAXS curves of a slice of peanut for different pressures.

Such types of structural changes have been previously reported for small angle scattering on different types of lipid systems under high temperature and pressure [5]. Thus, we attribute these findings to the composition of different lipids contained in the peanut and their pressure suceptibility.

Thus, this short study showed impressively a fully reversible pressure-induced transition in a peanut.

The authors like to acknowledge the DELTA machine group for providing synchrotron radiation, technical support and sample supply. The authors are not aware of any affiliations, memberships, funding, or financial holdings that might be perceived as affecting the objectivity of this review.

References

[1] G. Panick, R. Malessa, R. Winter,G. Rapp, K.J. Frye, C.A. Royer. *J. Mol. Biol.* **275**, 389 (1998).

[2] M.A. Schroer, M. Paulus, C. Jeworrek, C. Krywka, S. Schmacke, Y. Zhai, D.C.F. Wieland, Ch.J. Sahle, M. Chimenti, C.A. Royer, B. Garcia-Moreno, M. Tolan, R. Winter. *Biophys. J.* **99**, 3430 (2010).

[3] M.A. Schroer, J. Markgraf, D.C.F. Wieland, Ch.J. Sahle, J. Möller, M. Paulus, M. Tolan, R. Winter. *Phys. Rev. Lett.* **106**, 178102 (2011).

[4] M.A. Schroer, Y. Zhai., D.C.F. Wieland, Ch.J. Sahle, J. Nase, M. Paulus, M. Tolan, R. Winter. *Ang. Chem. Int. Ed.*, accepted for publication (2011).

[5] R. Winter, C. Jeworrek. *Soft Matter* **5**, 3157 (2009).

[6] M.F. San Martin, G.V. Barbosa-Canovas, B.G. Swanson. *Crit. Rev. Food. Sci. Nutr.* **42**, 627 (2002).

[7] C. Krywka, C. Sternemann, M. Paulus, N. Javid, R. Winter, A. Al-Sawalmih, S.B. Yi, D. Raabe, M. Tolan, *J. Synchrotron Rad.* **14**, 244 (2007).

[8] C. Krywka, C. Sternemann. M. Paulus, M. Tolan, C. Royer, R. Winter, *ChemPhysChem* **9**, 2809 (2008).

Investigation the effect of iron incorporation during Kr^+ ion beam sputtering on Si (001) by using X-ray absorption near edge spectroscopy (XANES)

B. Khanbabaee[1], B. Arezki[1], A. Biermanns[1], M. Cornejo[2], D. Hirsch[2], F. Frost[2], U. Pietsch[1] D. Lützenkirchen-Hecht[3], and R. Wagner[3]

[1] Solid State Physics, Siegen University, 57068 Siegen, Germany

[2] Leibniz-Institut für Oberflächenmodifizierung e. V. (IOM), Permoserstraße 15, 04318 Leipzig, Germany

[3] Fachbereich C Physik, Bergische Universität Wuppertal, GaußStr. 20,42097 Wuppertal

Ion beam sputtering or ion beam erosion of surfaces can modify the surface and create a diversity of surface topographies. Recently is has been shown that pattern formation appears only if metal impurities like Fe or Cr are present on the surface. These finding prove the importance of co-deposited metals for pattern formation on Si surfaces [1-4].

We investigate the influence of iron incorporation while 2 keV Kr^+ ion beam erosion of Si surfaces under near normal ion incidence (15°) with two different doses of iron atoms. Considering the low penetration depth of ions we have used X-ray absorption near edge spectroscopy (XANES) under grazing-incidence in order to determine the depth profile and phase composition of incorporated iron atoms straight below the surface.

The XANES spectra of sample 1-A with ripple like surface and for sample 2-A with smooth surface is presented in Fig.1 (a-b), respectively, taken in vicinity of the Fe-K edge at Fe (7112 eV) under grazing incidence angle of X-ray varying from 0.1° to 0.35°. All spectra show nearly uniform shape except for sample 1-A in the region $\alpha_i << \theta_c$ (critical angle of Si) which shows a shift toward lower photon energies. The measured XANES spectra are compared with XANES standard spectra taken for various silicide compounds such as $FeSi_2$ and Fe_3Si [Fig. 4(c)]. It can be shown that the measured spectra refer to Si-rich silicide ($FeSi_2$) whereas the spectrum of sample 1-A taken at $\alpha_i << \theta_c$ is closer to a Fe-rich silicide (Fe_3Si). This means that Fe-rich silicide can be found on top of the ripples of sample 1-A only whereas Si-rich silicides can be found in deeper region and always in the non patterend sample. In other words pattern formation leads to enhancement of iron concentration in the subsurface area.

However, no of the measured spectra did match with one of the standards spectra. For further analysis it is supposed that the samples consist of a mixture of several of these compounds. The XANES data therefore were fitted by a linear combination of different standard phases. The fitting result is presented in Fig.1 (d) for sample 1-A. For all incidence angles the contribution of the $FeSi_2$ phase dominates. In addition we find a content of 25% of Fe_3Si in the subsurface region of sample 1-A but only 12% in sample 2-A (not shown). In sample 1-A the concentration of the iron rich phase decreases drastically for increasing the depth. Subsequently the Si rich phase dominates in bulk. This variation is not so obvious for sample 2-A due to the fact that the spectra do not vary as much changing the incidence angle. The fitting result verify that the XANES spectra of sample 2-A are dominated by $FeSi_2$ and the Fe_3Si is only a minority phase (9 % in α_i=0.22°).

Since the only difference of sputtering parameters between sample 1-A and 2-A is the concentration of metal atoms, pattern formation might be related to different iron concentrations on top of the surface which may induce inhomogeneous sputtering yield along the surface.

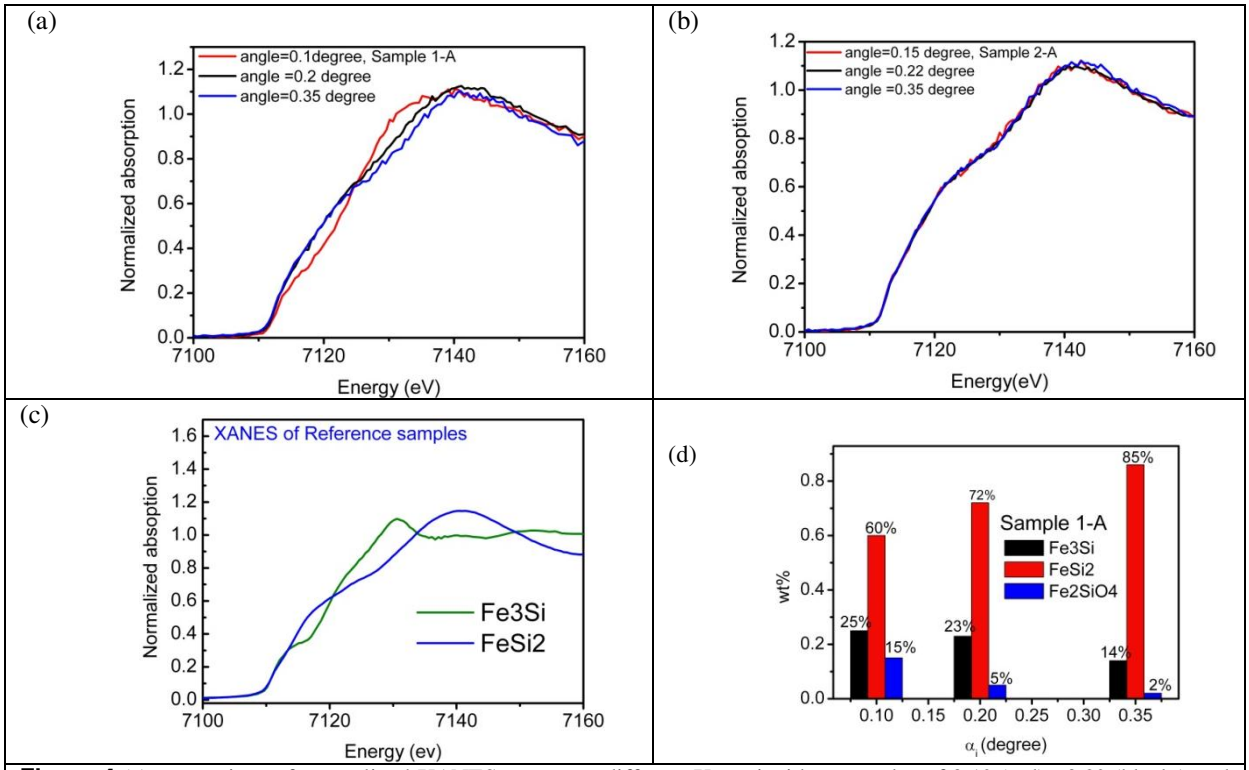

Figure 4 (a) comparison of normalized XANES spectra at different X-ray incidence angles of 0.1° (red) , 0.2° (black) and 0.35° (blue) for samples 1-A at Fe K edge. (b) incidence angles of 0.15° (red) , 0.22° (black), 0.35°(blue), for samples 2-A. (c) Comparison of the normalized XANES spectra at Fe K edge of known reference powder samples.

References :

[1] M. Cornejo, B. Ziberi, Ch. Meinecke, D. Hirsch, J. W. Gerlach, T. Höche, F. Frost, and B. Rauschenbach, Appl. Phys. A **102**, 593 (2011).

[2] F. Frost, R. Fechner, B. Ziberi, J. Völlner, D. Flamm, and A.Schindler, J. Phys.: Condens. Matter **21**,224026 (2009).

[3] S. Macko, F. Frost, B. Ziberi. D. F. Förster, and T. Michely, Nanotechnology **21**, 085301 (2010).

[4] D. Carbone, A. Biermanns, B. Ziberi, F. Frost, O. Plantevin, U. Pietsch. and T. H. Metzger, J. Phys.: Condens. Matter **21**, 224007 (2009).

Electronic structure study of the ferrospinel $NiFe_2O_4$

Martina Müller[1], Christian Caspers[1], Stephan Kramer-Sinzinger[1], Sven Döring[2,3], Ulf Berges[2,3], Claus M. Schneider[1], and Carsten Westphal[2,3]

[1]Peter Grünberg Institut (PGI-6), Forschungszentrum Jülich, D-52425 Jülich

[2]Experimentelle Physik 1, Technische Universität Dortmund, D-44221 Dortmund

[3]DELTA, Technische Universität Dortmund, D-44227 Dortmund

The ferrospinel $NiFe_2O_4$ is an insulating magnetic oxide with high magnetic ordering temperature and large saturation magnetization. This rare combination makes it very attractive for application as magnetic building blocks in spintronics devices, i. e. as spin filter tunnel contacts to semiconductors [1] or in artificial multiferroic heterostructures [2].
For such spintronics applications, the ferrimagnetic spinel $NiFe_2O_4$ has to be grown in form of high quality thin films and on heteroepitaxial substrates. However, the electronic and magnetic properties of thin films can strongly depend on the substrate material, film thickness and eventually differ significantly from the corresponding bulk materials (see Fig. 1). In order to efficiently optimize such epitaxial $NiFe_2O_4$ thin film heterostructures, it is important to clarify in detail their electronic properties. Photoemission spectroscopy based on the use of soft- x-rays can provide valuable insights in this respect by allowing to element-specifically probe the chemical state of the valence bands and core levels.

In our study, we investigated nickel ferrite $NiFe_2O_4$ films of $d_{NFO} = 20\,nm$ thickness, which were synthesized on $SrTiO_3$ substrates ($a_{NFO}/a_{STO} = -6.4\%$) by means of pulsed laser deposition from a stoichiometric target. A KrF laser with an energy of 72 mJ and a repetition rate of 7 Hz was used, while the substrate was kept at 700°C at an oxygen backpressure $p_{O_2} = 6 \times 10^{-6}\,mbar$. The chemical analysis of the $NiFe_2O_4$ thin films by soft X-ray photoemission spectroscopy (XPS) was conducted at BL 9 (DELTA).

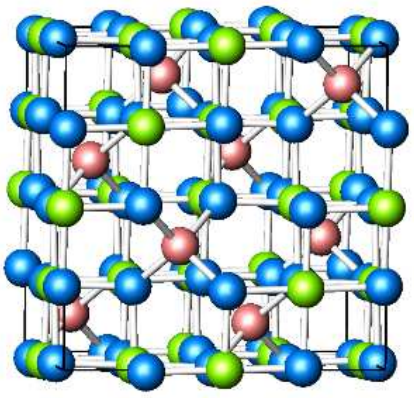

Figure 1: *$NiFe_2O_4$ crystallizes in an inverse spinel structure.*

The electronic structure study of $NiFe_2O_4$ involved mainly the Fe $2p$, $3p$ and Ni $2p$, $3p$ peaks, because their shape intimately depends on the oxidation state of these atoms. In particular, the peak separation and satellite structure are useful in characterizing the chemical environment of tetrahedrally and octahedrally bond cations in the inverse spinel crystal structure (Fig.1). In $NiFe_2O_4$, the divalent Ni_2^+ cations occupy octahedral lattice sites, whereas trivalent Fe_3^+ cations are distributed at both octahedral and tetrahedral sites.

The Fe $2p$ peak, for instance, is always split into its spin-orbit components Fe $2p_{1/2}$ and Fe $2p_{3/2}$ (Fig. 2). In the oxidized state, an additional satellite peak appears in between the Fe $2p_{1/2}$ and Fe $2p_{3/2}$ components as follows: For FeO (purely Fe^{2+}) this peak is situated 4.5 eV above the Fe $2p_{3/2}$ component, while in the case of Fe_2O_3 the satellite appears at about 8 eV above the Fe $2p_{3/2}$ component. In the particular case of Fe_3O_4, the presence of both Fe^{2+} and Fe^{3+} in a 1:1 ratio leads to the equal presence of both satellites and thus an unresolved structure between the two $2p$ spin-orbit components [3].

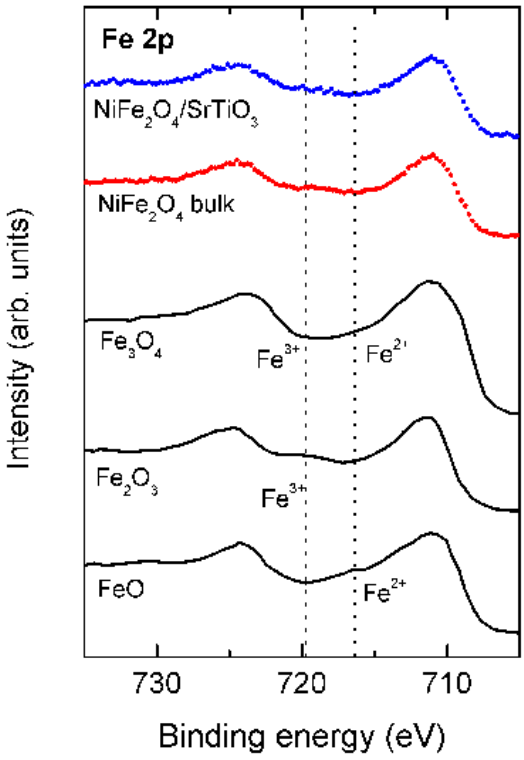

Figure 2: *Reference XPS spectra for the Fe 2p peaks in the different oxidation states of the Fe ions (taken from [3]), compared to the Fe 2p spectra of a $NiFe_2O_4$ bulk and thin films sample.*

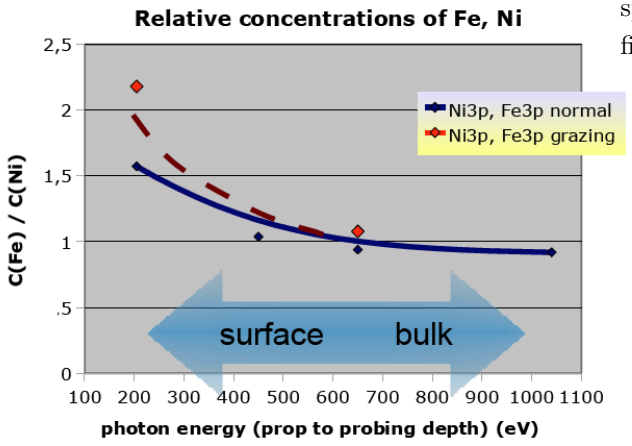

Figure 3: *Relative concentration vs. photon energy of Fe and Ni cations, extracted from the spectral intensity of the Fe, Ni 3p multiplet structures.*

Since the Fe cations in the inverse spinel structure are expected to be of trivalent valence, Fe^{3+}, one anticipates to observe a Fe $2p$ peak identical to that of Fe_2O_3. Fig. 2 contains the reference peaks of the three possible combinations of Fe oxidation states. The observation of a satellite peak and absence of a resolved satellite structure is therefore characteristic of a trivalent Fe^{3+} chemical state in stoichiometric $NiFe_2O_4$, as is observable in Figure 2. Furthermore, the Fe $2p$ spectrum of bulk $NiFe_2O_4$ is comparable to that of a $NiFe_2O_4$ thin film, however, the characteristic satellite structures are less pronounced.

The complete XPS study of the $NiFe_2O_4$ thin films confirms the proper oxidation state of the Ni and Fe atoms. Regarding the relative concentration of Fe and Ni cations, we investigate the spectral intensity of the Fe and Ni $3p$ multiplet structures. A significant decrease in information depth was achieved by (a) varying the photon energy from 1000 eV to 200 eV and (b) rotating the sample around into grazing emission geometry. The result of this depth-dependent analysis is summarized. One can clearly identify an increase in Fe cation concentration with decreasing information depth, which indicates an accumulation of iron cations in the near surface regime. validating the specific growth conditions used to elaborate the films.

[1] M. Müller, M. Luysberg, and C. M. Schneider, Appl. Phys. Lett. **98**, 142503 (2011).

[2] H. Zheng *et al.*, Science **303**,661 (2004).

[3] A. M. Bataille *et al.*, Appl. Phys. Lett. **86**, 012509 (2005).

The X-ray investigation of doping influence on InAs wire by selective area MOVPE growth

A. Davydok[a], A. Biermanns[a], K.Sladek[b] , S.Abbasi[a] and U. Pietsch[a]

[a]*Festkörperphysik, Universität Siegen, Walter-Flex-Str. 3,57072, Siegen, Germany*
[b]*Institut für Bio- und Nanosysteme (IBN-1), Jülich Aachen Research Alliance (JARA,)Forschungszentrum Jülich, 52425 Jülich, Germany*

III-V nanowires (NW) demonstrate superior electrical and optical properties what is very promising for manufacturing numbers of devices. Nowadays growth of NWs is typically realized using vapor-liquid-solid (VLS) mode MBE onto [111] planes of a zinc-blende or diamond type semiconductor by solution from a molten eutectic alloy formed by metallic seed or catalyst-free mode. Post-synthesis doping can provide additional flexibility in device design, doping control and selectivity for more sophisticated device structures [1]. Moreover using doping during growth process aspect ratio can be controlled. But influence on crystal structure of NW's is not so clear. Also crucial point for NWs formation is substrate preparation prior to growth process.

In previous experiments we investigated the self-assisted InAs NW's grown on GaAs (111)B substrates, Si doped at the level of 10^{17}~ $5x10^{18}$ cm^{-3} (n-type), covered with a thin layer of Hydrogen Silsesquioxan (HSQ). The HSQ is etched in very diluted HF to ~ 6nm thickness. SEM images show the HSQ is wavy and in some parts is damaged. Our previous experiment has shown a certain dependence of phase formation on the level of doping. In a case of doped sample we observed an additional peak appearing qz=18.33nm^{-1} indicating alloy formation. With increasing doping level this peak is shifting towards higher qz (Fig.1a). The InAs peak is found at qz=18.16nm^{-1}.

In the reported experiment we concentrated on samples where the HSQ stayed unetched. In contrast to the previous series we did not observe alloy formation (see Fig.1b and 1c). Therefore the alloy formation of the first samples series is explained by surface diffusion of Gallium liberated through small holes created during the etching process.

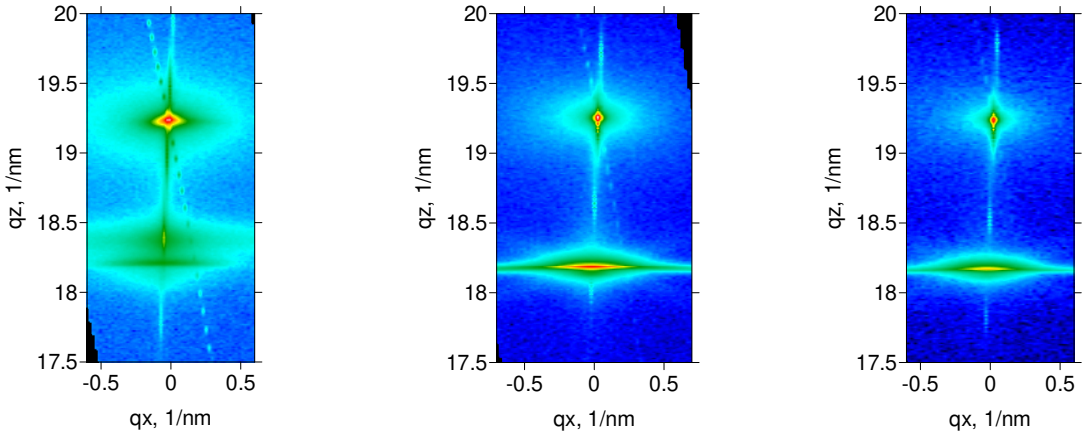

Fig. 1 RSM measured at GaAs(111) reflection from samples: a)etched, doping level $1x10^{18}$; b) unetched, undoped; c) uneched, doping level $8x10^{19}$.

In future we are planning to extend this investigation. In-plane component of such nanostructure have not been characterized yet. It is can be done at BL9 with Huber six-circle diffractometer which dedicated to GID[2].

References

[1 K. Byon, J. Fischer, K. Adu, P. Eklund Mater. Res. Soc., 832, 2005
[2] C. Krywka *et al* J. Synchrotron Rad. (2006). 13, 8-13

Current Induced Structural Changes of Thin Film OFET Devices

L. Grodd, A. Davydok, S. Grigorian, U. Pietsch
Solid-State Physics, University of Siegen, Germany

Date of experiment: 04.10.2010 – 08.10.2010
Beamline: BL 9, DELTA
Beamline scientists: Christian Sternemann, Michael Paulus

Conjugated polymers are of great interest for electronic applications, such as organic thin film field effect transistors (OFETs). Due to its semi-conducting properties, poly(3-hexylthiophene) (P3HT) is a promising candidate for organic electronics. However, the correlation of electric and structural properties is essential for the understanding of charge transfer processes within the polymer conducting channel.

At beamline BL9, DELTA, in situ studies of P3HT OFETs under applied electric field were done using grazing incidence x-ray diffraction (GIXD) technique. The (100) reflection, which corresponds to the alkyl chain-stacking, of a drop cast P3HT film was monitored at different source/drain (top contact) voltages varying between 0 V and 100 V. A channel length of 2 mm ensured that the whole conducting area of polymer was illuminated by the synchrotron beam. The source/drain current was recorded simultaneously to the structural x-ray studies.

The structural measurements revealed a reversible peak shift to smaller q_z values with increasing of the current (see Figures 1 and 2) corresponding to an expansion of (100) d-spacing of about 1.2%. The intensity remained unchanged under electric field whereas previous in situ studies of P3HT films at elevated temperatures (up to 100 °C) have shown a strong intensity decrease besides the peak shift [1].

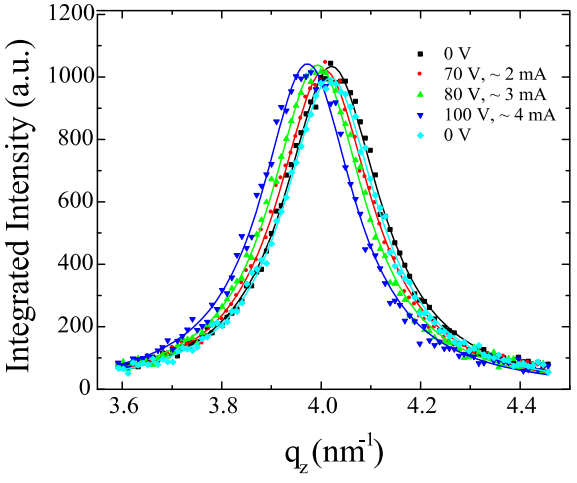

Figure 1: (100) peak position and intensity at different voltages/currents

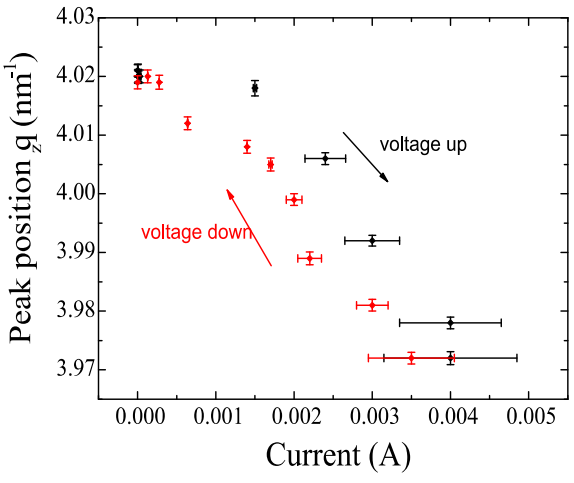

Figure 2: Reversible change in (100) peak position as function of induced current

Ongoing studies deal with the investigation of current induced changes during the solidification process of thin P3HT films. In first in_situ experiments at BL9, P3HT/chloroform solution was dropped onto source/drain channels to of silicon substrates with oxide layer at fixed source/drain voltages. Time resolved studies of the formation and the structural growth were performed by monitoring of the (100) reflection (see Figure 3) and simultaneous measurements of the current induced in the conductive channel.. During the liquid phase the reflected intensity is low (minima in intensity curve) but increases when getting solid. The final intensity level of the (100) reflection increases with the amount of deposited material. Interestingly, source/drain current (not shown here) rises after droplet deposition and peaks straight before the structural intensity has reached its maximum.

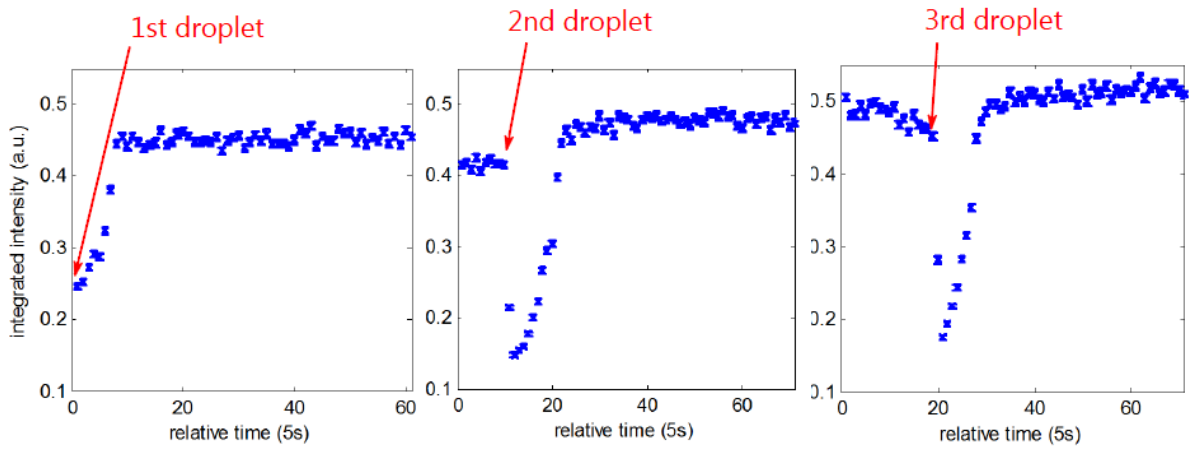

Figure 3: Out of plane (100) integrated peak intensity during film formation as a function of time. Applied source/drain potential is 10 V, counting time 5s per point. After the film was dry more droplets of P3HT were deposited on top of the existing film

References

[1] S. Joshi et al., Macromolecules 2008, 41, 6800-6808

Influence of Alkyl Side Chains on the Formation of RT and -30°C Cast P3AT crystallites

Thankaraj Salammal Shabi, [†] ***Souren Grigorian,*** [†] ***Martin Brinkmann,*** [‡] ***Ullrich Pietsch,*** [†] ***Navaphun Kayunkid,*** [‡] ***Nils Koenen*** [•] ***Ullrich Scherf*** [•]

[†] *Solid State Physics, University of Siegen, Walter Flex Strasse-3, D-57068, Siegen, Germany.*

[‡] *Institute Charles Sadron, CNRS-University of Strasbourg, 23 rue du loess, 67034 Strasbourg, France.*

[•] *Macromolecular Chemistry, University of Wuppertal, D-42097, Gauss-Str.20, Wuppertal, Germany.*

In the growing organic electronics, poly(3-alkylthiophene)s (P3ATs) has been found to be the working host materials for the fabrication of solar cells and organic field effect transistors (OFETs) etc.[1] The anisotropy in electrical conductivity of such a P3AT polymers is need of edge-on oriented crystallites for the fabrication of high throughput OFETs and solar cells.[1-3] There are a lot of strategies like molecular weight and regioregularity (rr) of the polymers have been addressed but the influence of alkyl side chain length on the in-plane stacking of the P3AT crystallites are not well known. The influence of alkyl side chain length on the formation of P3AT crystallites were studied using the following poly(3-pentylthiophene) (P3PT), poly(3-hexylthiophene) (P3HT), poly(3-heptylthiophene) (P3HeptT), and poly(3-octylthiophene) (P3OT) polymers. The grazing incidence X-ray diffraction and specular, rocking scan analysis performed for the RT and -30°C cast P3AT polymers shows that the proper selection of concentration, growth temperature and uniform casting place can helps to produce highly crystalline, very thin, and uniform films on the substrates. The 2D X-ray diffraction patterns of RT and -30°C cast P3AT polymers measured at BL9, DELTA,

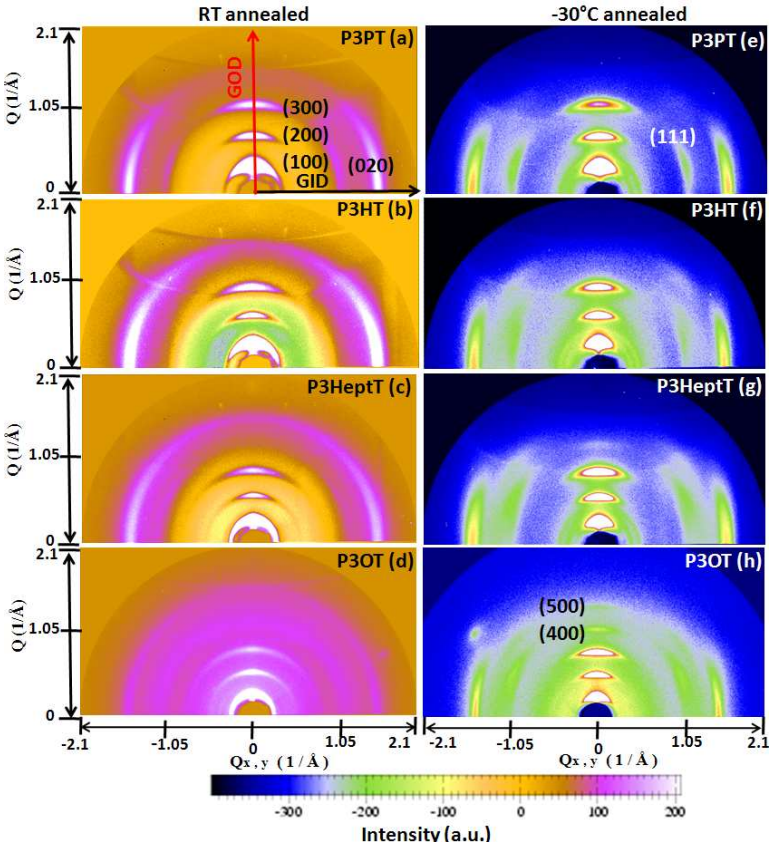

Figure 1: 2D X-ray diffraction pattern of RT (left column) and -30°C (right column) cast annealed films

Dortmund are shown in Figure 1. The -30°C cast film composed of only edge-on oriented crystallites where the RT cast film contains both the mixtures of edge- and face-on oriented crystallites. The reduction in casting temperature of the P3HT solution has two important effects: i) slowing down the evaporation rate of $CHCl_3$ i.e. the kinetics of P3HT aggregation and ii) lowering the P3HT concentration at super-saturation. At RT, the fast evaporation of $CHCl_3$ leads to kinetically trapped morphologies far from equilibrium with reduced domain sizes. Instead, at -30°C, solvent evaporation is slow and hence the aggregation occurs on a longer time scale that allows polymer chains to find the thermodynamically most stable position in an aggregate and also to adopt the most favorable orientation of the domains with respect to the substrate. The visibility of (h11) asymmetric and (020) reflections concludes the formation of highly in-plane stacked crystallites while casting at -30°C. It starts to fade as the side chain length increases because of the increase in steric hindrance between the alkyl side chains which can stimulate torsion on the thiophene backbones.[4, 5] Eventually it reduces the OFET performances as well as the photoluminescence emission of the P3AT polymers. The mobility of the -30°C cast OFET has increased by one order of magnitude as compared to the RT cast one. The overall results suggest that the highly crystalline, edge-on oriented crystallites can be prepared by reducing the casting temperature as well as the alkyl side chain length.

References

1. So, F., *Organic electronics: materials, processing, devices and applications*. 2009: CRC.
2. Kline, R.J., et al., *Dependence of regioregular poly (3-hexylthiophene) film morphology and field-effect mobility on molecular weight.* Macromolecules, 2005. **38**(8): p. 3312-3319.
3. Sirringhaus, H., et al., *Two-dimensional charge transport in self-organized, high-mobility conjugated polymers.* Nature, 1999. **401**(6754): p. 685-688.
4. Roncali, J., *Conjugated poly (thiophenes): synthesis, functionalization, and applications.* Chemical Reviews, 1992. **92**(4): p. 711-738.
5. Xie, H., et al., *The thermochromism of poly (3-alkylthiophene) s: the role of the side chains.* Synthetic Metals, 2001. **122**(2): p. 287-296.

XANES and EXAFS studies on diamond metal composites

Andre Steffen[1], Michael Paulus[1], Manuel Ferreira[2], Wolfgang Tillmann[2], Metin Tolan[1]

[1] Fakultät Physik/DELTA, TU Dortmund, D-44227 Dortmund
[2] Lehrstuhl für Werkstofftechnologie, TU Dortmund, D-44227 Dortmund

Introduction

Diamond grinding tools have widely established its usage in machining and cutting of natural stone and concrete [1,2]. Due to the fact that the performance of these tools depends on their structural properties, especially the bonding between the metal matrix and the diamond grains [2,3], x-ray spectroscopy experiments (EXAFS, XANES) promise to be a powerfull tool to investigate diamond grinding tools. XRD studies on cobalt and cobalt diamond composites, performed in 2008, 2009 and 2010 at BL9 at DELTA, did not shown any presence of cobalt carbide but a significant quantity of graphite in the interface area [4]. This is due to the graphitization of the diamond during the sintering process and leads only to a mechanical bonding of the diamond grains. Furthermore the phase transformation of cobalt could be investigated in situ during heating and cooling. To tie in with these measurements and results and to understand the sintering process more detailed our studies have been extended by the method of x-ray spectroscopy (XANES & EXAFS).

Experiment

At beamline BL8 at DELTA a big amout of metal diamond composites and pure metal references could be measured. The samples were measured at the Ti, Cr, Co and Fe K-edges. In Table 1 all samples and the performed measurements are listed.

	XANES			EXAFS			
Samples	Ti	Cr	Co	Fe	Co	Fe	(K edges)
Co-Dia I			x		x		
Co-Dia II			x				
CoCrDia		x	x		x		
Co references		x					
FeCuDia				x		x	
FeCrCuDia		x		x			
Fe references			x				
CrDia I	x						
Cr carbides		x					
Cr references	x						
Ti carbides	x						

Table 1: List of all samples and measurements.

In Figure 1 the spectra at the Co K-edge of the Co and CoCr diamond composites and their reference pure Co and cobalt oxide samples are plotted. The Co oxide sample was produced by annealing pure cobalt powder on air. It can be seen that the absorption edge shifts to higher energy due to the oxidation process. The spectra of two different, but in the same way produced, Co-Dia composites exhibit same characteristics. Their absorption edges are shifted to higher energy in the same way as the one of the Co oxide sample. The spectra of the Co-Dia and the CoCr-Dia samples show significantly structural changes compared to the reference Co powders respectively the oxidized Co powder. Differences between the Co-Dia and the CoCr–Dia samples can be seen above their absorption edges. This indicates that the local structure of these composites is different. This may be caused by the presence of Chromiumcarbides as Cr is known to be high reactive in forming carbides.

All in all these spectra exhibit different characteristics indicating interesting information about the local structure of the Co diamond interfacial area. Therefore this first eye up analysis needs to be replaced by a detailed analysis.

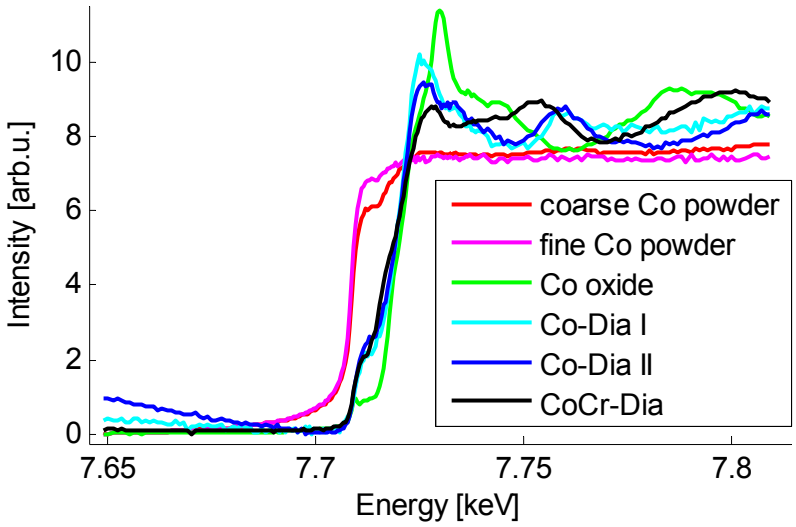

Figure 1: Co K-edge of Co diamond composites and Co references.

The spectra of FeCu and FeCrCu diamond composites as well as the ones for pure Fe and Fe oxide are shown in Figure 2. While all pre-edges are located at the same energy the absorption edges are shifted to higher energies in comparison to the Fe reference. The Fe oxide and the FeCu-Dia spectra are very similar. This may indicate that instead of forming ironcarbides the bigger part of the iron oxidized during the production process. Only the FeCrCu-Dia sample shows significant structural changes.
These data needs also to be analysed in detail to extract reliable informations.

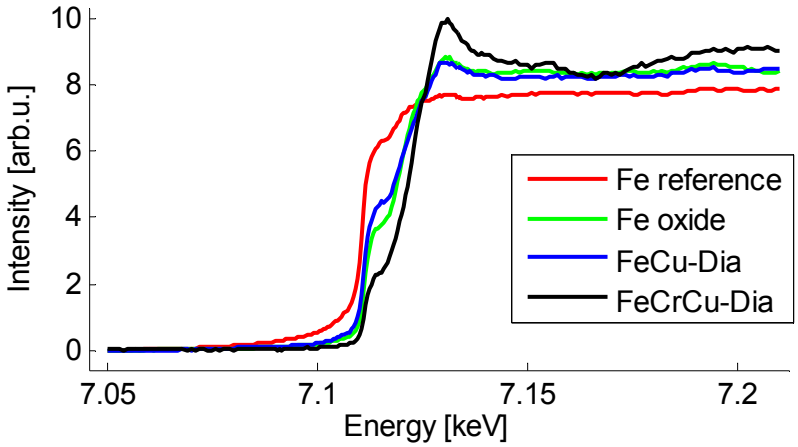

Figure 2: Fe K-edge of Fe diamond composites and Fe references.

References

[1] Denkena et al., Werkstofftechnik online, 6:290-296, 2006..
[2] Tillmann et al., Materialwissenschaften und Werkstofftechnik, 38(2):112-115, 2007.
[3] Molinari et al., Material Science and Engineering, 130:257-262, 1990.
[4] Steffen et al., Report DELTA User Meeting, 2009.

Temperature induced phase separation and nanocrystal formation in bulk amorphous $Si_xGe_yO_z$ with high Ge amount

A. Nyrow[1], Ch. J. Sahle[1], C. Sternemann[1], A. Schwamberger[1], R. Wagner[2], A. Hohl[3], and M. Tolan[1]

[1]Fakultät Physik/DELTA, TU Dortmund, D-44221 Dortmund, Germany

[2]Fachbereich C- Abteilung Physik, Bergische Universität Wuppertal, D-42097 Wuppertal, Germany

[3]Institute for Materials Science, Darmstadt University of Technology, D-64287 Darmstadt, Germany

Due to their unique physical properties oxide matrix embedded semiconductor nanocrystals became very interesting for a high number of applications since their discovery in the 90's, e.g. for the development of fast and stable non-volatile memory devices, efficient light emitting diodes or non-toxic biological markers [1-3]. Here, annealing of amorphous $Si_xGe_yO_z$ precursors leads to SiO_2 embedded Ge nanocrystal formation [4]. In this study, x-ray diffraction (XRD) and x-ray absorption near-edge structure (XANES) spectroscopy at the Ge K-edge have been used to investigate the temperature induced phase separation and nanocrystal formation process in $Si_{0.25}Ge_{0.25}O_{0.5}$.

Amorphous $Si_{0.25}Ge_{0.25}O_{0.5}$ samples were prepared by evaporation of SiO at 1300°C and GeO at 1000°C with a ratio of 1:1 in vacuum and subsequent condensation on a molybdenum substrate. The samples were afterwards annealed for 30 minutes in an inert argon atmosphere at different temperatures between 300°C and 1000°C to induce phase separation as well as Ge nanocrystal formation.

XRD measurements were performed at beamline BL9 using the MAR345 image plate detector with an incident energy of 12.6 keV and an angle of incidence of 3°. The corresponding XRD patterns are presented in figure 1.

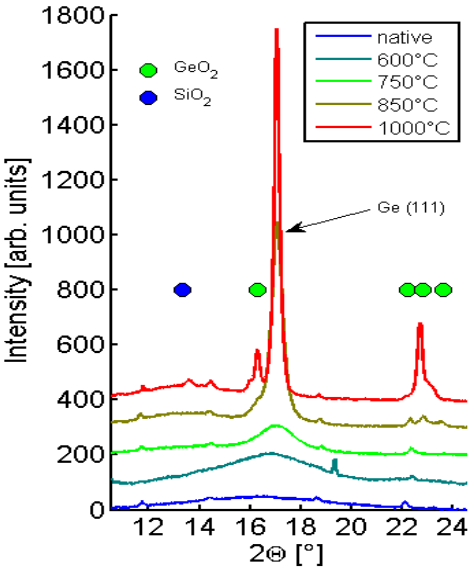

Figure 1: XRD pattern of native and annealed $Si_{0.25}Ge_{0.25}O_{0.5}$

The pattern of the native sample does not show any Bragg reflections. A significant variation of different bonding lengths generates a broad maximum in the XRD pattern indicating a highly amorphous structure of the native $Si_{0.25}Ge_{0.25}O_{0.5}$. With increasing temperature the Ge (111) Bragg reflection can be observed indicating Ge nanocrystal formation. Moreover, the broad maximum at $2\Theta = 13.3°$ can be associated with amorphous SiO_2 formation in favor of a structure where Ge nanocrystals are embedded in a glassy SiO_2 matrix.

To investigate the nanocrystal formation process XANES measurements at the Ge K-edge were performed at beamline BL8 using the Si (111) monochromator and a Passivated Implanted Planar Silicon (PIPS) Detector. The Ge K-edge is known to be very sensitive to the changes of the oxidation state in Ge resulting in an energy shift of the absorption edge by several eV [5,6]. XANES spectra of differently annealed $Si_{0.25}Ge_{0.25}O_{0.5}$ samples are presented in figure 2. The spectrum of the native sample seems to consist of a high amount of pure Ge and GeO_2. Additionally, significant amount of Ge suboxides can be observed. Between 400°C and 700°C the spectral intensity decreases at about 11.106 keV and increases at 11.111 keV which is a typical sign of phase separation of Ge suboxides to pure Ge and GeO_2 as it was observed e.g. in amorphous GeO [6]. At higher temperatures the spectra show a Ge cluster formation and a reduction of GeO_2 to Ge by Si ($GeO_2 + Si \rightarrow Ge + SiO_2$). These results complemented with measurements of the Si L-edge using x-ray Raman scattering yield a detailed description on how Si oxidation can be used to produce SiO_2 embedded Ge nanocrystals from amorphous $Si_xGe_yO_z$.

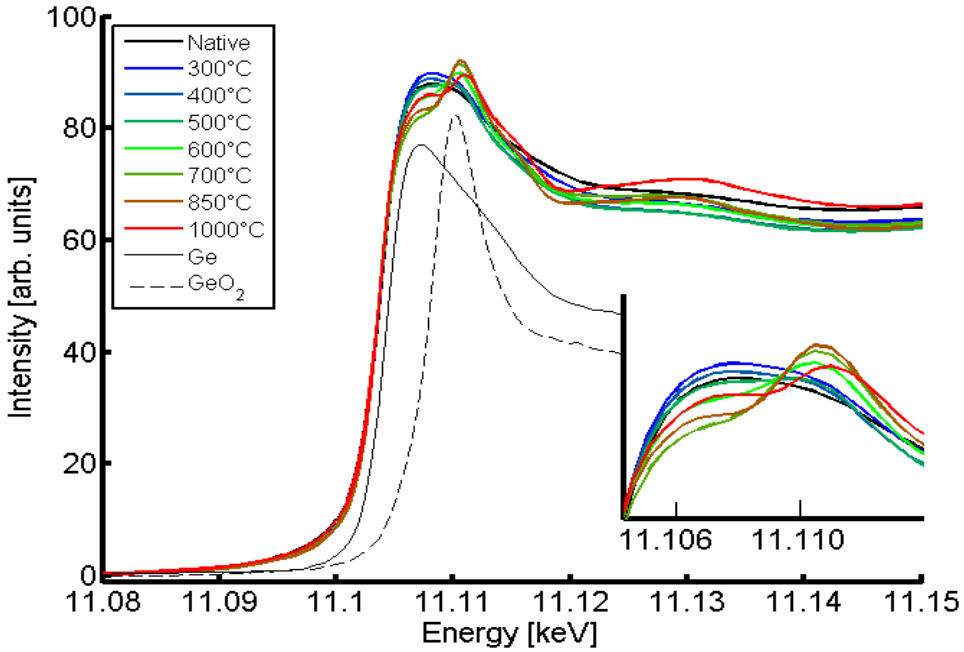

Figure 2: XANES spectra of the native and annealed $Si_{0.25}Ge_{0.25}O_{0.5}$ sample.

[1] L. Pavesi, L. Dal Negro, C. Mazzoleni, G. Franzo, F. Priolo: Nature **408**, 440 (2000); [2] W.-R. Chen, T.C. Chang, P.T.Liu C.H. Tu, J.L. Yeh, Y.T. Hsien,R.Y. Wang, C.Y. Chang: Surface & Coating Technology **202**, 1333 (2007); [3] M. Bruchez, M. Moronne, P. Gin S. Weiss, A.P. Alivisatos: Science **281**, 2013 (1998); [4] M. Zschintzsch, Ch.J.Sahle, J. von Borany, C. Sternemann, A. Mücklich, A. Nyrow, A. Schwamberger, and M. Tolan: Nanotechnology in print (2011); [5] Ch.J.Sahle, M. Zschintzsch, C. Sternemann, J. von Borany, A. Mücklich, A. Nyrow, N.M. Jeutter, R. Wagner, R. Frahm, M. Tolan: Nanotechnology **22**, 125709 (2011); [6] Ch. J. Sahle, C. Sternemann, H. Conrad, A. Herdt O.M. Feroughi, M. Tolan, A. Hohl, R. Wagner, D. Lützenkirchen-Hecht, R. Frahm, A. Sakko, K. Hamalainen, Appl. Phys. Lett. **95**, 021910 (2009).

Investigation of TRIP assisted Q&P steels

Niko Große-Heilmann[(a)], Christian Kronholz[(a)], Andreas Peters[(a)],
Andre Steffen[(b)], Karin Rüster [(b)], Metin Tolan[(b)]

[(a)] Benteler Tube Management GmbH, Paderborn

[(b)] Fakultät Physik/DELTA, TU Dortmund

Introduction

The so-called Quenching and Partitioning (Q&P) process was originally proposed in 2003 by J. G. Speer, D. K. Matlock and B. C. Cooman [1]. As shown in figure 1, the quenching and partitioning heat treatment creates a three-phase microstructure, consisting of low carbon martensite m1, high carbon martensite m2 and retained austenite γ.

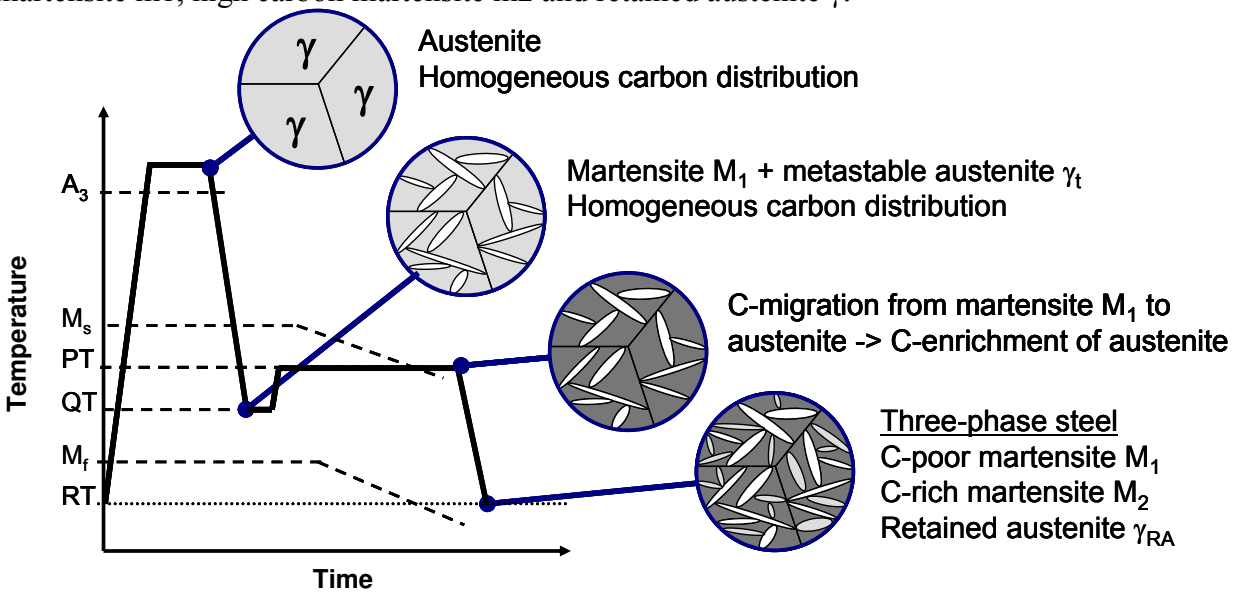

Figure 1: The Quenching and Partitioning Process [2]

During the quenching step the steel is fully austenized and then quenched to a temperature between the martensite start and martensite finish point. Due to the suppressed cementite precipitation due to the high silicon or aluminium content, the carbon diffuses from super-saturated martensite m1 to austenite during the subsequent partitioning phase. Because of the austenite stabilising effect of carbon, the martensite finish temperature of the carbon-enriched austenite is decreased below room temperature. Hence, after final quenching to room temperature, high carbon martensite m2 is formed and carbon-enriched austenite remains. This metastable retained austenite shows TRIP[1] behaviour during mechanical loading. As a result superior mechanical properties are achievable.

Experiments

The amount of retained austenite was studied on samples of 3 mm diameter and 10 mm length made from 0.2 wt.% C, 1.75 wt.% Mn, 1,75 wt.% Si low alloyed steel which were heat treated on a high speed quenching dilatometer. Samples were heated at 10K/s and austenized at 950 °C for 300 s, quenched at 40 K/s to 300 °C and 250 °C, partitioned for 10 s, 100 s, 1000 s, 2000 s and 4000 s and afterwards quenched at 40 K/s to room temperature. Samples were cut into disks of 0.4 mm thickness for transmission XRD experiments on DELTA Beamline 9.

[1] Transformation Induced Plasticity

Image Plate detector MAR345 was used to analyse cubic face centered austenite and cubic body centered ferrite at 350 mm sample to detector distance and 27 keV photon energy.

Results

Reference Intensity Ratio Method was used to determine the retained austenite fraction from [200], [220] austenite and [200], [211] ferrite intensities. I/I_c values were calculated with Powder Cell Software. The results are shown in figure 2.

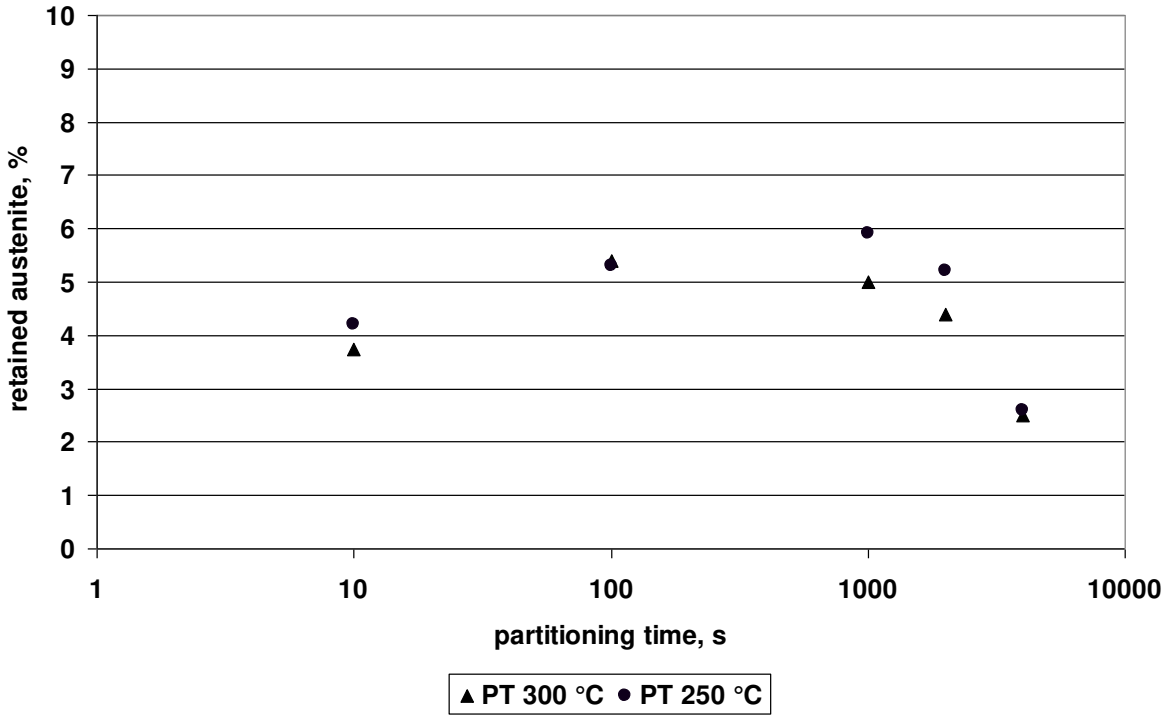

Figure 2: Effect of partitioning time on retained austenite

Highest amount of retained austenite was achieved at 250 °C partitioning temperature and 1000 s partitioning time. Development of the results furthermore supports the theory of a austenite stabilizing (carbon diffusion into austenite) and a degenerating (carbide formation) effect. The higher partitioning temperature shows faster stabilization and degeneration because of accelerated carbon diffusion.

In-situ heat treatment experiments are planned to investigate the phase transformations and the diffusion of carbon during Q&P and in subsequent tempering processes. We will use a high temperature sample cell. The sample cell will enable both high temperature up to 1000 °C and quick cooling up to -40 K/s. To avoid oxidation processes during the experiment the cell will be flushed by inert gas. In further work the TRIP effect (degradation of retained austenite fraction due to deformation) should be shown by interrupted tensile tests or by in-situ tensile testing.

References

[1] Speer, J.; Matlock, D. K.; Cooman, B. D. and Schroth, J., 'Carbon partitioning into austenite after martensite transformation', Acta Materialia 51(9), 2611-2622, (2003)

[2] Matlock, D.; Bräutigam, V. and Speer, J., Application of the Quenching and Partitioning (Q&P) Process to a Medium-Carbon, High-Si Microalloyed Bar Steel, in 'Materials Science Forum', Trans Tech Publications Ltd, pp. 1089-1094, (2003)

Temperature-induced denaturation of protein layers at solid-liquid interfaces - an x-ray reflectivity study

Irena Kiesel, Michael Paulus, Julia Nase, Sebastian Tiemeyer, Christian Sternemann, and Metin Tolan

Fakultät Physik/DELTA, TU Dortmund, Maria-Goeppert-Mayer-Str. 2, 44227 Dortmund, Germany

Protein adsorption at solid/liquid interfaces plays a key role in technical, biomedical, and food processing applications [1–10]. Because proteins lose their functionality during denaturation, the protein adsorption process is crucial for e.g. the acceptance of implants in human bodies and for applications as biosensors.

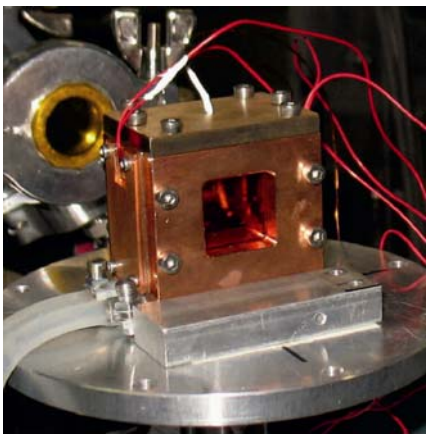

Fig. 1: Heating cell for reflectivities at solid/liquid interfaces.

In our experiment we have investigated the denaturation process induced by increasing temperature. Until now, these types of experiments were performed in protein solutions. However, because such a solution represents a protein reservoir, further protein adsorption can occur during the heating process. Therefore, we have prepared hydrophilised silicon wafers with a natural oxide layer and placed them in a protein solution until a protein layer was established. Afterwards the wafer was transferred into pure buffer solution. The used model proteins are lysozyme, albumin and RNase A. In-situ x-ray reflectivity measurements were performed on these protein coated silcon wafers in pure phosphate buffer solution and in protein buffer solution. X-ray reflectivities at different temperatures up to 90°C were recorded using the 27 keV x-ray reflectivity setup of BL9 at the synchrotron radiation source DELTA. A new heating cell was used (see Fig. 1). With this heating cell it is possible to cover a temperature range between room temperature and 90°C with an accuracy of ±1°C. The temperature is measured with a Pt100 temperature sensor and controlled by a feedback loop of a LakeShore 330 controller. Complemental to the electrical heating plates a water heat exchanger plate is installed for temperature stabilization.

The denaturation process could be investigated by analyzing the (layer) electron density profile and thereby information on structural changes of the protein film induced by temperature was obtained (Fig. 2-7).

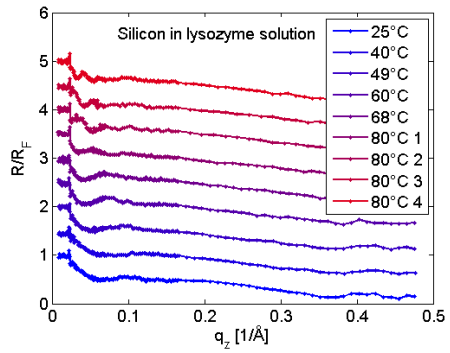

Fig. 2: Normalised and shifted reflectivities of lysozyme on a silicon wafer in protein solution for different temperatures.

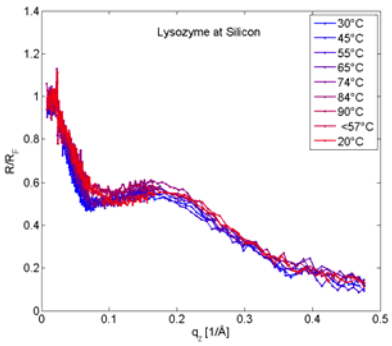

Fig. 3: Normalised reflectivities of lysozyme on a silicon wafer in pure buffer solution for different temperatures.

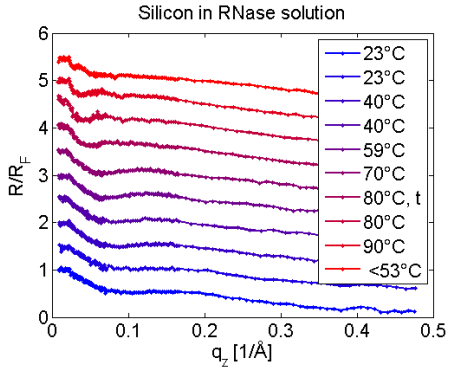

Fig. 4: Normalised and shifted reflectivities of RNase on a silicon wafer in protein solution for different temperatures.

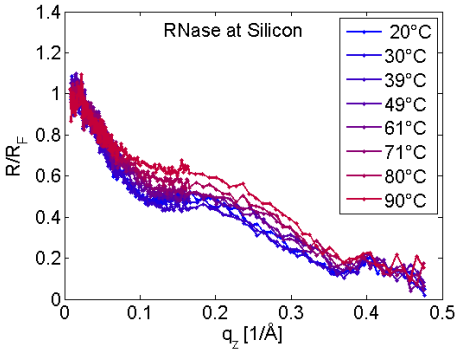

Fig. 5: Normalised reflectivities of RNase A on a silicon wafer in pure buffer solution for different temperatures.

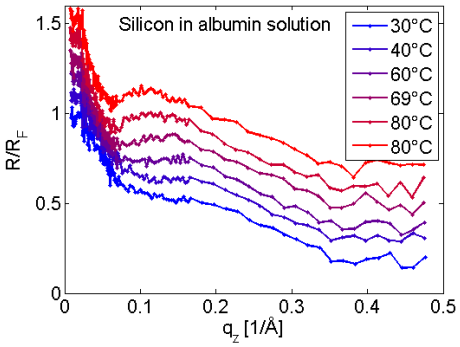

Fig. 6: Normalised and (slightly) shifted reflectivities of Albumin on a silicon wafer in protein solution for different temperatures.

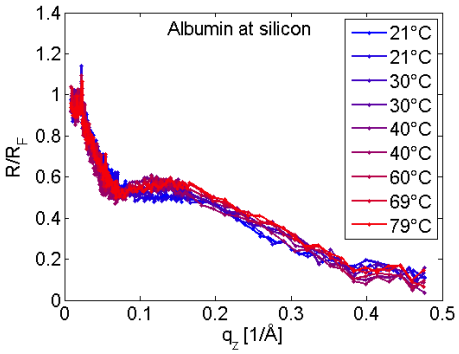

Fig. 7: Normalised reflectivities of Albumin on a silicon wafer in pure buffer solution for different temperatures.

We found differences between the two preparation methods, i.e. using either a protein solution or a pure buffer solution:

- Temperature treatment of protein layers in protein solution causes an increase of layer thickness and can be explained by multilayer formation.
- Only small changes of the temperature treated protein layers in pure buffer were observed which can be explained by small changes in the dispersion (i. e. electron density) and roughness of the adsorbed protein layer.

In the first case, proteins are adsorbed permanently caused by the heating process. Thus, it is difficult to analyze the denaturation process within the adsorbed protein layer. The increased tendency for protein adsorption with increasing temperature might be due to the destabilization of proteins by temperature which results in a higher aggregation rate.
In contrast, in the second case, changes in the reflectivities for different temperatures are caused by changes within the adsorbed protein layer only so that the denaturation process of the adsorbed protein layer is directly observable.
We also found differences between the proteins: The differences between the two preparation methods are larger for lysozyme and RNase A than for Albumin. This might be due to the different size, charge or conformational stability of the proteins. Furthermore we observed a time dependent layer thickness of the protein layer in protein solution during heating at 80°C (Fig. 3). On the time scale of our experiment we did not see saturation of this adsorption prozess.
The data analysis is still in progress and additional measurements will be carried out to study the temperature stability of the adsorbed films in more detail.

[1] A. Baszkin and W. Norde (1999); Physical Chemistry of Biological Interfaces; CRC Press; 1 edition; ISBN 0824775813
[2] C. Czeslik (2004); Zeitschrift fuer Physikalische Chemie; 218 (7-2004): pp. 771_801; doi: 10.1524/zpch.218.7.771.35722
[3] F. Evers, K. Shokuie, M. Paulus, C. Sternemann, C. Czeslik and M. Tolan (2008); Langmuir: The ACS Journal of Surfaces and Colloids; 24 (18): pp. 10.216_10.221; doi:10.1021/la801642s;
[4] F. Evers, C. Reichhart, R. Steitz, M. Tolan and C. Czeslik (2010); Physical Chemistry Chemical Physics; 12 (17): p. 4375; ISSN 1463-9076; doi:10.1039/b925134k
[5] G. Jackler, R. Steitz and C. Czeslik (2002); Langmuir; 18 (17): pp. 6565_6570; doi:10.1021/la025605i
[6] J. Lu, T. Su, P. Thirtle, R. Thomas, A. Rennie and R. Cubitt (1998); Journal of Colloid and Interface Science; 206 (1): pp. 212_223; ISSN 0021-9797; doi: 10.1006/jcis.1998.5680
[7] P. Déjardin, editor (2006); Proteins at Solid-Liquid Interfaces; Springer Berlin Heidelberg; ISBN 978-3-540-32657-1
[8] Castner, D. G.; Ratner, B. D. Surface Science (2002); *500*, pp. 28–60.; doi:10.1016/S0039-6028(01)01587-4
[9] B. Kasemo (2002); Surface Science ; 500 (1-3): pp 656-677, doi: 10.1016/S0039-6028(01)01809-X
[10] M. Tirrell, E. Kokkoli and M. Biesalski (2002); Surface Science; 500 (1-3): pp. 61_83; doi: 10.1016/S0039-6028(01)01548-5

Determination of melting temperatures of strained natural rubber vulcanizates

Benjamin Heuwers*, Robin Hoeher, Dominik Quitmann, Frank Katzenberg, and Joerg C. Tiller

Biomaterials & Polymer Science, Department of Biochemical and Chemical Engineering, TU Dortmund, Emil-Figge-Str. 66, D-44221 Dortmund, Germany

*email: benjamin.heuwers@udo.edu

In 1839 Charles Goodyear discovered the vulcanization of natural rubber (NR, *cis*-1,4-polyisoprene) with sulphur and started the success story of rubber materials. Vulcanizates of *cis*-1,4-polyisoprene distinguish themselves from other rubbers through great physical and mechanical properties in fatigue resistance and, more outstanding, in high tensile strength (20 – 30 MPa) at large elongations (up to 1000 %). This is a consequence of strain-induced crystallization (SIC) which was first verified by Katz [1, 2] in the 1930s by X-ray measurements and thermodynamically described by Flory [3]. Since that the crystallization of vulcanized *cis*-1,4-polyisoprene has been studied for years by different scientific groups and many studies have been carried out concerning the nucleation and growth of crystals at high elongations as well as their disappearance during relaxation [4-6]. Also the melting temperatures in the stretched state have been tried to determine [7, 8] which is a challenging task since usually the strain-induced crystallites disappear on retraction and the rubber becomes completely amorphous.

Recently, we reported on lightly cross-linked *cis*-1,4-polyisoprene-networks which can store high strains through SIC [9] and thus exhibit melting temperatures above room temperature. Beside the great shape memory properties (stored strains up to 1000 %), the melting temperatures of theses strain-induced crystals are physically tunable for one and the same network in a broad range from -25 °C to 50 °C. Melting of these crystals by raising the temperature above the respective melting temperature leads to the retraction of the samples to almost 0 % strain. Moreover, we found out that the crystals can be molten completely athermally without the need of additional heat, just by applying extrinsic stress transverse to their crystals c-direction meaning transversal to the prior strain direction because the melting temperature is suppressed under ambient temperature [10].This effect may be due to increasing intrinsic stress exerted by the amorphous phase. Therefore, we suppose the observed melting temperatures T_m of strain-induced crystals in lightly cross-linked NR networks to be equal to the melting temperature of intrinsically unstressed crystals $T_{m,unstressed}$ reduced by a stress-, elongation-, etc. dependent temperature term $\Delta T(\sigma_t, \varepsilon, ...)$. To verify this hypothesis we investigated the melting temperature of natural rubber vulcanizates exhibiting different strains via synchrotron measurements at DELTA's beamline BL9.

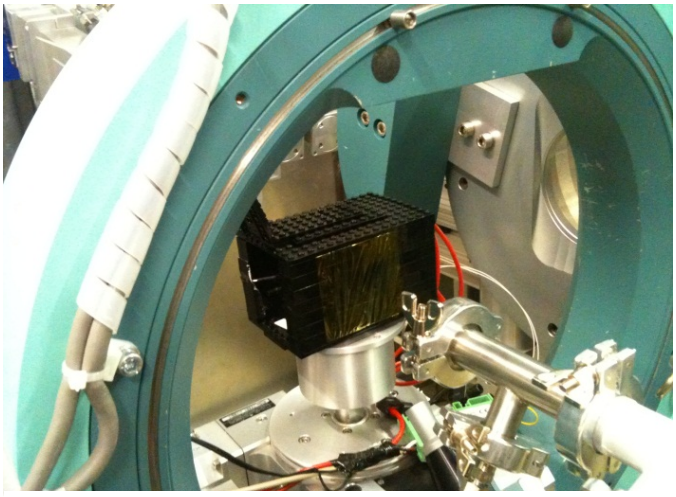

Figure 1: Picture of the measuring device of an acrylonitrile-butadiene-styrene-copolymer at beamline BL9, DELTA.

Materials. For our experiments, different samples of *cis*-1,4-polyisoprene networks were prepared according to the two following general procedures. Pre-vulcanized *natural rubber latex* was obtained by mixing natural rubber latex Neotex FA (Weber & Schaer GmbH) with 0.2 parts per hundred rubber (pphr) sulphur, 0.4 pphr zinc di-n-butyldithiocarbamat and 0.25 pphr zinc oxide cross-linking for 5 h at 50 °C. Subsequently, the natural rubber latex was dried at room temperature using a desiccator for 7 days. Vulcanizates of *solid natural rubber* were achieved by mastication of Standard Malaysian Rubber 10 (SMR 10) for 10 minutes using a heated double-roller operated at 100 °C. Subsequently, the SMR 10 was mixed with 0.15 pphr sulfur, 1 pphr N-Cyclohexyl-2-benzothiazolesulfenamide (CBS), 0.2 pphr zinc oxide and 1.4 pphr stearic acid and masticated for further 5 minutes before vulcanization was carried out in a heating press at 140 °C for 35 minutes.

Synchrotron measurements. Synchrotron measurements were carried out at beamline BL9 at DELTA. The wavelength was 0.08157 nm and the distance from sample to detector was 940 mm. The two-dimensional WAXD patterns were recorded using a Pilatus 100 k detector with exposure times of 30 s for each pattern. Vulcanized *cis*-1,4-polyisoprene samples, clamped and strained to different elongations, were placed in a

measuring device of an acrylonitrile-butadiene-styrene-copolymer (ABS) and were irradiated while the temperature was raised with 1 K/min. This was achieved by using two resistance heating plates placed above and below the samples. The temperature within the ABS-device was measured and controlled by usage of a calibrated resistance thermometer (PT100). The melting temperature of each sample was obtained when the reflections disappeared. An exemplary plot of standardized intensity for (120)- and (200)-reflections of a SMR 10 vulcanizate (0.15 pphr sulphur), strained to 900 %, during temperature increase can be seen in Figure 1a.

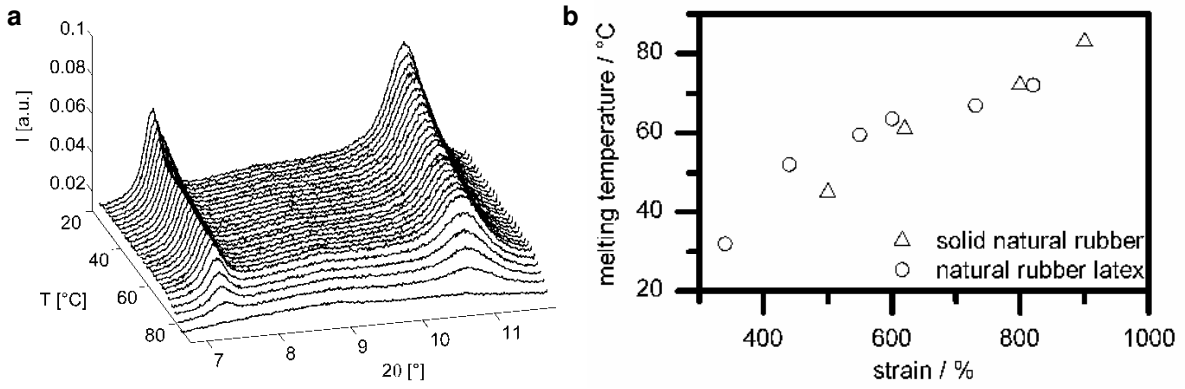

Figure 1: Left: 3D-plot of the (120)- and (200)-reflections versus temperature of a 900% strained SMR 10 vulcanizate.
Right: Melting temperatures of vulcanizates of solid natural rubber and pre-vulcanized natural rubber latex depending on different strains.

Figure 1b shows the melting temperatures of the vulcanizates of solid natural rubber and natural rubber latex for different elongations. Obviously, the melting temperature rises with increasing strain. Since the vulcanizates of natural rubber latex could be strained to a higher elongation than those of solid natural rubber, the maximum melting temperature is higher. The maximum values are $T_{m,NR\ latex}$ = 83 °C and $T_{m,solid\ NR}$ = 72 °C for NR latex and solid NR, respectively. Since the melting temperature of the elongation stabilized crystals does not exceed 50 °C [9] and the maximum melting temperature of the clamped samples is up to 83 °C, our hypothesis that the intrinsic stress exerted by the amorphous phase has a big impact on the melting temperature of natural rubber is justified.

Acknowledgement

The authors acknowledge the DELTA staff for providing synchrotron radiation. Moreover, we thank Continental Reifen Deutschland GmbH, in particular Dr. Fred Waldner and Dr. Tobias Ruckert, for supplying Standard Malaysian Rubber 10 as well as Weber & Schaer GmbH & Co. KG, especially Dr. Andreas Schuch, for providing non-vulcanized natural rubber latex. The research leading to these results has received funding from the Ministry of Innovation, Science and Research of North Rhine-Westphalia in the frame of CLIB-Graduate Cluster Industrial Biotechnology.

References

[1] J.R. Katz, *Naturwissenschaften* **4**,169 (1925).
[2] J.R. Katz, *Transactions of the Faraday Society* **32**, 77 (1936).
[3] P.J. Flory, *Journal of Chemical Physics* **15**, 397 (1947).
[4] G.S.Y. Yeh, *Polymer Engineering and Science* **16**, 138-144 (1976).
[5] S. Toki, B.S. Hsiao, I. Sics, S. Ran, L. Liu, *Polymer* **44**, 6003 (2003).
[6] M. Tosaka, S. Kohjiya, S. Murakami, S. Poompradub, Y. Ikeda, S. Toki, I. Sics, B.S. Hsiai, *Macromolecules* **37**, 3299 (2004).
[7] A.N. Gent, L.-Q. Zhang, *Rubber Chemistry and Technology* 75, 923 (2002).
[8] D.E. Roberts, L. Mandelkern, *Journal of the American Chemical Society* **77**, 781 (1954).
[9] F. Katzenberg, B. Heuwers, J.C. Tiller, *Advanced Materials* **23**, 1909 (2011).
[10] B. Heuwers, D. Quitmann, F. Katzenberg, J.C. Tiller, *Proceedings of the ACS Division of Polymeric Materials: Science & Engineering* **106**, submitted.

The new setup for grazing incidence diffraction measurements at BL9

F. J. Wirkert*, M. Paulus, C. Sternemann, S. Holz, I. Kiesel, M. Tolan
Fakultät Physik/DELTA, TU Dortmund, Maria-Goeppert-Mayer-Str. 2, D-44227 Dortmund, Germany

*email: florian.wirkert@tu-dortmund.de

Grazing incidence diffraction (GID) is a powerful tool to study the lateral structure of thin films such as lipid monolayers at interfaces. Therefore a new setup was installed at beamline BL9, which will be described in the following and the results of first test measurements at the liquid-gas interface will be shown.

The installation of the experimental setup

In a typical GID experiment the incoming x-ray beam hits the sample under a grazing angle which is below the critical angle of external total reflection. Thus, the penetration depth is in the order of a few nanometers yielding a surface sensitive scattering signal. For GID studies on liquid surfaces it is important to measure the intensity of the scattered beam in dependence of the in-plane angle 2Θ in order to obtain large wave vector transfers parallel to the samples' surface. Till now this degree of freedom was not accessible at beamline BL9. To turn the detector in horizontal direction around the sample a new goniometer was installed at the six circle diffractometer.

We used a 2D pixel detector with a sensitive area of $83.8 \times 33.5\,\mathrm{mm}^2$ (PILATUS 100K from DECTRIS) [1]. In front of the detector window a Soller collimator was mounted. This collimator consists of a large number of parallel thin foils, which are coated with gadolinium oxide. The angular resolution of the collimator is $0.1\,^\circ$. The calibration of the angular scale was tested by performing powder diffraction measurements using two different samples. The peak positions in the obtained data of silicon as well as silver behenate are conform with values given in literature.

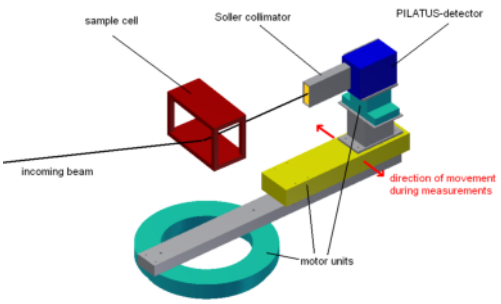

Figure 1: Schematic drawing of the experimental setup.

First test measurements

To realize GID measurements at the liquid-gas interface a sample cell containing a Langmuir trough with the dimensions $100 \times 210\,\mathrm{mm}^2$ was used. The incident photon energy for the experiments was set to 11.5 keV while the angle of incidence was set to $0.09\,^\circ$, which is below the critical angle of water at that energy. First test measurements were made with aqueous iron(II) chloride solution under an ammonia atmosphere. We expected to observe the formation of crystalline structures at the liquid-gas interface between an iron(II) chloride solution (100 mM) and an ammonia atmosphere [2]. Therefore a cup of ammonia (aq. 25%) was placed in the sample cell besides the Langmuir trough, which contained the iron(II) chloride solution. After placing the sample system into the cell several 2Θ-scans were recorded. The obtained data is shown in figure 2.

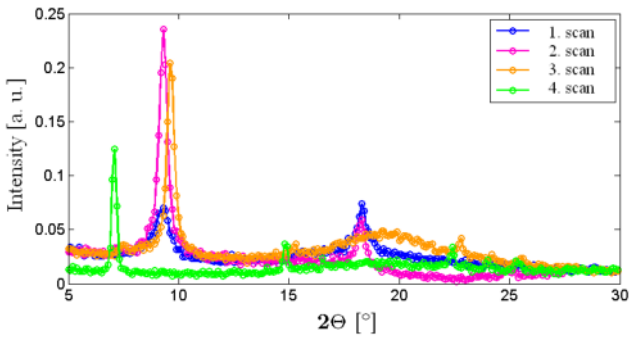

Figure 2: Development of the intensity curves at the iron(II) chloride sample system.

The results obtained from the experiments with iron(II) chloride show the appearance of two different structures. The crystal structure formed at the beginning of the measurements undergoes a phase transition with ongoing duration of the experiment. Comparison with data given in literature [3] show the presence of lepidocrocite in the beginning, while FeOCl was formed at the end of the experiment (see figure 3). Several additional Bragg reflections were visible at the end. These reflections might be caused by amounts of goethite and hematite formed during the experiment. Taking a look at the full width at half maximum of the Bragg reflections one can determine the crystallite size. The analysis of the data shows a growth of the crystallite size during the whole experiment.

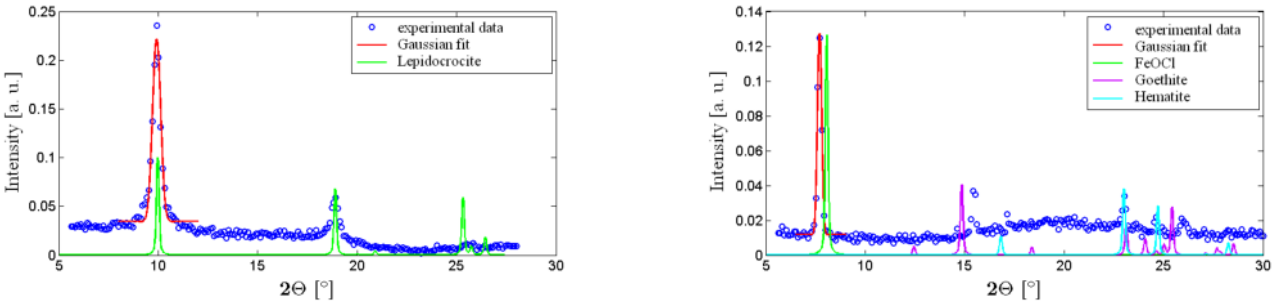

(a) 2. scan

(b) 4. scan

Figure 3: Intensity as a function of the in-plane scattering angle 2Θ for two different scans including Gaussian fit and theoretical intensities.

The authors like to acknowledge the DELTA machine group for providing synchrotron radiation and technical support.

References

[1] Dectris, *User Manual*, 2010

[2] M. Maas, P. Degen, H. Rehage, H. Nebel, M. Epple, *Biomimetic formation fo thin, coherent iron oxide films under Langmuir monolayers*, Colloids and Surfaces A: Physicochem.Eng.Aspects 354 (149-155), 2010

[3] *American Mineralogist Crystal Structure Database*, online database, http://rruff.geo.arizona.edu/AMS/amcsd.php, Stand: 22.07.2011

CO_2 adsorption experiments on $[Zn_2(BME\text{-}bdc)_2(dabco)]_n$ thin films

D.C. Florian Wieland,** Denise Zacher,* Sebastian Henke,* Christan Sternemann,**Michael Paulus**; Metin Tolan** and Roland A. Fischer*

* Lehrstuhl für Anorganische Chemie II, Ruhr-Universität Bochum, Universitätsstr. 150 44801 Bochum
** Experimentelle Physik I, Technische Universität Dortmund, Otto-Hahn-Strasse 4 44221 Dortmund

MOFs represent a young class of inorganic-organic hybrid materials possessing extraordinary porosity and huge specific surface areas. These zeolite-type structures are constructed from rigid organic linkers (e.g. 1,4-benzenedicarboxylate), which connect inorganic building units (metal ions or metal(-oxo) clusters). Due to a modular building principle MOFs offer the possibility to tune their properties on the molecular level for specific applications in gas storage, separation, and chemical sensing.[1,2] Some MOFs exhibit remarkable structural flexibility (drastic changes of cell parameters) in response to external stimuli, e.g. temperature and adsorbed guest molecules.[3] However, the reasons for the framework dynamics and the underlying processes remain poorly understood. Elaborated investigations of this so called "breathing effect" are strongly necessary to gain detailed information about the mechanisms of adsorption in the flexible frameworks. A major requirement for the utilization of MOFs in sensing applications or as membranes for gas separation is the defined growth of MOF thin films on various surfaces (e.g. Au wafers, porous alumina or titania).[2] Numerous concepts for the fabrication of polycrystalline MOF coating are reported. Most of them are based on direct deposition methods, such as the growth under solvothermal conditions or using a special pre-treated mother solution. Besides, reports on the fabrication of perfect MOF thin films, so called SURMOFs (surface grown metal-organic frameworks) following the stepwise Layer-**b**y-**L**ayer (LbL) deposition technique came up.

In previous studies the CO_2 adsorption behavior of powder samples of MOF **1** ($[Zn_2(BME\text{-}bdc)_2(dabco)]_n$ (1; BME-bdc = 2,5-bis(2-methoxyethoxy)-1,4-benzenedicarboxylate; dabco = diazabicyclo[2.2.2]octane)) was investigated.[5] A reversible adsorption behavior accompanied by structural changes could be observed.

In this work we have investigated the structural changes of 20 µm thick films of **1** grown on special functionalized gold substrates upon adsorption of CO_2. *In-situ* pressure depend X-ray diffraction measurements were performed at beamline BL9 of Detla. The experiments were performed at 195 K, using a closed cycle cryostat. For the experiment a

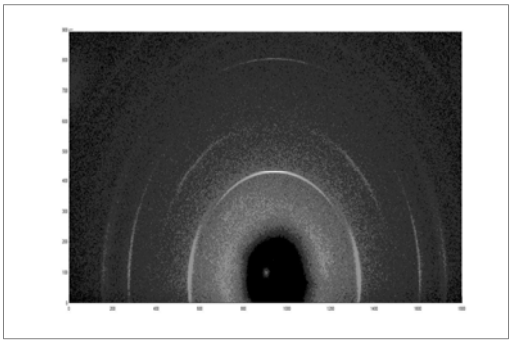

Figure1: Two-dimensional x-ray scattering pattern. In the vertical (horizontal) direction the wave vector transfer is perpendicular (parallel) to the surface.

MAR345 detector and an X-ray energy of 27keV was used.[6] In order to examine if a successful oriented growth could be achieved, coating of **1** were investigated with respect to their orientation. Figure 1 shows a two-dimensional scattering pattern of **1** deposited on a pyridyl-terminated surface. In this pattern a texture can be observed clearly showing an oriented growth of **1** on the substrate.

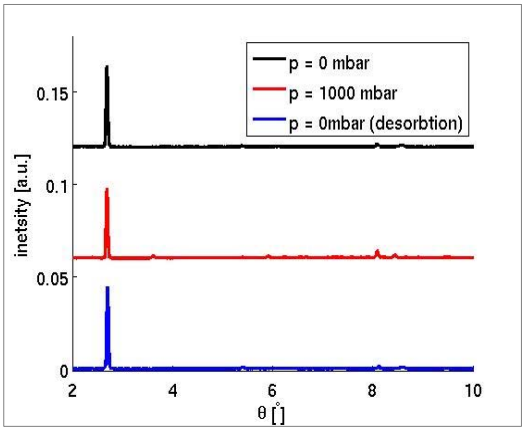

Figure 2: X ray scattering pattern of the [001] scan direction (vertical to the surface) as function of CO_2 pressure.

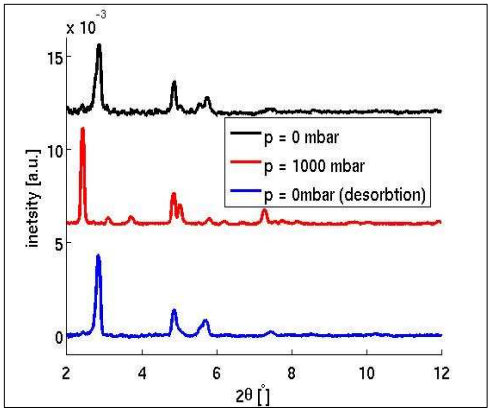

Figure 3: X ray scattering pattern of the lateral scan direction (parallel to the surface) as function of CO_2 pressure.

In order to investigate if the CO_2 adsorption behavior is influenced by the anchoring of the MOF on a substrate, CO_2 adsorption experiments at 195K were performed. The low temperature was needed to achieve a CO_2 saturation at a reasonable gas pressure of 1 bar. Figure 2 and Figure 3 show a selection of the obtained diffraction data on the sample system along the scattering direction perpendicular and parallel to the sample surface. The data show no changes in [001] direction upon CO_2 adsorption (Figure 2), which is in accordance to the scattering data of the powder sample. However, the diffraction pattern parallel to the sample surface shows a shift of the (110) reflection if CO_2 is present, indicating a pore opening due to CO_2 adsorption (Figure 3). Evacuating the sample volume afterwards, the reflection shifts back to the initial state indicating a successful removal of CO_2.

In conclusion, the experiments show the successful growth of oriented layers of **1** on functionalized gold substrates. The responsive behavior of thin films of **1** is thereby not influence by anchoring on a substrate.

[1] G. Ferey, Chem. Soc. Rev., 2008, **37**, 191.
[2] a) D. Zacher, O. Shekhah, C. Wöll, R. A. Fischer, Chem. Soc. Rev., 2008, **38**, 1418; b) D. Zacher, R. Schmid, C. Wöll, R. A. Fischer, Angew. Chem.Int. Ed., 2011, **50**, 176.
[3] G. Ferey, C. Serre, Chem. Soc. Rev., 2009, **38**, 1380.
[4] D. Zacher, K. Yusenko, A. Betard, S. Henke, M. Molon, T. Ladnorg, O. Shekhah, B. Schüpbach, T. de los Arcos, M. Krasnopolski, M. Meilikhov, J. Winter, A. Terfort, C. Wöll, R. A. Fischer, Chem. Eur. J., 2011, **17**,1448.
[5] S. Henke, D. C. F. Wieland, M. Meilikhov, M. Paulus, C. Sternemann, K. Yusenko and R. A. Fischer CrystEngComm, **13,** 6399 (2011)
[6] C. Krywka, C. Sternemann, M. Paulus,N. Javid, R. Winter, A. Al-Sawalmih, S. Yi, D. Raabe, and M. Tolan, J. Synchrotron Rad. **14**, 244 (2007).

Protein Adsorbates on Hydrophobic Surfaces.

Hendrik Hähl[a], Peter Loskill[a], Almuth Hoffmann[a], Mischa Klos[a], Irena Kiesel[b] Michael Paulus[b], Christian Sternemann[b], Metin Tolan[b] and Karin Jacobs*,[a]
[a] *Experimentalphysik, Universität des Saarlandes, D-66041 Saarbrücken,*
[b] *Fakultät Physik/DELTA, TU Dortmund, D-44221 Dortmund*

*email: k.jacobs@physik.uni-saarland.de

Introduction

Surfaces that come into contact with a protein containing solution will quickly be covered by adsorbed proteins. Since the resulting protein adsorbate acts as a conditioning film for later biofilm development, the adsorption process is of great importance in biomedical as well as technical applications. Thereby, the adsorption behavior is influenced by a large number of parameters, describing the solution as well as the surface [1].

In former studies, we distinguished substrate influences arising from the substrate's surface from the ones arising from the subsurface composition of the substrate [2, 3]. It could be shown that the subsurface composition mainly influences the absolute adsorbed amount of protein whereas the surface chemistry determines wether the proteins denature. It was found that proteins strongly denature on samples that were rendered hydrophobic by a silane coating [3]. On polystyrene (PS) and on silica, however, a protein film thickness was measured that corresponds to adsorbed proteins in a nearly native conformational state [4]. The applied surfaces differ not only in surface energy, which is the property that defines wether a surface is hydrophobic or -philic, but also in their atomic structure: PS and silica exhibit an amorphous structure whereas the silanes form a two-dimensional crystalline layer. PS is also a hydrophobic material, yet with a still higher surface energy than the silane coating. Since the strong denaturation was only found on the silane surfaces, it is not clear which parameter is the more relevant for this process: the very low surface energy or the ordered structure.

For the reported experiments, different hydrophobic surfaces (crystalline and amorphous, and with differences in surface energy) have been brought into contact with protein solutions. The resulting adsorbates have been measured *in situ* using high energy (27 keV) X-ray reflectometry. As previous studies have shown [4, 5], this methodology is well-suited for the study of adsorbed protein films at solid-liquid interfaces.

Experiments and Results

As common basis for all substrates, silicon wafers with a thermally grown silicon oxide thickness of 160 nm (Silchem, Freiberg, Germany) were used. These wafers were coated by different types of silanes: two silanes with pure hydrocarbon chains but different lengths (*dodecyltricholorsilane*, DTS, with 12 and *octadecyltrichlorosilane*, OTS, with 18 C-atoms in the backbone) and a perfluoronated silane, FDS. Thus, crystalline layers with CH_3 and CF_3 surfaces were obtained. Amorphous layers were produced by dip-coating substrates with the fluoropolymer AF1600 (prod. no. 469610, Sigma-Aldrich, Steinheim, Germany), which exhibits nearly the same surface energy as the FDS surfaces. To ensure an adhesion of the AF1600 layer on the substrate even immersed in water, OTS covered wafers were used instead of pure silicon wafers. As proteins, bovine serum albumin (BSA) and the hydrophobin HFBI are used. The former has a mass of 66 kg/mol and tends to denature upon adsorption on OTS [3], the latter is a relatively small protein (7.5 kg/mol) and structurally very stable [6]. Furthermore, HFBI is strongly amphiphilic and hence it tends to adsorb with its hydrophobic part to hydrophobic surfaces.

BSA was dissolved in a 10 mM phosphate buffer solution (pH 7), for HFBI, acetate buffer (10 mM) at pH 5 was used. For the reflectivity measurements, the substrates were put in a closed teflon cell and immersed in the respective buffer. First a reference measurement of the substrate was performed. Then protein solution was added, such that a protein concentration of 0.1 mg/ml in the cell was achieved. After equilibration of the system, the final measurement was made. The reflectivity measurements were carried out on the beamline BL9 at the DELTA synchrotron light source with the X-ray reflectivity set-up in a θ-2θ geometry and a photon energy of 27 keV optimized to access solid-liquid interfaces.

In figure 1, examples of the obtained reflectivity data are shown. The characteristics of the respective substrates are clearly visible: Already from the raw data, the oscillations in the data with their distinct frequency can be attributed to the different layers of the substrate. (For $q_z > 0.26\,\text{Å}^{-1}$, the point density was reduced resulting in an apparent change of the oscillations.) Moreover, the contribution of the protein adsorbate is evident by comparison with the respective reference measurement. For a comparison of the adsorbate layers, however, a detailed analysis is mandatory as the contrast in electron density differs for every adsorbate/substrate system studied.

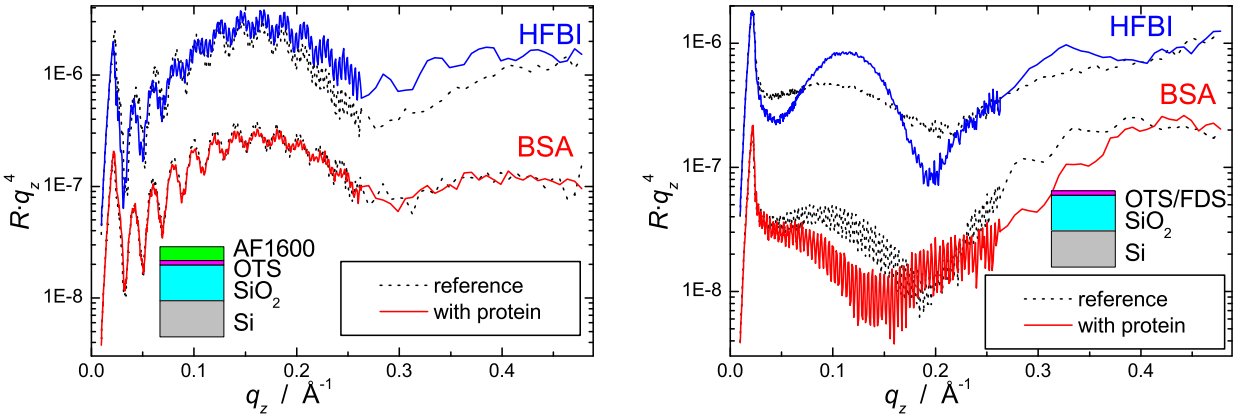

(a) (b)

Figure 1: (a) Reflectivity data of adsorbates of HFBI (top datasets, blue) and BSA (lower datasets, red) on an amorphous hydrophobic surface (covered with AF1600), reference data are shown as dotted lines. (b) HFBI (top datasets, blue) and BSA (lower datasets, red) on crystalline surfaces (OTS for HFBI and FDS in the case of BSA). The graphic inset shows the respective substrate's layer system.

Conclusion

Using high energy X-ray reflectivity, protein adsorbates on different hydrophobic substrate were measured. Thereby the structure of the surface was varied (amorphous or crystalline), whereas the surface energy was changed only marginally. By also using proteins with different conformational stability, the influence on the surface structure rather than its surface energy on the denaturation of adsorbed proteins should be tested. The obtained data appear promising. A detailed analysis, however, is still in progress.

Acknowledgments

The DELTA machine group is gratefully acknowledged for providing synchrotron radiation and technical support. We would like to thank the Bundesministerium für Bildung und Forschung, the NRW Forschungsschule 'Forschung mit Synchrotronstrahlung in den Nano- und Biowissenschaften', and the Deutsche Forschungsgemeinschaft for financial support under grant number GRK 1276 and GRK 532.

References

[1] C Czeslik, *Z. Phys. Chem.* **218**, 771 (2004).

[2] M Bellion, L Santen, H Mantz, H Hähl, A Quinn, A Nagel, C Gilow, C Weitenberg, Y Schmitt, K Jacobs, *J. Phys.: Condens. Mat.* **20**, 404226 (2008).

[3] H Hähl, F Evers, S Grandthyll,M Paulus, C Sternemann, P Loskill, M Lessel, A Hüsecken, T Brenner, M Tolan, K Jacobs, *(in preparation).*

[4] F Evers, K Shokuie, M Paulus, S Tiemeyer, C Sternemann, C Czeslik, M Tolan. *Eur. Phys. J.: Spec. top.* (2009) **167**, 185.

[5] F. Evers, K Shokuie, M Paulus, C Sternemann, C Czeslik, M Tolan, *Langmuir* **24**, 10216 (2008).

[6] M. Linder, *Curr. Op. Coll. Int. Sci.* **14** 356 (2009).

Exciton-mediated lattice distortions in InAs/GaAs quantum dots

Sebastian Tiemeyer*,[a], Michael Bombeck[b], Michael Paulus[a], Christian Sternemann[a], Florian Wirkert[a], Manfred Bayer[b], and Metin Tolan[a]

[a] *Fakultät Physik/DELTA, TU Dortmund, Maria-Goeppert-Mayer-Str. 2, D-44227 Dortmund, Germany;*
[b] *Experimentelle Physik II, TU Dortmund, Otto-Hahn-Str. 4, D-44227 Dortmund, Germany.*

*email: sebastian.tiemeyer@tu-dortmund.de

Quantum dot heterostructures are a research topic offering both the discovery of principal knowledge in terms of quantum information processing [1] and the development of optoelectronic devices [2]. The confinement of charge carriers to length scales comparable to the de Broglie wavelength in semiconductor heterostructures such as quantum wells and quantum dots leads to a considerable modification of the density of states (DOS). In particular quantum dots represent zero-dimensional structures possessing a DOS similar to that of atoms. From this attribute arises a wide range of applications.
For example, exploiting these unique properties make quantum dot lasers possible which are superior to semiconductor diode lasers regarding the threshold current density and temperature stability of the threshold current. In terms of quantum cryptography single photon sources based on quantum dots are promising devices for secure key distribution [3]. Also applications as 1.3 μm photonic devices or the development of quantum dots in order to realize qubits for quantum computing are research topics attracting a lot of interest.
A further specific feature is the ability to fabricate structures with atomic precision by self-organized growth. The epitaxial assembly of quantum heterostructures by the Stranski-Krastanov (SK) growth has established as the technique of choice leading to well defined quantum dots with a narrow size distribution. Based on the deposition of material on a substrate of different lattice constant forming a wetting layer, these structures emerge from a minimization of the elastic energy at the expense of the surface energy. Indium arsenide (InAs) and gallium arsenide (GaAs), growing both in the zinc blende structure, exhibit a lattice mismatch of 7%. This attribute predestines these materials for the SK growth giving rise to considerable strain fields in quantum dot heterostructures. The strain affects significantly the electronic properties of quantum dots e.g. the band structure and gap [4,5].
Previous x-ray studies have determined the strain distribution in non-excited quantum dots [6,7]. Optically excited quantum dots have shown lattice distortions attributed to injected charge carriers which have been monitored indirectly by high resolution continuous wave or non-linear time-resolved optical spectroscopy [8-12]. To detect directly these lattice distortions, we have applied at the beamline BL9 anomalous x-ray diffraction in combination with a laser shutter system and a liquid helium flow cryostat setup. The laser system consisted of a Klastech Symphony Nd:YAG laser device operating at a wavelength of 532 nm with an output power of 1 W (cw) which enabled us to excite the whole sample. The cryogenic environment was essential for suppressing the non-radiative recombination of the charge carriers in the quantum dots. Therefore, we have ensured that the x-ray beam probed a sample area containing only excited quantum dots. The state of excitation of the quantum dots was monitored in situ by photoluminescence spectra.
The experiments were performed with an InAs/GaAs quantum dot multilayer structure grown on a (001) oriented GaAs substrate. The sample consisted of 5 quantum dot layers separated by 30 nm GaAs spacing layers and capped with 50 nm GaAs. The 5 period multilayer structure guaranteed a high amount of quantum dots in the volume probed by the x-ray beam. The density of the InAs/GaAs quantum dots was 10^{10} cm^{-2}. The capped quantum dots had a base diameter and height of approximately 20 nm and 5 nm, respectively [13]. Thus, the quantum dots covered less than 5% of the wetting layers. Moreover, the quantum dots were subject to segregation of gallium during the growth process resulting in an inhomogeneous distribution of indium atoms inside of the dots. Hence, the scattering intensity stemming from the quantum dots was extremely low in comparison to the GaAs matrix.
In order to improve the quantum dots' scattering contribution, we have performed ω - 2θ scans at the (002) superstructure reflection. By choosing a photon energy of 12.38 keV, this reflection allowed the suppression of the scattering amplitude of the GaAs matrix by a factor of 500 based on the scattering amplitude of InAs. Furthermore, due to being above the K-edges of gallium and arsenic, the chosen photon

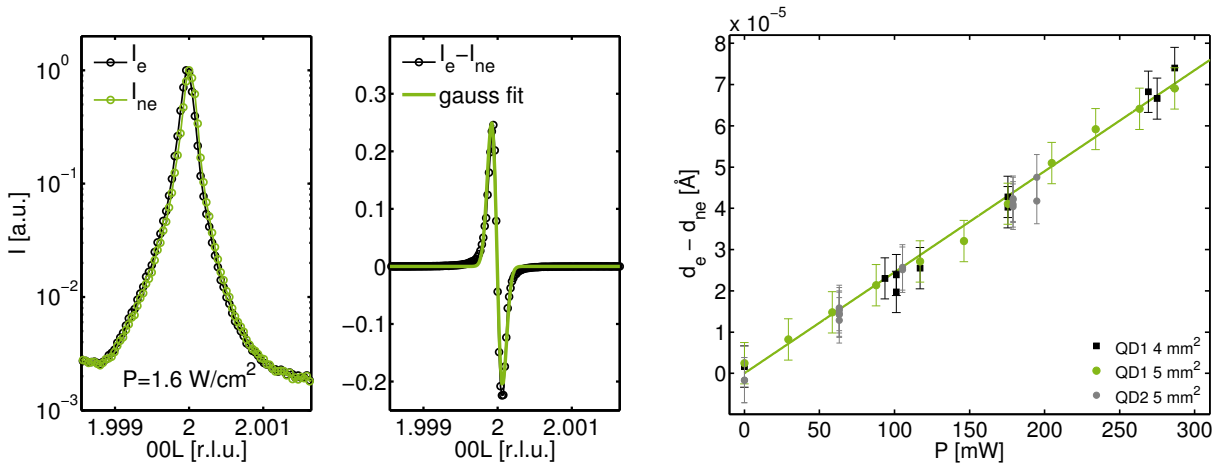

Figure 1: Left: $\omega - 2\theta$ scans of the GaAs(002) superstructure reflection in non-excited and excited state at 100 K. Scans are given in reciprocal lattice units. Middle: Difference plots of the scans collected in excited state and non-excited state I_e-I_{ne}. The data is fitted by the difference of two gauss curves. Right: Lattice expansion as a function of the laser power for different laser spot sizes. QD1 and QD2 denote separately prepared samples.

energy limited the probing depth of the x-rays to 1 μm. Thus, the scattering volume comprised mostly the multilayer structure.

A former x-ray study showed a shift of the GaAs(002) Bragg reflection on laser excitation [14]. On this account, we have conducted a high resolution analysis of the (002) reflection for different excitation powers and densities at a sample temperature of 100 K. Figure 1 , left, depicts a ω - 2θ scan of the (002) reflection in excited and non-excited state of the sample at an excitation density of 1.6 W/cm^2. The laser irradiation caused a shift of the Bragg reflection toward smaller angles corresponding to an expansion of the lattice. The middle part shows the difference of the two Bragg reflections which can be fitted by the difference of two Gaussian curves shifted with respect to each other. The resulting angular shift was converted into the differential expansion of the (002) lattice constant d_e - d_{ne}. This procedure was done for laser powers up to 300 mW and laser spot sizes of 4 mm and 5 mm, respectively, as displayed in the right part of Figure 1. Apparently, the expansion of the (002) lattice constant followed a linear power dependence. In contrast, changing the spot size from 4 to 5 mm had no influence on the lattice's expansion. Excluding an impact from the conductive paste, ensuring the thermal connection of the sample, the experiment was conducted again (denoted as QD2), and was found to be in accordance with the previous results.

In principle, our findings can be explained by a thermal expansion of the lattice. To gain a comprehensive insight into this effect, upcoming experiments will reveal the laser power dependence of the lattice expansion for both the (002) and (200) reflection of the quantum dot sample and a reference bulk GaAs wafer, respectively.

Acknowledgment. The DELTA staff is gratefully acknowledged for providing synchrotron radiation. S. T. thanks the NRW Forschungsschule 'Forschung mit Synchrotronstrahlung in den Nano- und Biowissenschaften' for financial support.

References

[1] F. Henneberger, O. Benson, Semiconductor Quantum Bits (World Scientific, Singapore, 2008). [2] D. Bimberg, M. Grundmann and N. N. Ledentsov, Quantum Dot Heterostructures (John Wiley and Sons, Chichester, 1999). [3] P. Michler et al., *Science* **290**, 2282 (2000). [4] O. Stier et al., *Phys. Rev. B* **59**, 5688 (1999). [5] F. Guffarth et al., *Phys. Rev. B* **64**, 085305 (2001). [6] I. Kegel et al.,*Phys. Rev. Lett.* **85**, 1694 (2000). [7] T. U. Schülli et al., *Appl. Phys. Lett.* **81**, 448 (2002). [8] P. Borri et al., *Phys. Rev. Lett.* **87**, 157401 (2001). [9] P. Borri et al., *Phys. Rev. Lett.* **91**, 267401 (2003). [10] A. Vagov et al., *Phys. Rev. B* **70**, 201305 (2004). [11] B. Krummheuer et al., *Phys. Rev. B* **71**, 235329 (2005). [12] A. Krügel et al., *Phys. Rev. B* **76**, 195302 (2007). [13] J. H. Blokland et al., *Appl. Phys. Lett.* **94**, 023107 (2009). [14] S. Tiemeyer et al., *HASYLAB User Report* 20101166 (2010).

The interface between a solid and a supercritical gas

Sebastian Holz, Michael Paulus, Julia Nase, Thorsten Brenner, Christian Sternemann, Metin Tolan

Fakultät Physik/DELTA, TU Dortmund, Maria-Goeppert-Mayer-Str. 2, 44227 Dortmund, Germany

Adsorption at interfaces is critical for many processes in nature, e. g. formation of gas hydrates, catalysis, enzymatic reactions, or industrial applications like filtering or water purification. The formation of an adsorption layer enhances the gas offer significantly and is thus of importance for transport and exchange processes at membranes and interfaces in nature. More than 100 models have been established to describe the various types of adsorption isotherms. Supercritical adsorption, however, is far less understood, though this phenomenon has been known for some time now [1]. It has tremendous importance in industrial applications like high pressure gas storage systems, Supercritical Fluid Chromatography (SFC), and polymer processing. However, the interface with a possible restructuration of the supercritical molecules has never been measured directly.

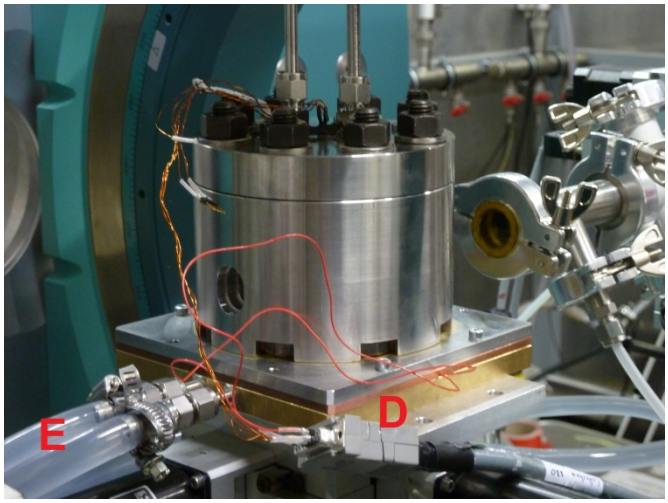

Fig. 1: High pressure cell for reflectivities at solid/liquid and solid/gas interfaces

Until now, most experiments concerning supercritical adsorption were performed using volumetric [2] or gravimetric [3] methods where highly porous solids are exposed to the gas phase and the adsorbed amount can be calculated from pressure respectively mass changes. In our experiments, the electron density profile along the surface normal can be determined from x-ray reflectometry, a reliable and well adapted technique to determine the thickness and roughness of interfaces. X-ray reflectivities at different temperatures and pressures were recorded using the 27 keV x-ray reflectivity setup of BL9 at the synchrotron source DELTA. A new pressure cell was used which can sustain pressure up to 100 bar (Fig. 1).

Figures 2 and 3 show some of the results of carbon dioxide adsorption on a silicon wafer. Figure 2 shows reflectivities of the subcritical temperature region and figure 3 of the supercritical temperature region. In both cases one can see a rise of the layer thickness with increasing pressure which is stronger at lower temperatures. The pressure could not be further increased due to condensation of carbon dioxide in the tubes. The next step should be to exceed the critical pressure (p_C = 73.8 bar). This goal can be reached by some minor changes in the experimental setup (e.g. thermally isolated tubes).

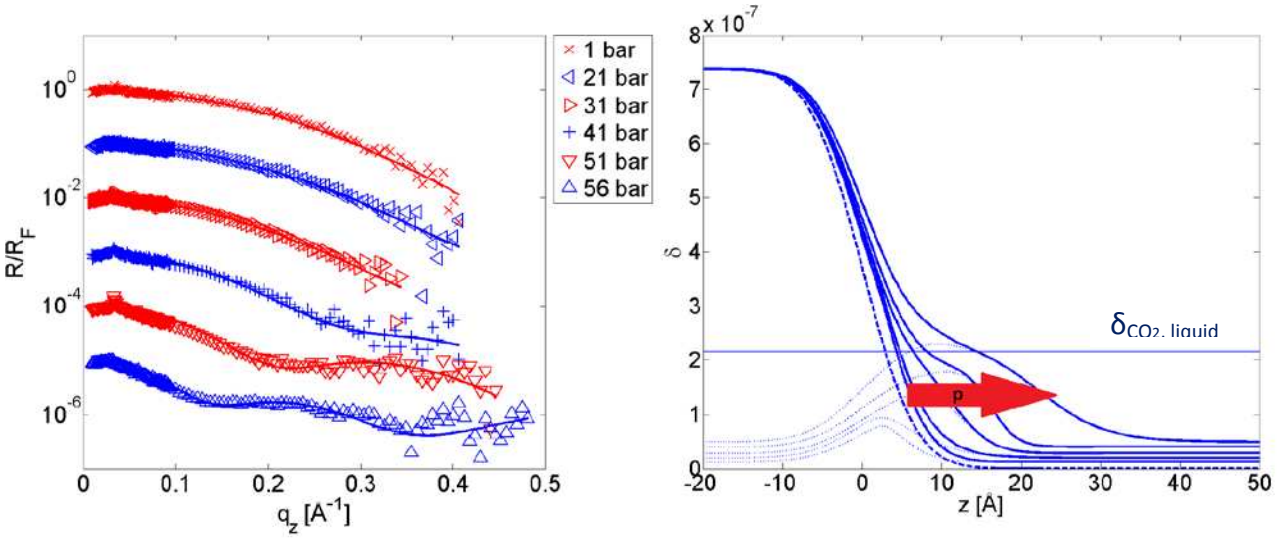

Fig. 2: Normalized and shifted reflectivities of carbon dioxide on a silicon wafer for different pressures at T = 21.5 °C (< T_C = 31 °C) and the corresponding dispersion profiles (dispersion ∝ electron density) perpendicular to the surface.

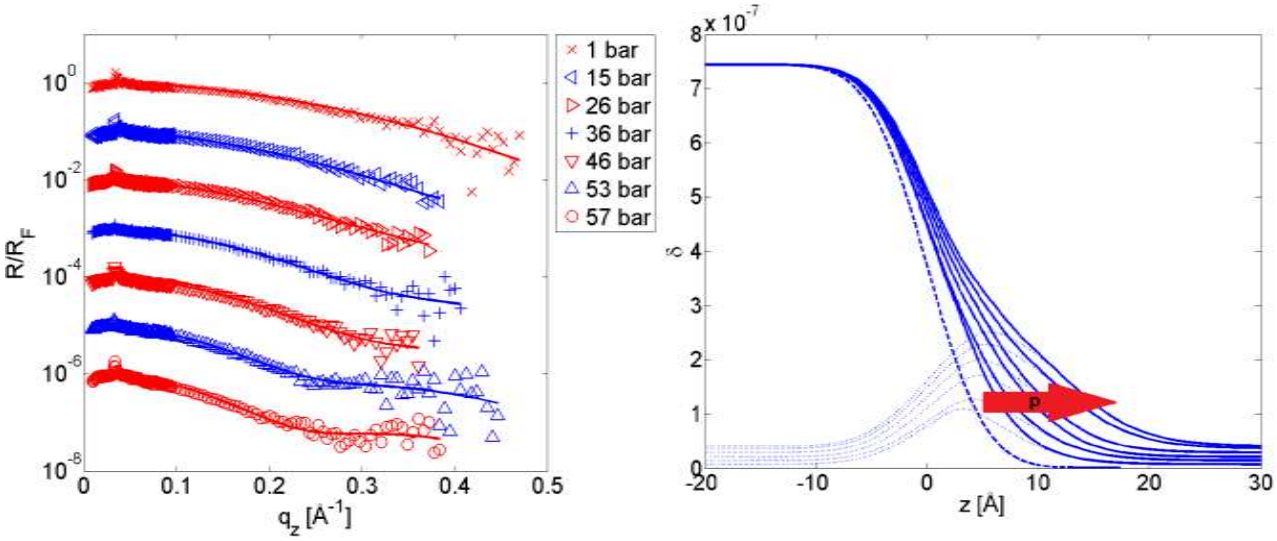

Fig. 3: Normalized and shifted reflectivities of carbon dioxide on a silicon wafer for different pressures at T = 36.7 °C (> T_C = 31 °C) and the corresponding dispersion profiles perpendicular to the surface.

[1] J. Tóth. Adsorption: Theory, Modeling and Analysis. Marcel Dekker, 2002.
[2] L. Zhou, Y. Zhou, S. Bai, and B. Yang. Studies on the transition behavior of physical adsorption from the sub- to the supercritical region: Experiments on silica gel. Journal of Colloid Interface Science, 253:9–15, 2002.
[3] A. Rajendran. Adsorption and chromatography under supercritical conditions. PhD thesis, ETH Zürich, 2004.

Laser-induced lattice distortions in CdSe/CdS core/shell quantum rods

Sebastian Tiemeyer*,[a], Michael Bombeck[b], Michael Paulus[a], Christian Sternemann[a], Julia Nase[a], Manfred Bayer[b], and Metin Tolan[a]

[a] *Fakultät Physik/DELTA, TU Dortmund, Maria-Goeppert-Mayer-Str. 2, D-44227 Dortmund, Germany;*
[b] *Experimentelle Physik II, TU Dortmund, Otto-Hahn-Str. 4, D-44227 Dortmund, Germany.*

*email: sebastian.tiemeyer@tu-dortmund.de

Optically excited low dimensional semiconductor heterostructures have shown strong evidence for lattice distortions triggered by exciton-phonon interactions. For instance, this effect was observed for the III-V group systems InAs/GaAs and InN/GaN by means of high resolution continuous wave or non-linear time-resolved optical spectroscopy [1-3]. A local change in the lattice constant due to the creation of electron-hole pairs was as well monitored for II-VI quantum structures [4]. The strength of the lattice distortions becomes stronger with decreasing size of the confined exciton and accordingly the quantum heterostructure. Hence, this effect is in particular pronounced in quantum nanocrystals exhibiting radii of only a few nanometer.

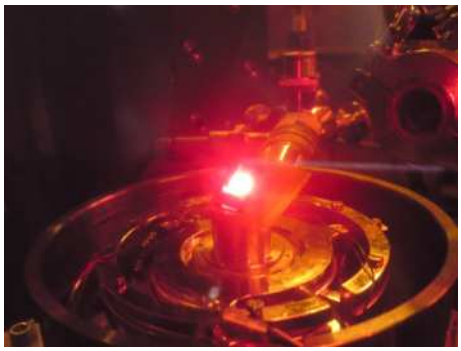

Figure 1: Picture of the optically excited CdSe/CdS core/shell quantum rods.

Therefore, we have investigated the laser-induced lattice distortions in CdSe/CdS core/shell quantum rods (QR) by employing high-resolution x-ray powder diffraction at the beamline BL9 of DELTA. The setup comprised a Pilatus 100k 2D detector and a power tunable Klastech Nd:YAG continuous wave laser system operating at 532 nm which enabled us to excite the QRs by laser irradiation. Sufficient separated Bragg reflections, a good angular resolution and a excellent signal to noise ratio were crucial for the success of our experiment. These requirements were complied by employing the Pilatus detector in a sample detector distance of 831 mm allowing to probe an angular range of 7 degree at an angular resolution of 0.012 degree. Choosing the photon energy to 12.38 keV, the simultaneous measurement of the (010), (002) and (011) wurtzite reflections, located in the scattering angle range from 14.6 to 20.4 degree, was possible giving access to information on every lattice direction. A flight path was necessary for suppressing x-ray scattering from air and thus improved the signal to noise ratio. The beam size was set to 1x1 mm maximizing the available scattering volume.
The quantum rod samples were grown from a CdSe seed of 4 nm size followed subsequently by an asymmetric shell growth of CdS [5]. Originating from this growth mode, the quantum rods exhibited an overall diameter of 4.9 nm and length of 46.1 nm. The in toluene dissolved QRs were dried on a polyimide foil resulting in a highly concentrated powder sample with inhomogeneous density. On this account, the sample stage was equipped with a linear position table to be capable of moving the sample lateral and perpendicular with respect to the x-ray beam. Figure 1 depicts the sample stage showing the visible photoluminescence of an optically active CdSe/CdS core-shell nanorod sample.
A typical powder diffraction image is shown in Figure 2A, exhibiting no texture within the Debye-Scherrer rings. The 2D images of the diffraction pattern were taken in excited and non-excited state of the sample each for 10s, alternately, adding up to an acquiring time of 35 min. This procedure circumvented a biased heating of the sample during laser irradiation. The radially integrated data for an excitation power of 300 mW is depicted in Figure 2B. Indexing identified the reflections as originated from the CdS shell. Due to the high aspect ratio of the quantum rods, the (002) reflection possessed a considerably smaller full width at half maximum (FWHM) with higher peak intensity at the same time. The diffractogram exhibited only minor changes in response to the excitation of the QR sample. Thus, the data is presented in Figure 2C for different excitation powers as the difference of the diffractograms from the excited and non-excited sample emphasizing by this the small features in the data. While on laser irradiation the (010) and (011) reflections were subject to a decrease in peak intensity, the (002) reflection revealed an unanticipated gain in intensity. This effect is reflected by the asymmetric shift to negative values of the difference which

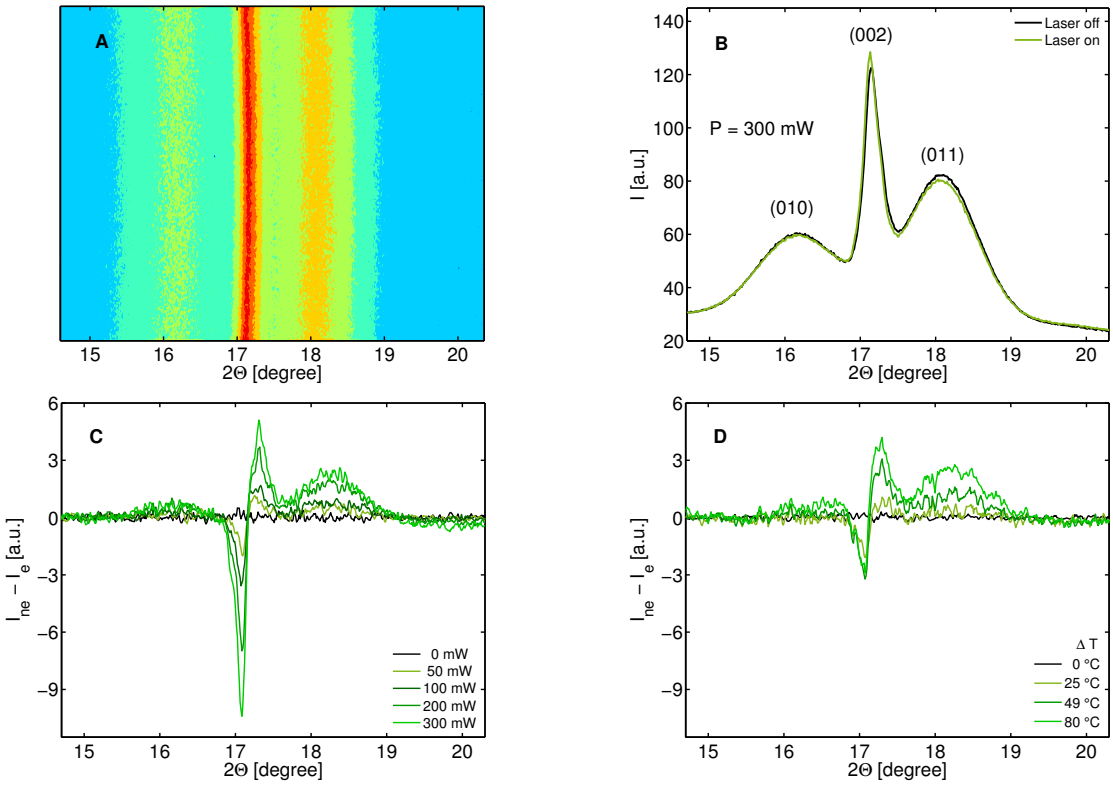

Figure 2: (A) Diffraction pattern of the quantum rods. (B) Corresponding radially integrated diffractogram of the QR sample in excited and non-excited state at an excitation power of 300 mW. Indexing identified the reflections as originated from the CdS shell. (C) Difference of diffractograms from the excited and non-excited sample for different Laser excitation powers. (D) Difference of diffractograms from the QR sample being held at different temperatures by a heating jet. Temperatures were calibrated afterwards using a PT100 temperature sensor at the sample position.

increased with higher excitation powers. Moreover, the (002) reflection shifted to smaller angles giving a hint for thermal expansion of the corresponding crystal direction.Though, the absence of such a shift for the other two reflections is possible due to an effect of insufficient resolution as a consequence of the low ratio of peak shift and width.

To classify these findings, we have conducted the same experiment with a heating jet instead of the laser making possible a comparison of the laser with the heat impact on the QRs. The difference of diffractograms from the QR sample being held at different temperatures by the heating jet is displayed in Figure 2D. In contrast to the measurements involving optical excitation, every reflection dropped in intensity on heating the sample. However, the shift of the (002) reflection was as well observable. Hence, the increase in intensity of the (002) reflection in optically excited state remains to be clarified.

The upcoming analysis of the data including evaluating the peak widths and shifts will provide a more precisely insight into these results.

Acknowledgment. The DELTA staff is gratefully acknowledged for providing synchrotron radiation. S. T. thanks the NRW Forschungsschule 'Forschung mit Synchrotronstrahlung in den Nano- und Biowissenschaften' for financial support.

References

[1] P. Borri, W. Langbein, S. Schneider, U. Woggon, R.L. Sellin, D. Ouyang, and D. Bimberg, *Phys. Rev. Lett.* **87**, 157401 (2001). [2] P. Borri, W. Langbein, U. Woggon, M. Schwab, M. Bayer, S. Fafard, Z. Wasilewski, and P. Hawrylak, *Phys. Rev. Lett.* **91**, 267401 (2003). [3] C.-K. Sun, J.-C. Liang, and X.-Y. Yu, *Phys. Rev. Lett.* **84**, 179 (2000). [4] L. Besombes, K. Kheng, L. Marsal, and H. Mariette, *Phys. Rev. B* **63**, 155307 (2001). [5] D. V. Talapin, R. Koeppe, S. Gotzinger, A. Kornowski, J. M. Lupton, A. L. Rogach, O. Benson,J. Feldmann, and H. Weller, *Nano Lett.* **3**, 1677 (2003).

Pressure dependent structure of silkworm silk fibroin nanocrystals

Christina Krywka [1], Florian Kunze [1], Christian Sternemann [2] and Martin Müller [3]

[1] Institut für Experiementelle und Angewandte Physik, Christian-Albrechts-Universität Kiel, Leibnizstraße 19, D-24098 Kiel
[2] DELTA, Technische Universiät Dortmund, Maria-Goeppert-Mayer Straße 2, D-44227 Dortmund
[3] Helmholtz Zentrum Geesthacht, Max-Planck-Straße 1, D-21502 Geesthacht

Natural silks exhibit extraordinary mechanical properties, as they combine high tensile strength with a high elongation at failure. Due to their remarkable mechanical properties and potential medical applications the ability to synthesize silk has been longed for by many fields of industry up to date. However, the nanoscopic structure of silk is still a matter of debate and none of the efforts to synthesize silk so far have led to fibres with comparable mechanical properties as the bio-spun fibres. The toughest silk known is spun by spiders. However, it has recently been shown that, chemically and rheologically closely related, silkworm silk (*Bombyx Mori*) could reach comparable parameters in an optimised spinning process [1]. Silkworm silk's major constitutent is fibroin, a protein rich in repetitive alanine and glycine sequences. Generally speaking, silkworm silk consists of a soft, more or less amorphous matrix into which β-sheet polyalanine nanocrystals are embedded [2], whose unit cell c-axis shows a high degree of orientation along the fibre axis. The mechanical models of silk available today do not satisfactorily connect nanoscopic structure and macroscopic properties. For example, the supposed high rigidity of the nanocrystals in the cross-linked rubber model [3] has been questioned by X-ray diffraction results [4]. In other models [5,6] the deformation processes in the crystals and the disordered regions are neglected. Our aim is to establish a model for silk incorporating the macroscopic mechanical behaviour for both tensile stress as well as compressive stress on the basis of its semicrystalline morphology.

To study the influence of the amorphous matrix on the mechanical properties and the way the nanocrystals are interconnected it is beneficial if undirected stress or pressure is used rather than tensile stress. That way crystal and external stress are equal, regardless of the details of the nanostructure. This demand, however, has not been met experimentally before. Existing studies on mechanical properties of silks employed mainly tensile tests methods where the fibers were only exposed to directed, uniaxial stress. There have been only few attempts to employ pressure [11,12]. None of them, however, investigated native silk samples but only silk fibroin solutions. To close this gap Wide Angle X-ray Scattering (WAXS) with *in situ* pressurization using hydrostatic pressure of up to 5 kbar (0.5 GPa) was performed as a proof-of-principle study at BL9 of DELTA, studying in this way the polyalanine nanocrystal stability and strength with no preferential force direction. Exemplary data is shown in figure 1.

The results show that as the β-sheet planes are aligned mostly parallel to the fibre axis, the crystallites are mostly squeezed perpendicular to the fiber axis when pressure is applied, i.e. in the direction of the H-bonds between the beta-sheets. From the pressure dependence of the detected shifts (see examples in fig.2), the modulus of compression can be determined for the affected unit cell axis. The results from the recorded data are compared to our results previously derived from tensile tests [7] and more detailed results, derived from subsequent high-pressure studies at the ESRF are also presented.

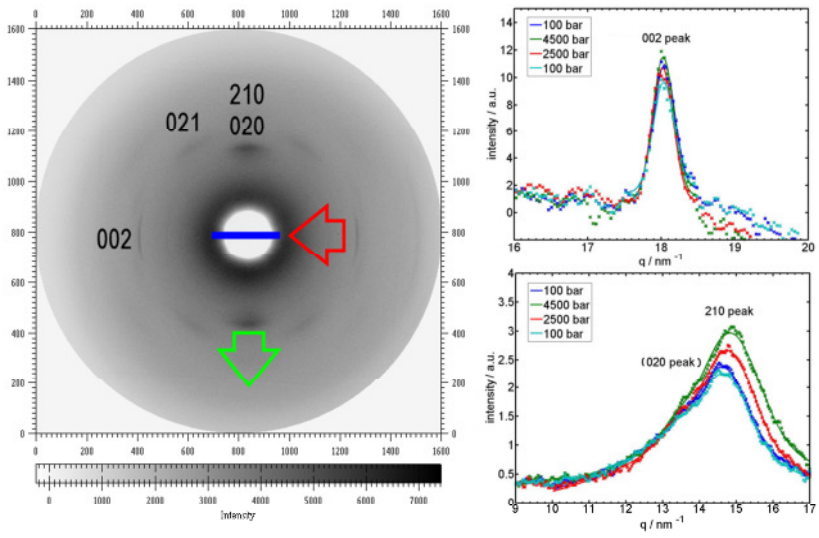

Fig. 1: Typical WAXS scattering pattern recorded at BL9 of DELTA from a bunch of silk fibres, the fibre direction indicated in blue. The red and green arrows indicate the shifts of the (002) and (210)/(020) reflections as the fibre is exposed to tensile stress and undirected hydrostatic pressure, respectively. Right: radially integrated sections showing the pressure dependence of both peaks for the case of hydrostatic pressure. The data was fitted using a sum of two and three Gaussians, respectively (solid lines).

Experimental method

To investigate the nanoscopic, pressure induced crystallite deformation and to be able to compare the results with tensile tests a pressure of several kbar was required. Unlike spider silk, which exhibits a dramatic change in morphology when exposed to water (known as supercontraction) in the case of silkworm silk no such effect occurs. Furthermore, we could show previously that water from the surrounding, humid gas phase is only incorporated into the amorphous phase and does not penetrate the crystallites [8,9]. This enabled us to employ a homebuilt hydrostatic pressure cell [10] using water as the pressurizing medium and to perform SAXS and WAXS measurements on silkworm silk in the desired pressure regime, i.e. with *in-situ* hydrostatic pressurization. SAXS measurements were performed at an incident photon energy of 10 keV and WAXS data was recorded at 27 keV in order to account for the relatively small acceptance cone of the used sample cell.

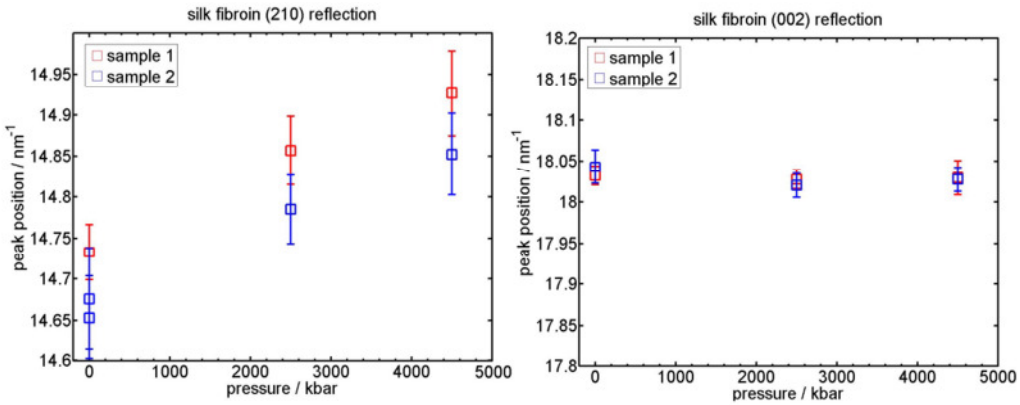

Fig. 2: Pressure dependence of the positions of the equatorial (210) and the meridional (002) reflection of silkworm silk fibroin nanocrystallites. For a better comparison the interval shown on the peak position axis is same size for both plots.

While the SAXS data exposed no significant pressure dependence and by this indicated a high stability of the tertiary structure of the fibroin protein against pressure induced denaturation we also succeeded in recording some isolated data in WAXS geometry. Although the WAXS part of the experiment was intended to be a proof-of-principle only, it generated a surprising finding: as indicated by the green arrow in figure 1 the observed pressure induced observed peak shift indicates a deformation of the crystallites that is also anisotropic – as in the case of tensile strain – but with a different unit cell axis being involved.

Acknowledgements

The authors thank the DELTA team for great support and providing the beam. Thanks go out also to the group of Prof. Winter for providing parts of the high-pressure experimental equipment. This project was supported within the framework of the BMBF (Federal Ministry of Education and Research) project 05KS7FK1.

References

[1] Z. Shao et al. *Nature* **418**, 741 (2002)
[2] Y. Shen et al. *Macromolecules* **31**, 8857 (1998)
[3] Y. Termonia. *Macromolecules* **27**, 7378 (1994)
[4] A. Sinsawat et al. *Polymer* **43**, 1323 (2002)
[5] D. Porter et al. *Eur.Phys. J. E* **16**, 199 (2005)
[6] F. Vollrath et al. *Appl.Phys. A* **82**, 205 (2006)
[7] I. Krasnov et al. *Phys. Rev.Lett.***100**, 048104 (2008)
[8] M. Müller et al. *Macromolecules* **31**, 3953 (1998)
[9] T. Seydel et al. *Macromolecules* **40**, 1035 (2007)
[10] C. Krywka et al. *Chem. Phys. Chem.* **9**, 2809 (2008)
[11] R. Gebhardt et al. *Macromolecules* **41**, 9934 (2008)
[12] H. Peng et al. *J. Phys. Chem. B* **113**, 4636 (2009)

Correlation of the particle behavior, microstructure and phase evolution during the optimization of HVOF sprayed WC-12Co coatings by means of DoE

Wolfgang Tillmann[a], Leif Hagen[a], Ingor Baumann[a],
Metin Tolan[b], Michael Paulus[b], Florian Wieland[b]

[a] *Institute of Materials Engineering, Technische Universität Dortmund, 44221 Dortmund, Germany*
[b] *Fakultät Physik/DELTA, Technische Universität Dortmund, 44221 Dortmund, Germany*

Introduction

Thermally sprayed WC-Co coatings are widely used for the wear protection of mechanical, aeronautic, and naval applications. They are commonly deposited by means of the High Velocity Oxy-Fuel Flame spraying technique (HVOF). The high process gas velocities and the corresponding short dwell time of the spray particles passing the supersonic flame do not only provide well-adhering coatings but also reduces the amount of undesired phases (Ref. 1, 6).
In order to optimize the process parameter settings statistical designs of experiments were used. Interactions between the process parameters provide a fundamental understanding about the complex relationships between the thermo-kinetic in-flight particle behavior, the microstructure formation and the phase evolution during the spray process. This knowledge is however necessary not only to develop wear resistant coatings with optimized mechanical and tribological properties, but also to meet economic demands with regard to the HVOF process.
The aim of the present research work is to study the effects of different spray parameter settings on the development of WC-12 coatings. A major focus is thereby placed on the correlation of the in-flight particle behavior (temperature, velocity and size), process characteristics (HVOF chamber pressure and process energy) and the phase evolution to achieve a fundamental understanding of the majorly important mechanisms during the manufacturing of WC-Co coatings. The phase development of the feedstock and the coatings was analyzed at the Beamline 9 of the DELTA, Dortmund, Germany using a photon energy of 27 keV (Ref. 2).

Experiments

Rectangular (70 mm x 50 mm x 10 mm) C45 steel specimens (1.0503) were employed as substrate material for thermal spray experiments. Commercially available agglomerated and sintered WC-12Co powder (Sulzer Metco AG, Switzerland) was used as feedstock material. The particle size was measured by static laser light scattering with a S3500 particle analyzer (Microtrac, USA). Figure 1 shows the grain size distribution and a SEM image of the powder morphology.

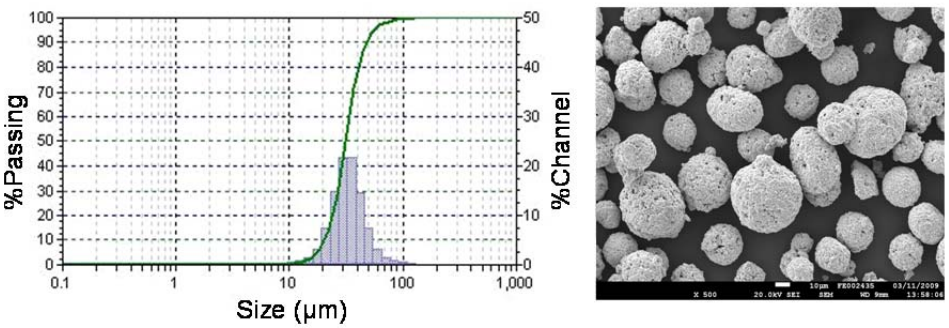

Figure 1: Right: Structure of the WC-12Co powder taken by SEM microscope; Left: powder grain size distribution analysis.

The WC-12Co powders feature a particle size distribution from 20.63 to 47.24 µm. An average size of 31.13 µm was determined. The temperature and the velocity of the particles were measured in-flight with Accuraspray-g3 device (Tecnar, Canada). A CJS-HVOF gun (Ther-

mico GmbH & Co KG, Germany) with K5.2 combustion chamber design was used to conduct the coating experiments. This liquid fuel HVOF system uses an EXXSOL D 60 kerosene (ExxonMobil Chemical Central Europe GmbH, Germany), hydrogen and oxygen as combustion media. A further description of the System is given else-where (Ref. 3 - 5).

Results

In terms of optimized parameter settings the experiments carried out that kerosene, oxygen and the stand-off distance of the spray gun are the most significant factors. Depending on these adjustable factors the spray particles are supplied with more or less kinetic and thermal energy at the point of impact on the substrate. While keeping the oxygen level constant experiments with different kerosene levels show the significant influence of the Oxy/Fuel Ratio (OFR) on the spray conditions as shown in Figure 2.

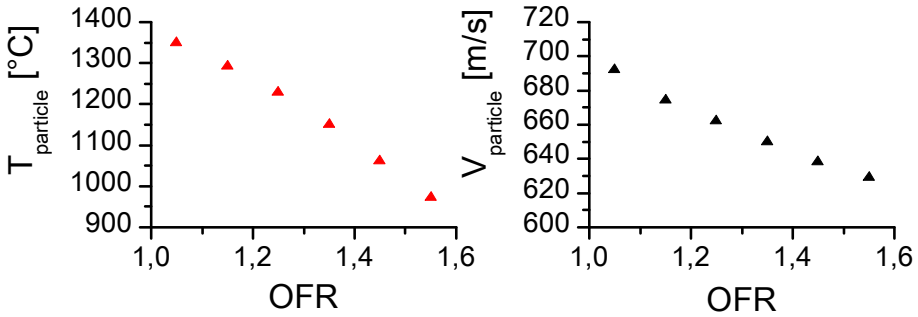

Figure 2: Inflight spray conditions depending on the stoichiometric relations (OFR: Oxy Fuel Ratio).

At a constant oxygen level an increase of the kerosene level with a stoichiometric OFR reaches 1 (HL = 90 l/min = const.) yields in distinctly higher particle velocities, higher temperature and a better molten state of the particle. In terms to these mentioned correlations, experiments with a stoichiometric OFR lead to a combustion chamber pressure of 13.5 bar at a measured thermal energy of 96 KW transferred to the coolant. By means of decreased kerosene levels and an OFR of 1.55 the experiments show a decreased combustion chamber pressure of 12.3 bar and less thermal energy of 71 KW.

Low kerosene levels generate a HVOF flame with lower thermal energy in order to prevent overheating of the feedstock material or to reduce the risk of phase transformation in terms of decarburization. In avoidance of brittle ternary phases of the system W-Co-C during spraying, different spray parameter settings were optimized. With regards to high energetic spray conditions selected samples were investigated by using synchrotron radiation source.

It can be summarized, that the agglomerated and sintered -45 + 15 µm WC-Co feedstock material still allow high energetic spray conditions. WC-Co powders contain a mixture of crystalline WC and Co phases without any non WC-Co Phases. In contrast, the WC-Co coatings show W_2C, W in addition to WC and Co phases and a ternary carbide (η) phases like Co_3W_3C. In terms of high energetic spray conditions the example is given by the phase analysis of high and low spray particle temperature shown in figure 3. With regards to the HVOF sprayed WC-Co coatings, the experiments show marginal phase transformations caused by decarburization. Carbon reacts with atmospheric oxygen. This reduction of carbon yields in a W_2C decomposition. Subsequently, elementary tungsten will dissolve in the liquid Co matrix while oxidation of C. Beside elementary tungsten a ternary carbide phase of Co_3W_3C is formed. The dissolution process is enhanced by the presence of oxygen. This phase transformation occurs as the powder particles traverse from the gun exit to the substrate until they are covered by new smashed splats. While WC-Co particles are injected into the hot flame, the particles reach temperatures up to 1750°C and high velocities of up to 750 m/s. Due to the spray conditions the particles are molten or partially molten. In situ particle diagnostic shows that under the spray conditions the particle temperature for the particle size -45 + 15

µm is below the WC peritectic decomposition temperature (2785°C). Therefore, this mechanism is not a dominant factor.

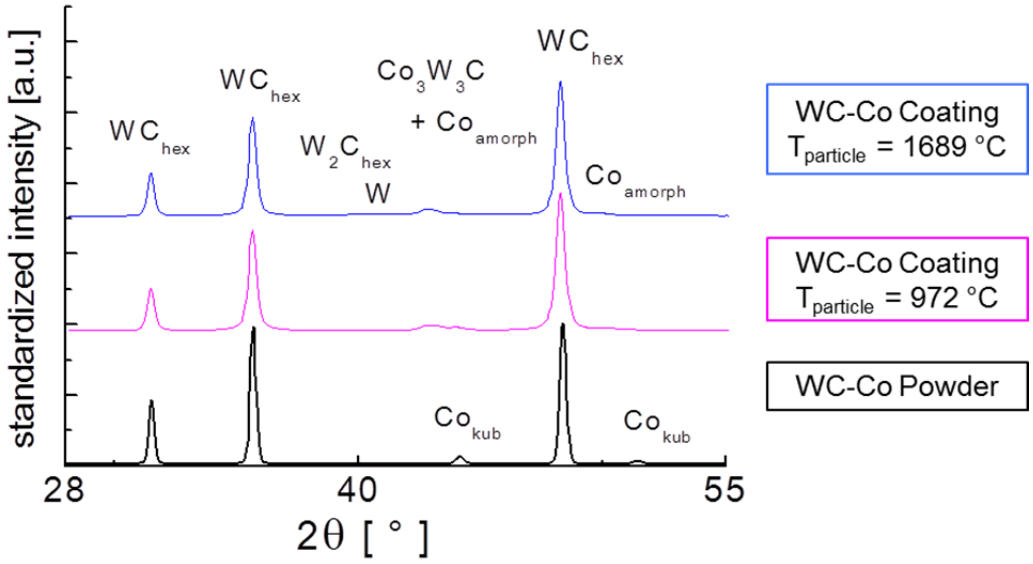

Figure 3: Diffraction patterns of coatings and WC-12Co powder feedstock material. 2-theta is scaled regarding to a photon energy of 8 keV.

Acknowledge

The authors gratefully acknowledge the financial support of the DFG (German Science Foundation) within the Collaborative Research Centre SFB 708 A2. We like to thank the DELTA machine group for providing synchrotron radiation and for technical support. We also would like to thank Prof. M. Tolan, Dr. M. Paulus and F. Wieland for their help and support during the test experiments carried out at Beamline 9 of the DELTA.

Literature

1. C. Bartulli, T. Valente, F. Cipri, E. Bemporad, M. Tului, Parametric study of an HVOF process for the deposition of nanostructured WC-Co coatings, J. Therm. Spray Technol., 2005, 14 (2), p 187-195

2. C. Krywka, M. Paulus, C. Sternemann, M. Volmer, A. Remhof, G. Nowak, A. Nefedov, B. Pöter, M. Spiegel, M. Tolan, Journal of Synchrotron Radiation, 2006, 13, 8-13

3. G. Matthaeus and A. Sturgeon, Application of the HVOF Process to Internal Coatings of Cylinders, and Hard-and Software for the Internal Coating of Complex Components, 7th HVOF Spraying Colloquium, Nov 9-10 2006, Germany, GTS e.V., 2006, p 199-205

4. G. Matthaeus and G. Stevens, New HVOF Equipment and Technology for the Use of Superfine Powders—10 lm and Internal Coating Applications, 6th HVOF Spraying Colloquium, Nov 27-28 2003 (Germany), GTS e.V., 2003, p 167-176

5. G. Matthaeus, M. Kostecki, and O. Dau, The Fully Automatic, Computer Controlled C-CJS (Computerised Carbide Jet System) HVOF System with 25 bar Combustion-Chamber pressure by Thermico, 5th Colloquium on HVOF Flame Spraying, Nov 16-17 2000, Germany, GTS e.V., 2000, p 147-158

6. W. Tillmann, E. Vogli, I. Baumann, G. Matthaeus, T. Ostrowski, Influence of the HVOF Gas Composition on the Thermal Spraying of WC-Co Submicron Powders (−8 + 1 µm) to Produce Superfine Structured Cermet Coatings, J. Therm. Spray Technol., 2008, 17 (5-6), p 924-93

Probing the interaction potential of proteins in solution

Johannes Möller*,[a], Martin A. Schroer[a], Mirko Erlkamp[b], Sebastian Grobelny[b], Michael Paulus[a], Metin Tolan[a], and Roland Winter[b]

[a] *Fakultät Physik/DELTA, TU Dortmund, Otto-Hahn-Str. 4, D-44227 Dortmund, Germany;*

[b] *Physikalische Chemie I, Fakultät Chemie, TU Dortmund, Otto-Hahn-Str. 6 , D-44227 Dortmund, Germany*

*email: johannes.moeller@tu-dortmund.de

The present work was dedicated to investigate the combined influence of pressure and salt (electrostatic screening) on the interaction potential of proteins. The fabrication of high quality protein crystals suitable for determine the atomic structure by X-ray diffraction is up to know still a challenging task due to the many parameters involved like pH, temperature, pressure, crystallization agent and its concentration, and protein concentration [1]. Therefore, the search for good crystallization conditions is usually made by a trial and error routine, which means the empirical screening through a large field of parameters sets until good crystals are obtained. Here, a more precise knowledge about the interaction between proteins in solution can help to predetermine possible crystallization conditions [2, 3], which is even more important when only a small amount of protein is available.

The interaction potentials were investigated by small angle X-ray scattering (SAXS) experiments, which were performed at beamline BL9 of DELTA and beamline BW4 at HASYLAB, Hamburg. The experiments at beamline BL9 of DELTA used the SAXS setup already described in Ref. [4]. A photon energy of 10 keV and a sample-to-detector distance of about 1335 mm allowed to cover a q-range from 0.2 up to 3.5 nm^{-1}. The exposure time was chosen to be 1200 s, with temperatures between 8 - 45 °C and pressures from 1 - 4000 bar. The used protein lysozyme (14.3 kDa, pI = 11) was dissolved in 25 mM bis-Tris buffer solution at pH 7 in concentrations between 5 - 20 wt %.

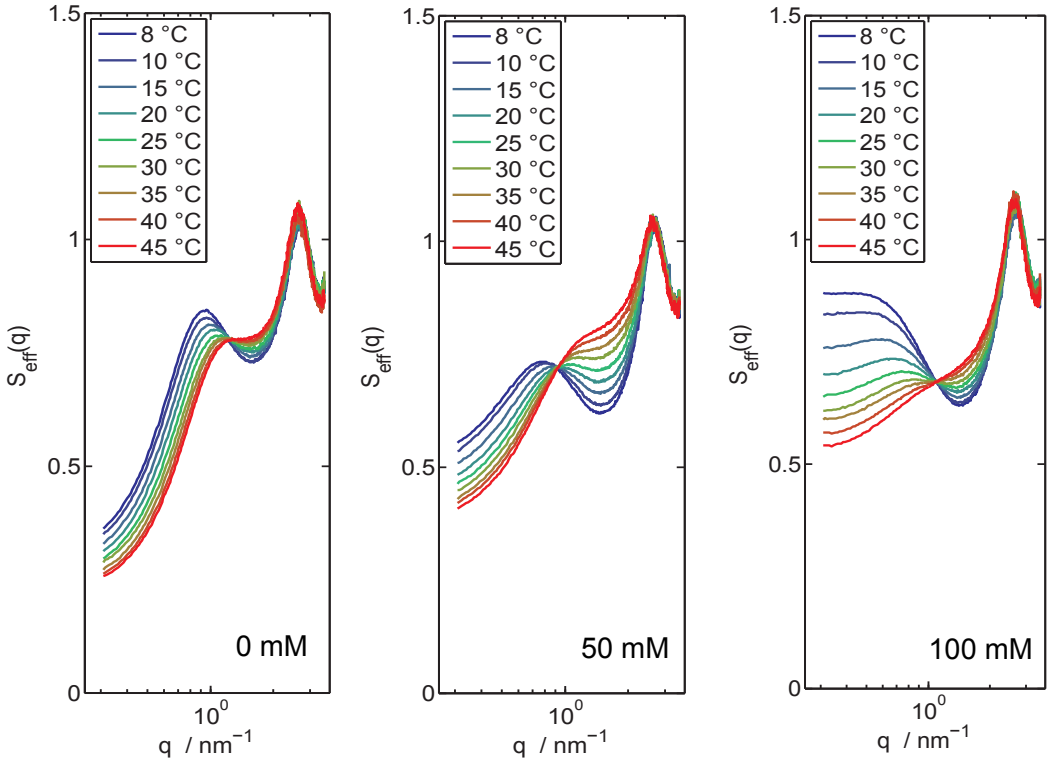

Figure 1: The effective structure factor under the influence of NaCl concentration (0 mM, 50 mM, 100 mM) and temperature.

The scattering intensity from diluted protein solution can be described by the form factor $P(q)$ with $q = (2\pi/\lambda)\sin(\Theta/2)$ being the wave vector transfer. For lysozyme in solution, the form factor can be described sufficiently by that of an ellipsoid of revolution. For solutions with higher protein concentration, an additional

scattering contribution can be observed, which is originated from the interaction of the particles. The resulting SAXS signal can be described in the decoupling approximation as product of the form factor and an effective structure factor, i.e. $P(q) \cdot S_{eff}(q)$. By measuring SAXS pattern at different protein concentrations, the effective structure factor of the proteins in solution can be determined from the scattering data. The effective structure factor for 10 wt % lysozyme is shown in figure 1. The increasing attractive interaction with enhanced NaCl concentration can be seen due to the increasing effective structure factor at low q-values.

In order to quantitatively investigate the protein interactions, the structure factor can be calculated in the mean spherical approximation, using a DLVO (Derjaguin-Landau-Verwey-Overbeck) potential consisting of a hard sphere, a repulsive screened Coulomb, and an attractive potential, which is modeled as a Yukawa potential. By refining this model to the measured data, the strength of the attractive interaction and therefore the interaction potential of the proteins can be calculated [5, 6].

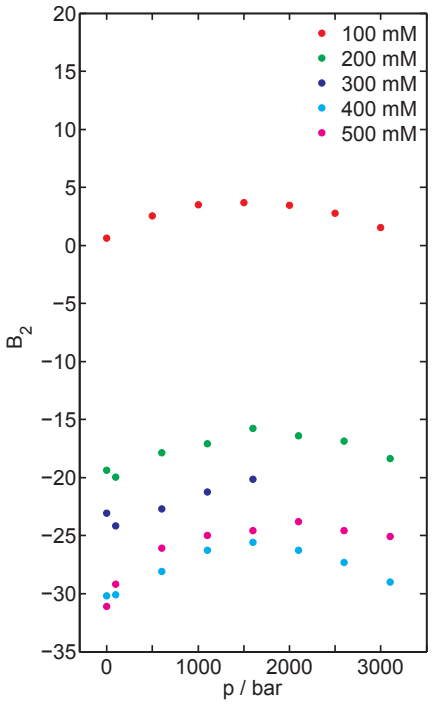

Figure 2: Second virial coefficient B_2 as a function of pressure and salt concentration for 10 wt% Lysozyme at $T = 25$ C.

The second virial coefficient B_2 was found to be a good criterion, if the crystallization condition is suitable to form high quality crystals. It is calculated from the interaction potential as

$$B_2 = 2\pi \int_0^\infty (1 - \exp(-(U(r)/k_B T))r^2 dr, \qquad (1)$$

with $U(r)$ being the interaction potential and T the temperature. In figure 2, the measured values for B_2 are shown at different pressures and salt concentrations. It can be seen, that with increasing salt concentration the second virial coefficient is decreasing as the repulsive Coulomb potential is screened and the attractive forces prevail. Additionally, a pressure dependence of the interaction potential can be observed, which shows a maximum around 1500-2000 bar and is not influenced by the salt concentration. Further measurements at different temperatures and protein concentrations were also performed. With this, the interaction potential of lysozyme in solution was determined in a wide parameter range, giving the possibility to influence the interactions in a desired way.

The authors like to acknowledge the DELTA machine group for providing synchrotron radiation and technical support.

References

[1] J. Wanke, W. Peukert, *Chem. Eng. Technol.* **34**, 4, 510-516 (2011).

[2] R. A. Curtis, L. Lue, *Chem. Eng. Scien.* **61**, 907-923 (2006).

[3] N. Asherie, *Methods* **34**, 266-272 (2004).

[4] C. Krywka, C. Sternemann, M. Paulus, N. Javid, R. Winter, A. Al-Sawalmih, S.B. Yi, D. Raabe, M. Tolan, *J. Synchrotron Rad.* **14**, 244 (2007).

[5] M. A. Schroer, J. Markgraf, D. C. F. Wieland, C. J. Sahle, J. Möller, M. Paulus, M. Tolan, R. Winter, *Phys. Rev. Lett.* **106**, 178102 (2011).

[6] M. A. Schroer, Y. Zhai, D. C. F. Wieland, C. J. Sahle, J. Nase, M. Paulus, M. Tolan, R. Winter, *Angew. Chem. Int. Ed.* **50**, 1-5 (2011).

Verification of carbide-nitride transformation in a cold work tool steel powder by means of synchrotron radiation

K. Zumsande[1,2*], N. Krasokha[2], S. Huth[2], S. Weber[1], W. Theisen[2]
[1]) Helmholtz Zentrum Berlin für Materialien und Energie, Hahn-Meitner-Platz 1, 14109 Berlin, Germany
[2]) Chair of Materials Technology, Ruhr-Universität Bochum, Universitätsstraße 150, 44801 Bochum, Germany
* Tel.: 0049 231 32 25962, Fax: 0049 231 32 14104, e-mail-address: zumsande@wtech.rub.de

Introduction

Tool steels are applied for materials processing like primary forming, forming or cutting processes. Therefore, they suffer high mechanical stresses and are exposed to corrosive attack. For processing at ambient temperatures cold work tool steels are applied. Those steels are classified depending on their carbon and therewith carbide content [1]. Carbides increase the resistance of the material against abrasion but may impair the mechanical properties of the material negatively, for instance if they have large dimensions. Thus, the amount, the distribution, the chemical composition and the size of the carbides have to be adjusted to the operation requirements. The investigated cold work tool steel X230CrVMo13-4 is classified to the high carbon steels. While a casting process leads to the formation of large carbides inside this material, the production by powder metallurgy (PM) results in a high but finely dispersed volume fraction of carbides and thus an improvement of mechanical properties of the resulting product. The production by PM is well understood and successfully applied. But due to the low sintering ability of gas atomized high alloyed steel powders (as the investigated steel) the PM production features challenges and it is necessary to use high temperatures and high pressures applying hot isostatic pressing. An alternative is the Super Solidus Liquid Phase Sintering (SLPS) where the material is heated up between solidus and liquidus temperature. By realizing a liquid fraction of ~30 % [2] full density is reached in short time without a significant coarsening of the microstructure. Since this process does not require an encapsulation, the material can interact with the ambient atmosphere. The investigated steel features high nitrogen solubility and therefore nitrogen uptake is expected if sintering takes place under nitrogen atmosphere leading to a change of chemical and phase composition [3-7].

This study deals with the microstructural evolution of the cold work tool steel X230CrVMo13-4 during a sintering cycle under consideration of the gas-solid interaction. Two effects are of interest. On the one hand the gas atomized powder is not in equilibrium state and thus is supposed to undergo changes in the phase composition as soon as diffusion is enabled and secondly the uptake of nitrogen at elevated temperatures will provoke an alteration of chemical composition of the phases. In case of the investigated steel a transformation from vanadium rich carbide (VC) into vanadium rich nitride (VN) is expected since VN is thermodynamically more stable than VC. This leads to an increase of carbon in the surrounding matrix material (VC+N→V(C,N)+C) [3,5,7]. This enrichment in carbon results in a decrease of solidus temperature and therewith reduces energy consumption and costs of the sintering cycle.

Experimental

Prior to the synchrotron study a heat treatment of the powder material was performed with a continuous heating rate of 10 K/min to different temperatures under both, helium (1 bar) and nitrogen (0.3 bar) condition. The holding time was set to 5 minutes followed by a rapid cooling by Argon gas in order to “freeze” the microstructure. The treatment took place at a Bähr DIL805 dilatometer which uses induction as heating source. The powder was heat treated indirectly through a ferritic capsule which was open to the atmosphere. Thus, the temperature of the powder material remained lower than the capsule. The corresponding temperatures can be extracted from Table 1.

The microstructural evolution was investigated at the Beamline 9 at DELTA (Dortmund, Germany) in reflection mode. All samples were still in powder state after heat treatment except sample 1200/N_2. The powder material was filled into glassy capillars and measured by means of the monochromatic synchrotron radiation while they are turned along the vertical axis in order to avoid influence of texture in the material. The slightly compacted sample (1200/N_2) was cut, ground and scanned in reflection mode.

Table1: Overview of set temperatures and the actual temperatures during heat treatment of the investigated powder material and the respective sample names. The heat treatment was performed under He and N_2 atmosphere.

	1 bar He		0.3 bar N_2	
Set temperature T_{set} [°C]	Actual temperature [°C]	Sample name	Actual temperature [°C]	Sample name
As atomized (RT)	-	X230	-	X230
600	525	600/He	560	600/N_2
800	749	800/He	735	800/N_2
1000	925	1000/He	929	1000/N_2
1200	1123	1200/He	1121	1200/N_2

Results and Discussion

The spectra reveal that the steel in initial state consists of an austenitic matrix (γ) which has a cubic face centered (fcc) structure with a small amount of martensite (α') which is a tetragonally distorded body centered cubic (bct) structure. Additionally, the presence of vanadium rich monocarbide (MC, M=metallic atoms) and chromium rich carbide (M_7C_3) can be detected in the scan. The fcc structure of the mainly austenitic matrix is caused by the high dissolved carbon content which inhibits the transformation from the high temperature fcc-phase into the low-temperature bcc-phase of the iron during rapid cooling. Therefore, the steel is not in equilibrium condition and thus expected to approach the equilibrium state with increasing temperature. On Figure 1 it can be seen that at a heat treatment at T_{set}=800 °C the matrix is transformed into the equilibrium bcc-phase (α). This transformation takes place due to carbide precipitation at elevated temperatures ($M_{23}C_6$, M_7C_3) resulting in a decrease of carbon in the matrix leading to a complete fcc-bcc transformation. Thus, the matrix remained body centered cubic even after quenching. At T_s=1000 °C the matrix is known to be transformed into fcc-austenite during heating, since the austenising temperature (~830 °C) is extended. Due to the rapid cool down and the moderate carbon content, the fcc-matrix transforms into bct-martensite (α') during quenching which explains the high bcc/bct-signal as to be seen on Figure 1.

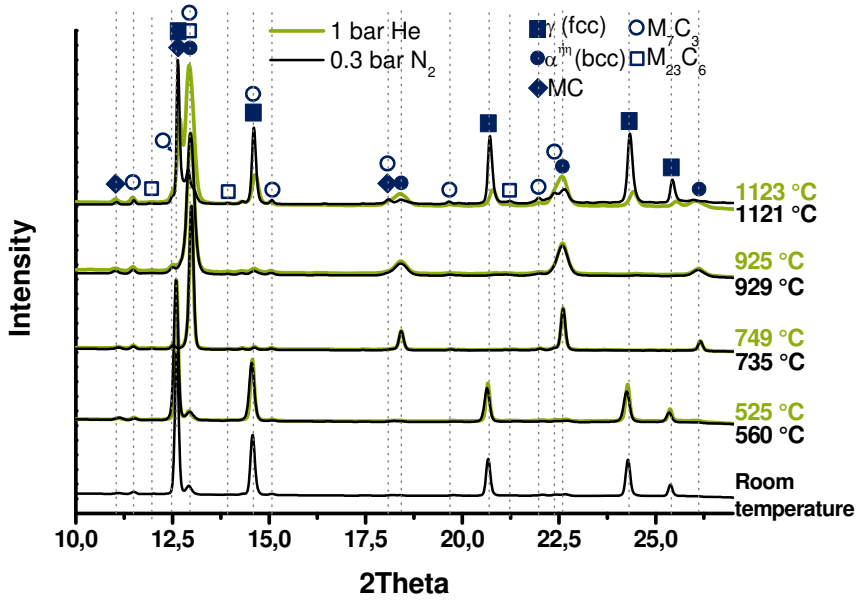

Figure 1: Overview of the obtained diffractograms

At all shown temperatures no evident difference between the phase compositions depending on the atmosphere can be detected expect the highest investigated temperature. The slightly broader reflections of the sample 1200/N_2 can be explained by the bulk state of the sample. However, even though the sample temperature of 1200N_2 and 1200/He differ only by 2 °C (the $T_{8/5}$ time varies only by 2 seconds), the composition of the matrix of 1200/N_2 has a distinct higher amount of retained austenite whereas the matrix of

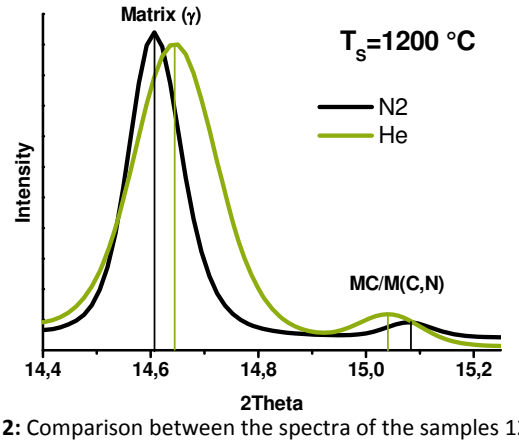

Figure 2: Comparison between the spectra of the samples 1200/N_2 and 1200/He showing a shift of peak position

1200/He is mainly martensitic. As mentioned, the amount of retained austenite is dependent on the dissolved carbon content in the matrix before quenching. Thus, at this elevated temperature the carbon content of the matrix is expected to be significantly higher when heat treatment takes place under nitrogen. This difference can be a result of various effects. The carbon content of the matrix can be affected by dissolution of carbides at elevated temperatures. However, since the actual temperatures do not vary, the amount of decomposed carbides is expected to be the same in both samples independent from the atmosphere. It has also been considered that a carbon loss of the matrix can be a result of carbothermal reduction of oxides at elevated temperatures. The most likely explanation, however, is that the carbon content of the matrix is enriched due to the transformation of the monocarbide into carbonitrides resulting in a release of carbon into the matrix if sintering takes place under nitrogen atmosphere. To verify this assumption a comparison between the samples heat treated to T_s=1200 °C is shown in Figure 2.

The range of 2Theta is chosen, since it allows a closer look on the position of one reflection related to both phases, the austenitic phase and the monocarbide/carbonitride phase. The position of the reflection on the *2 θ* scale is related to the lattice spacing *d* and therewith to the lattice constant *a* as can be seen by the Bragg Equation.

$$\frac{2\sin\theta}{\lambda} = \frac{1}{d(hkl)} \quad \text{Eq. 1 [8]}$$

This equation reveals that as smaller the lattice constant gets as more the reflection angle shifts to higher values and vice versa. Figure 2 shows that the position of the reflection related to the MC/M(C,N) phase of 1200/N_2 is shifted to higher reflection angle compared to 1200/He. This is an indication for the transformation from MC to M(CN) as vanadium rich nitride features a lower lattice constant than vanadium rich carbide. As mentioned, this transformation is known to be accompanied by the release of carbon into the matrix. A lower peak position of the austenite phase of 1200/N_2 compared to 1200/He can be seen clearly in Figure 1. It indicates a carbon uptake of the matrix as the lattice constant increases if additional interstitial elements as carbon are dissolved and therefore confirms the expectation that carbon is released into the matrix.

Summary and Conclusion

To conclude, the nitrogen atmosphere is investigated to lead to a nitrogen uptake of the MC leading to a formation to M(CN) and to a release of carbon into the surrounding austenitic matrix. The shift of the positions of the reflections of the MX and austenite to higher and lower reflection angles, respectively, confirms this correlation. Additionally, the increased carbon content results in a higher amount of austenite after quenching as can be seen clearly in the synchrotron measurements. These results proof the distinct effect of the atmosphere on the chemical composition of the phases which results in an alteration of sintering behavior as well as it will lead to a decrease of solidus temperature.

Acknowledgement

This work was supported by the Deutsche Forschungsgemeinschaft within the project “Untersuchung des Flüssigphasensinterns vorlegierter Metallpulver auf Eisenbasis und dessen Beeinflussung durch Gas-Festkörperreaktionen“ (WE 4436/3-1 and TH 531/8-1). The authors gratefully acknowledge the TU Dortmund

for the opportunity to perform measurements at BL 9 at the electron storage ring DELTA. Thanks are due to the DELTA team, especially due to Dr. Sternemann, Dr. Paulus and Dipl. Phys. Steffen for their support.

Literature

[1] H. Berns, W. Theisen: *Eisenwerkstoffe – Stahl und Gusseisen. 3. Auflage.* Springer-Verlag Berlin Heidelberg 2006
[2] R.M. German: *Supersolidus Liquid Phase Sintering of prealloyed powders*. Metallurgical and Materials Transactions A28 (7), 1997, S. 1553-1567
[3] Aguirre I, Gimenez S, Talacchia S, Gómez-Acebo T, Iturriza I (1999) *Effect of nitrogen on supersolidus sintering of modified M35M high speed steel*. Powder Metallurgy, Volume 42, Number 4, pp. 353-357(5)
[4] Hill H, Weber S, Siebert S, Huth S, Theisen W (2010) *Comprehensive Investigations of the Supersolidus Liquid-Phase Sintering of Two Plastic Mold Steels*. Metallurgical and Materials Transactions A41 (2), S. 686-695
[5] Giménez S, Iturriza I (2003) *Study of the sintering behaviour of PM HSS under Nitrogen atmospheres: Application to alloy design*. Congreso Europeo de Metalurgia de Polvos, Valencia
[6] Weber S, Theisen W (2011) Critical *investigation of high temperature gas nitriding of a PM tool steel.* International Journal of Materials Research 102 1, pp. 17-24
[7] Zumsande K, Krasokha N, Huth S, Weber S, Theisen W (2011) *In-situ synchrotron study of a high alloyed cold work tool steel during heat treatment under nitrogen atmosphere*. Euro PM 2011 Proceedings
[8] Spieß L, Teichert G, Schwarzer R, Behnken H, Genzel C (2009) *Moderne Röntgenbeugung. Röntgendiffraktometrie für Materialwissenschaftler,* Physiker und Chemiker. 2. Auflage, Vieweg+Teubner, Wiesbaden

New beamline BL10

Konstantin Istomin[1], Anne Hüsecken[1], Stefan Balk[2], Ralph Wagner[2] and D.Lützenkirchen-Hecht[2]
[1]Universität Siegen [2]Universität Wuppertal

In cooperation with University of Wuppertal and Technical University of Dortmund, the solid state physics group of Siegen University has finished the construction of the new beamline BL10. The beamline is devoted to materials science research with the focus on X-ray diffraction and absorption spectroscopy measurements. Future experiments include:

1. Precise single crystal diffraction
2. Charge density studies
3. In-situ fatigue studies in metals
4. Transmission and fluorescence EXAFS measurements
5. Reflection mode EXAFS, making use of the diffractometer

A schematic lay-out of the beamline is shown in Fig. 1a (optics part) and Fig.1b (experimental part).

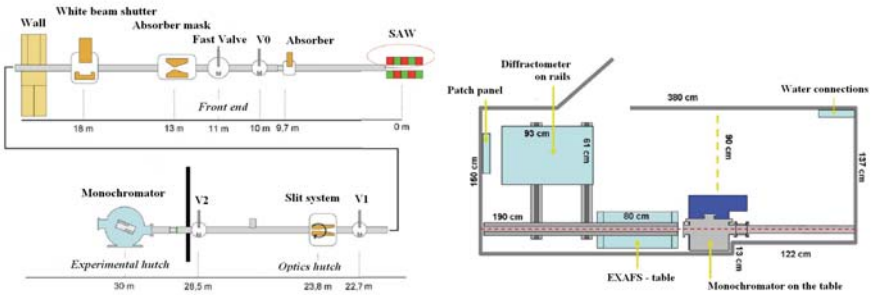

Fig.1 (a) BL10 Lay-out and main components (b) Experimental hutch (top-view).

The beamline has been officially inaugurated (See Fig.2, from the left) by Prof. Michael Scheffel (Prorector of University of Wuppertal), Prof. Holger Burckhart (Rector of University of Siegen), Prof. Ursula Gather (Rector of TU Dortmund), Prof. Ronald Frahm (University of Wuppertal), Prof. Ullrich Pietsch (University of Siegen) and Prof. Metin Tolan (DELTA chief and Prorector of TU Dortmund).

The current status of the BL10 is as follow: the first synchrotron light has been observed in the hutch (Fig.3). For this the old beryllium window needed to be replaced by a water-cooled beryllium window. The entire water cooling system of the beamline was re-arranged. After a major additional work the personal safety

interlock system and the vacuum control system have obtained clearance from Delta radiation safety team and have to be accepted by federal authorities in November 2011. Optimization work with the tilting absorber slit system is under way. A new filter inserter box is acquired and will be tested together with a set of monochromatic beam slits. Both fast avalanche photodiode and scintillation detectors are installed at the 4-circle Huber-diffractometer and ready for operation. Ionization chambers which will be used as detectors for EXAFS experiments and as monitors for diffraction experiments will be assembled shortly.

Fig. 2. Official inauguration of the beamline.

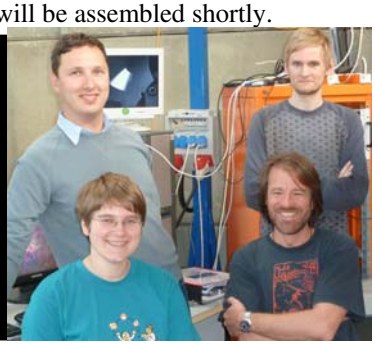

Fig. 3. BL10 team with the first beam on the monitor.

The beamline is expected to be fully operational from the beginning of 2012. The expected parameters of the beamline are summarized in Table 1.

Table 1. Parameters of BL10.

Parameter	Expected value	Note
Energy range	4 – 16 keV	
Energy resolution	dE/E ~ 1.6 x 10^{-4}	
Beam size	3 x 10 mm^2 to 0.5 x 0.1 mm^2	depending on aperture
Photon Flux	5 x 10^9 Photons / s mm^2	

Commissioning and first experiments at the PEEM at the TGM Beamline 12

C. Keutner[1,2,*], U. Berges[1,2], C. M. Schneider[3], C. Westphal[1,2]

[1] Experimentelle Physik I - Technische Universität Dortmund, Otto-Hahn-Str.4, D-44221 Dortmund
[2] DELTA - Technische Universität Dortmund, Maria-Goeppert-Mayer-Str. 2, D-44221 Dortmund
[3] PGI-6, Forschungszentrum Jülich, D-52425 Jülich
[*] corresponding author: christoph.keutner@tu-dortmund.de

(October 2011)

In this report we describe the commissioning of the photoemission electron microscope (PEEM) at BL 12 for operation with synchrotron radiation as well as first studies on magnetotactic bacteria.

In the last winter shutdown the deformed outlet-chamber of beamline 12 had to be replaced in order to provide synchrotron radiation at the beamline end-station. The PEEM reached a spatial resolution of $(0.5 \pm 0.1)\,\mu m$ (Figure 1) with synchrotron light excitation. This resolution differs from the best spatial resolution of $(0.22 \pm 0.02)\,\mu m$ obtained in threshold photoemission mode. The deviation in resolutions is no surprise, since many factors are limiting the resolution. For example, chromatic and spherical aberrations reduce the spatial resolution of a PEEM, and these two factors rely on the energy width of the emitted electrons [1].

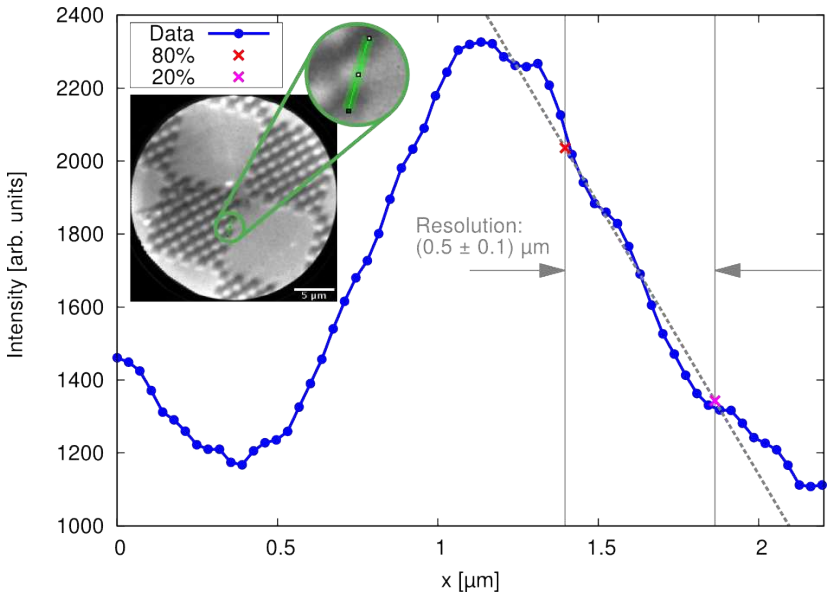

Figure 1: Resolution achieved by excitation with synchrotron radiation (right).

Additionally to the energy-dependent reducing factors in spatial resolution, two further effects strongly influence imaging properties; the first one is a heating-up effect of the beamline and the PEEM-endstation caused by the intense sun-light shining through the window nearby, which leads to a strong sample-drift under the PEEM-optics. Secondly, a blur during image recording induced by vibrations of the sample stage and beamline end-station additionally reduces the achievable spatial resolution. These vibrations occurring during normal DELTA-operation are reducing the resolution by at least 50% to $(0.34 \pm 0.07)\,\mu m$ in threshold photoemission mode, as test measurements showed. Therefore, as a first measure, additional

weights were attached to the girder of the end-station and some spare concrete blocks normally used as elements for the radiation wall were placed near the end-station. Subsequent vibration measurements proved the reduction of all vibrations at the PEEM end-station.

After commissioning first experiments recording images of magnetotactic bacteria were conducted. This group of bacteria contains a chain of magnetic particles, the so-called magnetosmome chain [2] for sensing earth's magnetic field. In order to prepare these bacteria in an UHV compatible way, some magnetotactic bacteria of the species *Magnetospirillum magnetotacticum* [3] were lyophilised and deposited on a silicon wafer. With this preparation method the first PEEM-images of *Magnetospirillum magnetotacticum* were obtained with threshold photoemission (Figure 2) and with excitation with synchrotron radiation.

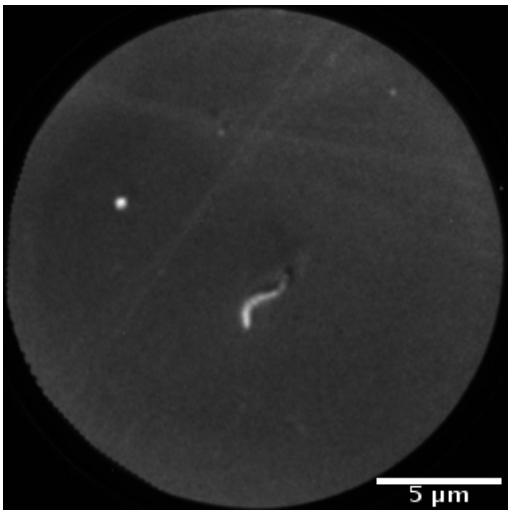

Figure 2: PEEM-image of *Magnetospirillum magnetotacticum*.

The further scientific goal is the study of a single magnetosome chain in a single bacterium. Up to now images of complete bacteria without any finer sub-structure were recorded, and especially its magnetosomes could not be resolved due to insufficient resolution. In order to achieve a higher spatial resolution, rather high voltage settings for the PEEM's electrostatic lenses have to be chosen, which is not possible in the present set-up. Therefore, the PEEM was sent for an upgrade to the manufacturer.

Acknowledgement

We would like to thank S. Doering as well as the DELTA-staff for their support.

References

[1] B. Heitkamp, Berichte des Forschungszentrums Jülich **Jul-4068** (2003).
[2] D. L. Balkwill, D. Maratea und R. P. Blakemore, J. Bacteriol. **141**, 1399 (1980).
[3] R. Blakemore, Science **190**, 377 (1975).

Investigation of the three layer system MgO/Fe/GaAs(001)

D. Handschak[1], F. Schönbohm[1,2], T. Lühr[1], S. Döring[2], D. Weier[1], C. Keutner[1,2], U. Berges[2] and C. Westphal[1,2]

[1]Experimentelle Physik 1 - Technische Universität Dortmund Otto-Hahn-Str. 4, D-44221 Dortmund, Germany
[2]DELTA - Technische Universität Dortmund, Maria-Goeppert-Mayer-Str. 2, D-44221 Dortmund, Germany

7th November 2011

We report a synchrotron high-resolution x-ray photoemission (XPS) and photoelectron diffraction (XPD) study of the three layer system MgO/Fe/GaAs(001). The interface of Fe/GaAs is interesting because it is a semiconductor-ferromagnetic junction. Therefore, it is possible to inject spins directly from iron to gallium arsenide. This is a part of research to spin-based communication, the so-called spintronics. Magnesium oxide is a very efficient insulator which is used especially in TMR-components (tunnel magnetoresistance). Both interfaces have a strong influence on the efficiency of the contributing effects. In this work we can clearify the structure of each layer.

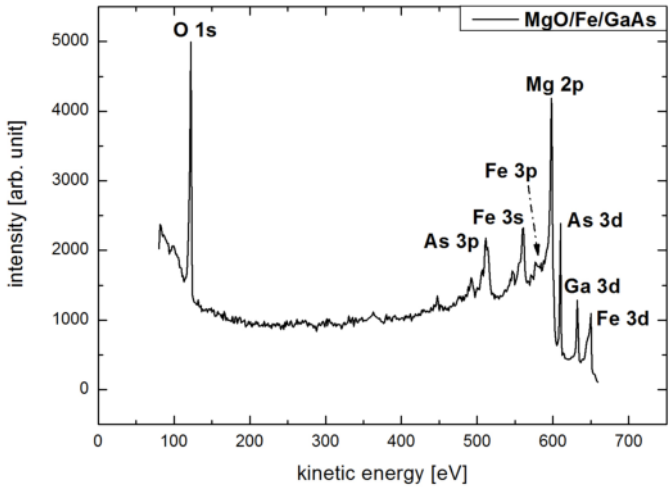

Figure 1: The survey scan of the prepared three layer system with an exitation energy of $h\nu = 650\,\mathrm{eV}$.

A reconstructed GaAs surface was used as a substrate for the foreseen studies on the three layer system. Core level spectra of As 3d and Ga 3d prove a successful preparation of the gallium rich (4×2)-reconstruction. Furthermore, the As and Ga diffraction pattern show a strong influence of this reconstruction as displayed in Fig.2a and 2b. From the diffraction patterns, we verify the known structure of this reconstruction as reported by Biegelsen and Xue, where two Ga-dimers are located on top of the surface and one Ga-dimer in the third layer [1, 2].
The high resolution spectra of As 3d and Ga 3d, which were recorded directly after iron deposition indicate an interdiffusion [3]. Nevertheless, a crystalline bcc structure of the Fe grown on the GaAs (4×2) surface is indicated by the photoelectron diffraction pattern of the Fe 3p signal, as shown in Fig.2c.
Further, a strong Mg^{2+} state is displayed in the high-resolution spectra of the Mg 2p signal. The Fe 3p signal exhibits an oxidation state. From the diffraction pattern we propose two layers of iron-oxide at the interface. These oxide-layers are generated as a consequence of MgO deposition onto the clean Fe-film. The results are in excellent agreement with the results of Meyerheim *et al.* [4].
In this study, we report the crystalline properties of the GaAs, the Fe and MgO films at the interface for the first time, as shown in Fig. 2.

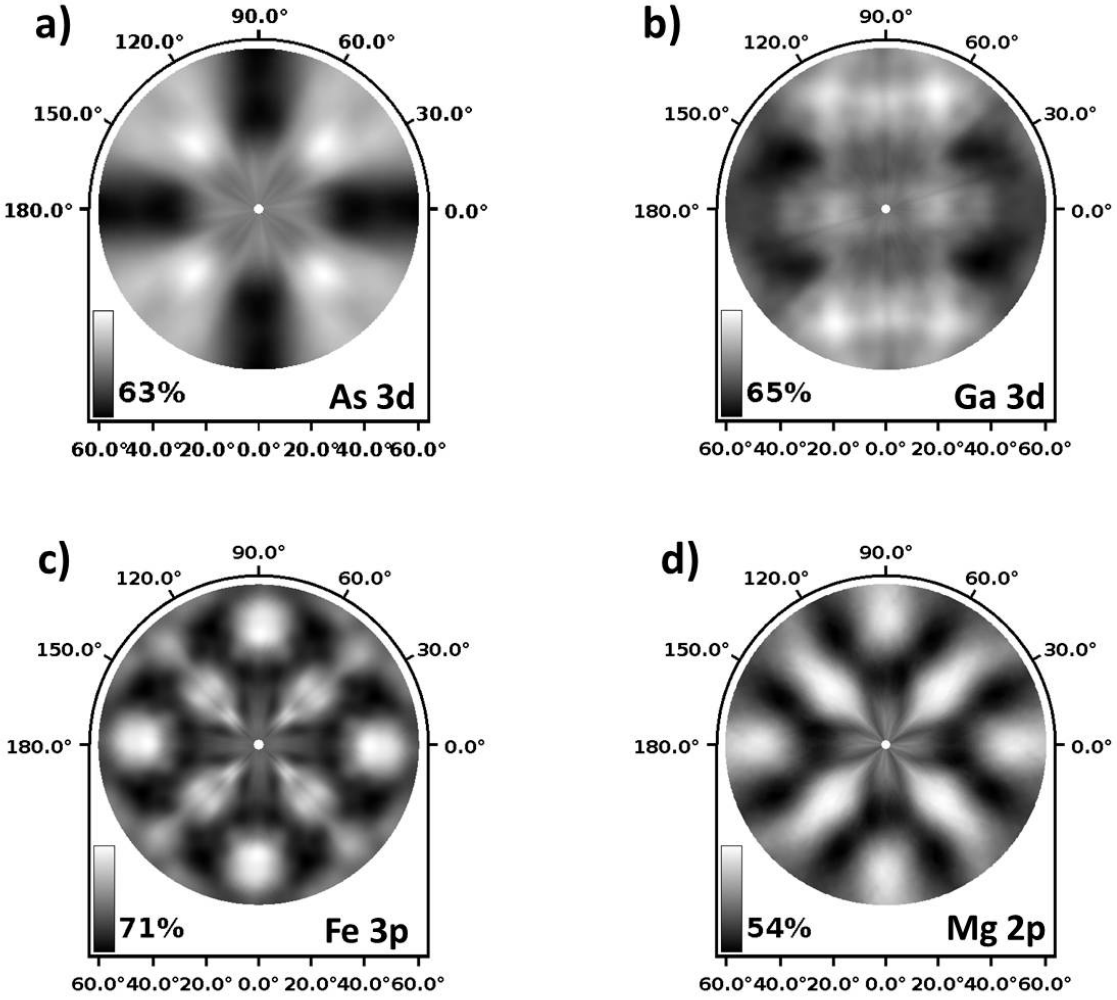

Figure 2: The diffraction patterns of the three layer system MgO/Fe/GaAs(001). The signals of As 3d, Ga 3d, Fe 3p and Mg 2p reveal a different diffraction signature, indicating the crystalline local environment of each emitter and a different local structure.

References

[1] Qi-Kun Xue, T. Hashizume, and T. Sakurai. Scanning tunneling microscopy of III-V compound semiconductor (001) surfaces. *Progress in Surface Science*, **56**(1-2):1 – 131, 1997.

[2] D. K. Biegelsen, R. D. Bringans, J. E. Northrup, and L.-E. Swartz. Surface reconstructions of GaAs(100) observed by scanning tunneling microscopy. *Phys. Rev. B*, **41**:5701–5706, 1990.

[3] R. Moosbühler, F. Bensch, M. Dumm, and G. Bayreuther. Epitaxial Fe films on GaAs(001): Does the substrate surface reconstruction affect the unaxial magnetic anisotropy. *Journal of Applied Physics*, **91**(8757), 2002.

[4] H. L. Meyerheim, R. Popescu, N. Jedrecy, M. Vedpathak, M. Sauvage-Simkin, R. Pinchaux, B. Heinrich, and J. Kirschner. Surface X-ray diffraction analysis of the MgO/Fe(001) interface: Evidence for an FeO layer. *Phys. Rev. B*, **65**(144433), 2002.

Magneto-Optical Polarization Spectroscopy at the Co 3p edge

M. F. Tesch, M. C. Gilbert, H.-Ch. Mertins, D.E. Bürgler[1], C. M. Schneider[1,2]

Münster University of Applied Sciences, Stegerwaldstr. 39, D-48565 Steinfurt
1) Forschungszentrum Jülich GmbH, Peter Grünberg Institut (PGI-6), D-52425 Jülich
2) Fakultät f. Physik & Center for Nanointegration Duisburg-Essen (CeNIDE), Uni Duisburg-Essen, D-47048 Duisburg

Magneto-optical polarization spectroscopy is a powerful tool to determine the complete set of magneto-optical constants of magnetic materials, thin layers and multilayer systems. We present first results obtained with a newly built UHV-chamber, which is designed for polarization experiments as well as for intensity measurements in longitudinal, transversal and polar magnetization geometry. It thus allows for classical MOKE, XMLD, XMCD and Voigt-spectroscopy in reflection and partially in transmission. This capability is demonstrated at the Co 3p edge. The observed magneto-optical signals at the low energy 3p edges are as large as at the 2p edges, but with strongly enhanced reflectivity which drastically increases the signal to noise ratio.

The experimental setup (Fig. 1) consists of a UHV-chamber with 600 mm diameter. In the center a sample magnetizing device based on rotating permanent magnets /1/ is placed on a θ/2θ-goniometer table. This allows for tuning the angle of incident light from 0° to 88° while the polarization detector, or alternatively a GaAsP-diode for intensity measurements are moved by 2θ into the reflected beam. A set of pin holes and higher order filters refine the incoming light. The chamber can be used at synchrotron beamlines as well as in the laboratory with visible xenon light sources or EUV deuterium sources. Magnetic fields up to 500 mT with a resolution of 0.02 mT are achievable and monitored via UHV compatible Hall sensors. A polarization analysis of the synchrotron radiation is performed via a Rabinovitch detector using a gold mirror near the Brewster angle /2/. The entire UHV chamber is arranged on a base-frame and can easily be aligned to the incoming beam with an accuracy of 0.01° and 0.1 mm. The accuracy of the θ/2θ goniometer table, i.e. the rotation axes θ and 2θ is better than 0.01° and the alignment and accuracy of the Rabinovitch detector is better than 0.02°.

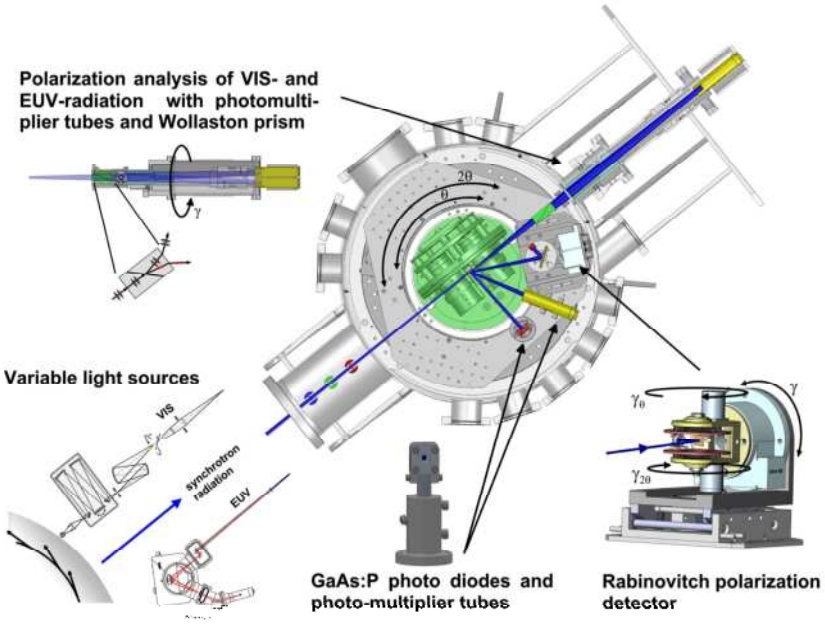

Fig. 1 Experimental setup with optical components and detectors.

The reflection and polarization experiments were performed at the TGM beamline 12 at DELTA. The sample was a 50 nm thin polycristalline Co layer grown on a Si wafer and capped with a 3 nm thin Cu

layer to prevent oxidation. The incoming synchrotron radiation was predominantly linearly p – polarized with electric field vector horizontally oriented. The sample was installed vertically with vertical rotation axis θ leading to a horizontal scattering plane of the reflected light, i.e. p-reflection geometry. Two different magnetization geometries were employed: in T-MOKE the magnetic field was parallel to the sample surface with vertical orientation. In L-MOKE the magnetic field was parallel to the sample surface but oriented horizontally /3/. The T-MOKE asymmetry concerns the change of intensity for linear polarized light with the polarization plane parallel to the plane of incidence. The L-MOKE intensity concerns the change of intensity for circular polarized light with the spin of the photons either parallel or antiparallel to the magnetization direction.

To detect the magnetic information from intensity measurements the absolute reflectance R^+ and R^- is measured for two opposite magnetic field directions $B^{+/-}$. From this the asymmetry parameter $A = (R^+ - R^-)/(R^+ + R^-)$ is deduced. The result is shown in Fig. 2 for T-MOKE. The reflectance (Fig. 2 top) increases to $8 \cdot 10^{-3}$ at the Co 3p edge near 62 eV. This is 100 times larger compared to the 2p edge near 780 eV /3/ and thus allows for spectroscopy even at large angles of incidence which are measured with respect to the sample surface. Maximum T-MOKE asymmetry is observed for angles of incidence close to the Brewster angle near 45°. Peak values of up to 23.1% are obtained which are similar to results at the 2p edge.

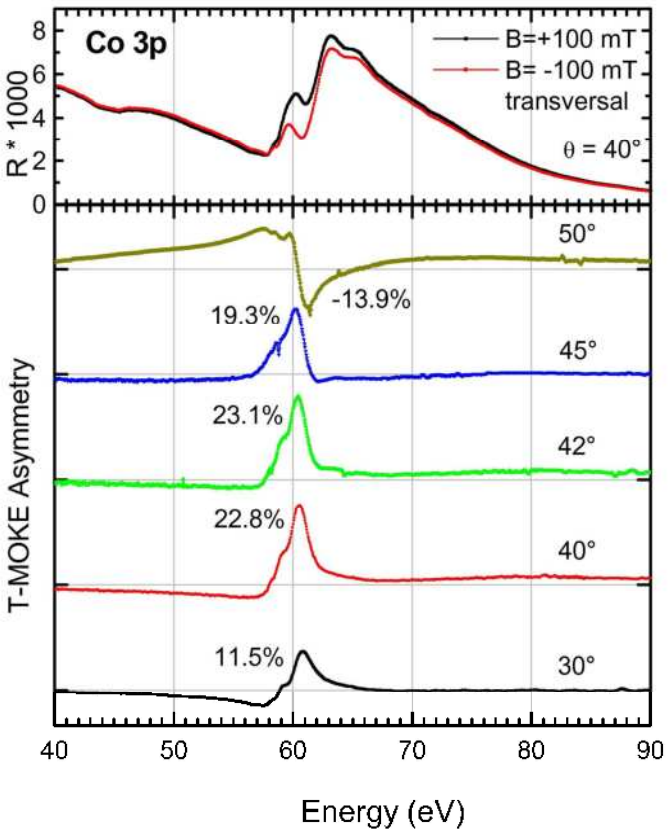

Fig. 2 top: absolute reflectivity for B = +/- 100 mT.
bottom: T-MOKE asymmetry spectra for different angles of incidence, deduced from the reflectance.

For L-MOKE geometry asymmetry spectra could also be deduced. This is astonishing since the L-MOKE asymmetry is observed with circularly polarized light only and should vanish for pure linear polarized light. However, a polarization analysis of the incoming beam at 60 eV revealed, as expected, a strong contribution of linearly p-polarized light $P_{\mathrm{lin}} = 0.9$, but also a small amount of circular polarization $P_{\mathrm{circ}} = 0.43$.

Additionally to these intensity measurements a polarization analysis of the light after reflection from the Co sample was performed. The magnetic field was applied in L-MOKE geometry. The Rabinovitch analyzer was moved into the reflected beam. A polarization analysis was performed by rotating the Au-mirror of the analyzer around the beam axis by the angle γ while the intensity was detected (Fig. 1, bottom, right side). The intensity can be expressed by the formula $I = I_0\left(1 + P_{Pow} \cdot P_{Lin} \cdot \cos(2\gamma - 2\theta)\right)/2$ where I_0 is the intensity of the light after interacting with the

sample, P_{pow} is the polarizing power of the Au mirror, P_{Lin} is the degree of linear polarization of the detected light and θ is the rotation angle of the polarization plane of the light /3/. Fitting the curve with this expression directly yields the Kerr rotation angle θ. With the calculated polarization power of the Au mirror P_{pow} the degree of polarization P_{Lin} of the reflected light was deduced. From this the Kerr ellipticity is deduced via the relation $\varepsilon = 0.5 \cdot \arcsin(\sqrt{1 - P_{Lin}^2})$ (Fig. 3). Each data point of the rotation and the ellipticity is measured by a full analyzer scan. Rotation angles of up to 3° are obtained. While the T-MOKE asymmetry data are comparable to that obtained at the 2p edges the rotation angles at the 3p edge are smaller by a factor five /3/.

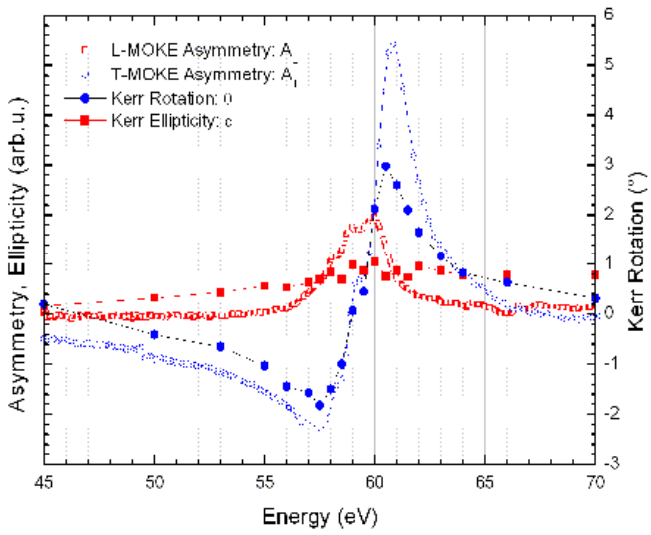

Fig. 3: filled symbols Kerr rotation and Kerr ellipticity, deduced from polarization analysis. Open symbols asymmetry spectra for L- and T-MOKE geometry.

The polarization spectra and the intensity spectra are directly correlated via the magneto optical constants. Measurements at the 2p edges of transition metals show a proportionality between the Kerr rotation and the T-MOKE asymmetry and a proportionality between the Kerr ellipticity and the L-MOKE asymmetry, using circularly polarized light /3/. This proportionality also was found at the Co 3p edges (Fig. 3). While it is well pronounced for the rotation angle and T-MOKE asymmetry it is less pronounced for the ellipticity and the L-MOKE asymmetry which might be due to the increased error bars for the determination of the ellipticity from polarization spectra.

/1/ M. Gilbert, H.-Ch. Mertins, M. Tesch, et al., Rev. Sci. Instrum, accepted 2011

/2/ F. Schäfers, H.-Ch. Mertins, A. Gaupp, et al., Appl. Opt. **38**, 4074 (1999)

/3/ H.- Ch. Mertins, S. Valencia, et al., Appl. Phys. A **80**, 1011 (2005)

Thermal stability of ultra thin HfO_2 films and structure determination of $HfSi_2$ islands on Si(110)

F. Schönbohm[1,2,*], C. D. Weier[1], T. Lühr[1], K. Skaja[1], S. Döring[2], U. Berges[2], and C. Westphal[1,2]

[1] Experimentelle Physik 1 - Universität Dortmund, Otto-Hahn-Str. 4, D 44221 Dortmund, Germany
[2] DELTA - Universität Dortmund, Maria-Goeppert-Mayer-Str. 2, D 44227 Dortmund, Germany
[*] corresponding author: frank.schoenbohm@tu-dortmund.de

(October 2011)

The ongoing miniaturization of electronic devices from one generation to the next reaches a physical limit when the SiO_2 gate dielectric is reduced below 2 nm. Due to increasing tunnel currents through the thin gate dielectrics the electronic devices loose their efficiencyfor structures below approximately 12 Å thickness. However, thin gate dielectrics are required in order to achieve high gate capacities. In order to minimize the undesired leaking currents alternative materials replacing SiO_2 are in the focus of current research. Presently, promissing candidates replacing the SiO2 dielectricum are the oxides of zirconium and hafnium. These materials are often referred to as $high-k$ materials due to their higher dielectric constant. The fabrication process of SiO_2 based MOSFET semiconductors requires temperatures of approximately 1050°C for dopant activation while thin HfO_2 films on clean silicon surfaces are already destroyed at much lower temperatures. Thus, the thermal stability of the HfO_2 films on Si(110) is investigated within a temperature range from 500°C up to 770°C.

Fig. 1 displays the photoelectron intensity of the Hf 4f, Si 2p, and O1 s as a function of temperature. The Hf 4f and Si 2p spectra were recorded at a photon energy of $h\nu = 320$ eV while the O 1s intensity was recorded at a photon energy of $h\nu = 650$ eV. For an annealing temperature of up to 730°C there is hardly no change within the Si 2p, Hf 4f and O 1s spectra. However, after annealing at 770°C the O 1s intensity is drastically reduced as shown by the dotted spectra in Fig. 1 c). Also, the Si 2p intensity shows a similar dependence of the annealing temperature as displayed in Fig. 1 b). Again, the most significant change in the spectra occurs at a temperature of 770°C. For spectra recorded after annealing at 770 °C the Si-oxide signal displayed at the low kinetic energy side of the spectrum vanishes indicating oxygen completely removed from the surface. Only the signal of the Si bulk component remains with a strongly increased intensity at the surface and its intensity is increased. The spectrum presented in Fig. 1 a) is composed by photoemission signals from the O 2s and Hf 4f intensities which are separated by $\Delta E_{kin} = 6.1$ eV. The experimental spectral resolution is not sufficient for a further peak separation. For temperatures up to 730°C both intensities remain nearly constant. After annealing at 770°C the O 2s intensity is strongly diminished since oxygen is nearly completely removed from the surface. As a consequence, the Hf 4f intensity formerly deriving from the hafnium-oxide is chemically shifted to higher kinetic energies now. The chemical shift is caused due to the formation of $HfSi_2$ on the surface because Hf was bound to the oxygen within Hf-oxide is now bound to the Si substrate. Further, the $HfSi_2$ component shows an asymmetric line shape compared to the line shape of HfO_2. The change is caused due to the transformation from the insulating HfO_2 to $HfSi_2$ with metal-like properties. The observed intensity increase of the Si 2p intensity might be induced by the formation of $HfSi_2$

islands which reveal some of the former buried Si substrate in the space between the islands.

In order to investigate the atomic structure of the $HfSi_2$ at the surface an XPD pattern was recorded after annealing at 770°C. The pattern presented in Fig. 1 d is recorded at a photon energy of $h\nu = 180\,\mathrm{eV}$ corresponding to a kinetic energy of $E_{kin} = 161.5\,\mathrm{eV}$. Presently, a structure determination comparing the experimental diffraction pattern with simulated diffraction patterns obtained for model structures is still in progress.

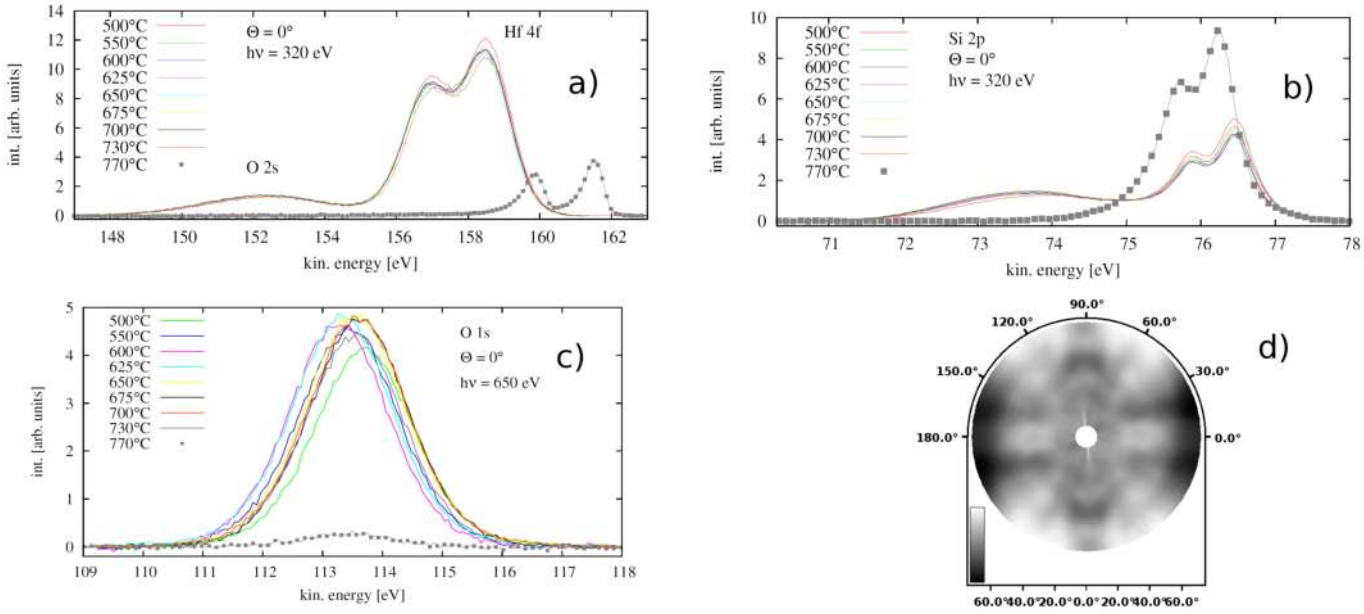

Abbildung 1: Photoelectron intensities of Hf 4f, Si 2p, and O 1s as a function of annealing temperature. For temperatures up to 730°C all spectra remain constant. The dotted spectra in a), b), and c) were recorded after annealing at 770°C. At this temperature the oxygen is removed from the sample c). Thus, oxide components within the Hf 4f a) and Si 2p b) intensities are also removed from the spectra. XPD pattern of the Hf 4f intensity was recorded after annealing at 770°C d).

Acknowledgments:
This work was financially supported by the Forschungsschule NRW. Thanks go to the staff of DELTA for continuous support during the beamtimes.